

Space - scale resolved surface-atmospheric fluxes across a heterogeneous, mid-latitude forested landscape

Sreenath Paleri^{1,1}, Ankur Rashmikanth Desai^{1,1}, Stefan Metzger^{2,2}, David Durden^{3,3}, Brian Butterworth^{4,4}, Matthias R. Mauder^{5,5}, Katrin Kohnert^{6,6}, and Andrei Serafimovich^{7,7}

¹University of Wisconsin-Madison

²NEON Program, Battelle

³Battelle Ecology Inc.

⁴University of Colorado Boulder

⁵KIT

⁶German Council of Experts on Climate Change, Berlin, Germany

⁷GFZ German Research Centre for Geosciences, Telegrafenberg, Potsdam, Germany

November 30, 2022

Abstract

The Earth's surface is heterogeneous at multiple scales owing to spatial variability in various properties. The atmospheric responses to these heterogeneities through fluxes of energy, water, carbon and other scalars are scale-dependent and non-linear. Although these exchanges can be measured using the eddy covariance technique, widely used tower-based measurement approaches suffer from spectral losses in lower frequencies when using typical averaging times. However, spatially resolved measurements such as airborne eddy covariance measurements can detect such larger scale (meso- β , γ) transport. To evaluate the prevalence and magnitude of these flux contributions we applied wavelet analysis to airborne flux measurements over a heterogeneous mid-latitude forested landscape, interspersed with open water bodies and wetlands. The measurements were made during the Chequamegon Heterogeneous Ecosystem Energy-balance Study Enabled by a High-density Extensive Array of Detectors (CHEESEHEAD19) intensive field campaign. We ask, how do spatial scales of surface-atmosphere fluxes vary over heterogeneous surfaces across the day and across seasons? Measured fluxes were separated into smaller-scale turbulent and larger-scale mesoscale contributions. We found significant mesoscale contributions to H and LE fluxes through summer to autumn which wouldn't be resolved in single point tower measurements through traditional time-domain half-hourly Reynolds decomposition. We report scale-resolved flux transitions associated with seasonal and diurnal changes of the heterogeneous study domain. This study adds to our understanding of surface atmospheric interactions over unstructured heterogeneities and can help inform multi-scale model-data integration of weather and climate models at a sub-grid scale.

Space-scale resolved surface fluxes across a heterogeneous, mid-latitude forested landscape

Sreenath Paleri ¹, Ankur R. Desai ¹, Stefan Metzger ^{2,1}, David Durden ²,
Brian J. Butterworth ^{3,4}, Matthias Mauder ^{5,6}, Katrin Kohnert ^{7*}, Andrei
Serafimovich ^{7†}

¹Department of Atmospheric and Oceanic Sciences, University of Wisconsin-Madison, Madison,
Wisconsin, USA

²Battelle, National Ecological Observatory Network, 1685 38th Street, Boulder, Colorado, USA

³Cooperative Institute for Research in Environmental Sciences, University of Colorado, Boulder, Colorado,
USA

⁴NOAA Physical Sciences Laboratory, Boulder, Colorado, USA

⁵Institute of Hydrology and Meteorology, Technische Universität Dresden, Dresden, Germany

⁶Institute of Meteorology and Climate Research – Atmospheric Environmental Research, Karlsruhe

Institute of Technology, Garmisch-Partenkirchen, Germany

⁷ GFZ German Research Centre for Geosciences, Telegrafenberg, Potsdam, Germany

Key Points:

- Substantial mesoscale surface atmospheric fluxes were measured across a heterogeneous mid-latitude forested domain from a wavelet based analysis of airborne flux measurements.
- Measured fluxes show distinct seasonal and diurnal variations.
- Measured mesoscale fractions of sensible and latent heat fluxes do not behave similarly.

*Now at: German Council of Experts on Climate Change, Berlin, Germany

†Now at: Deutscher Wetterdienst, Offenbach, Germany

Corresponding author: Sreenath Paleri, paleri@wisc.edu

23 **Abstract**

24 The Earth’s surface is heterogeneous at multiple scales owing to spatial variability in
 25 various properties. The atmospheric responses to these heterogeneities through fluxes of
 26 energy, water, carbon and other scalars are scale-dependent and non-linear. Although these
 27 exchanges can be measured using the eddy covariance technique, widely used tower-based
 28 measurement approaches suffer from spectral losses in lower frequencies when using typical
 29 averaging times. However, spatially resolved measurements such as airborne eddy covari-
 30 ance measurements can detect such larger scale (meso- β , meso- γ) transport. To evaluate
 31 the prevalence and magnitude of these flux contributions we applied wavelet analysis to
 32 airborne flux measurements over a heterogeneous mid-latitude forested landscape, inter-
 33 spersed with open water bodies and wetlands. The measurements were made during the
 34 Chequamegon Heterogeneous Ecosystem Energy-balance Study Enabled by a High-density
 35 Extensive Array of Detectors (CHEESEHEAD19) intensive field campaign. We ask, how do
 36 spatial scales of surface-atmosphere fluxes vary over heterogeneous surfaces across the day
 37 and across seasons? Measured fluxes were separated into smaller-scale turbulent and larger-
 38 scale mesoscale contributions. We found significant mesoscale contributions to sensible and
 39 latent heat fluxes through summer to autumn which wouldn’t be resolved in single point
 40 tower measurements through traditional time-domain half-hourly Reynolds decomposition.
 41 We report scale-resolved flux transitions associated with seasonal and diurnal changes of the
 42 heterogeneous study domain. This study adds to our understanding of surface-atmospheric
 43 interactions over unstructured heterogeneities and can help inform multi-scale model-data
 44 integration of weather and climate models at a sub-grid scale.

45 **Plain Language Summary**

46 Accurate and reliable knowledge of the surface-atmospheric transport of mass and en-
 47 ergy is essential to inform our theories and models of Earth system processes. Convention-
 48 ally, such transport has been measured by tower-mounted weather instruments that make
 49 high frequency measurements. However, experimental and simulation studies over the last
 50 couple of decades have shown that there is an imbalance between incoming, available energy
 51 and outgoing transport as observed from tower-mounted setups. A dominant hypothesis ad-
 52 dressing this imbalance issue postulates that there exists significant larger landscape scale
 53 transport (of the order of 10-100 km) over the course of a day. Single point tower mea-
 54 surements would not be able to include such transports in their conventional process flows.
 55 We use airborne data collected over a mid-latitude temperate forest in Northern-Wisconsin,
 56 USA to quantify large scale transport over the forested domain. Observations were made
 57 over the course of single days in July, August and September to include seasonal landscape
 58 transitions. The measured surface-atmospheric exchange is resolved into smaller and larger
 59 scale contributions using a space-frequency analysis framework that has been in use for
 60 aircraft measured atmospheric data. We report substantial large scale contributions with
 61 daily, seasonal and spatial characteristics.

62 **1 Introduction**

63 Surface-atmospheric fluxes of energy, momentum, water, carbon and other scalars are
 64 integral components of Earth system processes. Terrestrial ecosystems act as important
 65 intermediaries for these exchange processes, influencing Earth’s weather and climate sys-
 66 tems (Pielke et al., 1998). However, the land-surface is heterogeneous at multiple scales
 67 owing to spatial variability in multiple properties and the atmospheric responses to these
 68 heterogeneous surface forcings through the fluxes of energy, water, carbon and other scalars
 69 are also scale dependent and non-linear (Avissar & Schmidt, 1998). Since the scales of
 70 transport vary from Kolmogorov microscale in the turbulent regime to the mesoscale it is not
 71 easy to resolve the contributions from all of the relevant scales directly using observations
 72 or simulations (Bou-Zeid et al., 2020)

73 The primary transport process in the atmospheric boundary layer (ABL) is turbulence
74 and the surface-atmospheric turbulent fluxes can be directly measured using the eddy-
75 covariance (EC) technique (Aubinet et al., 2012; Foken, 2017). The EC technique uses
76 Reynolds decomposition of the Navier-Stokes equation for momentum and scalar transport,
77 with the assumptions of stationarity and horizontal homogeneity, to calculate turbulent
78 fluxes in the ABL. Tower based EC measurements are widely used to study ecosystem level
79 biosphere-atmosphere interactions and quantify surface-atmospheric fluxes (Aubinet et al.,
80 1999; Baldocchi et al., 2001). Even with careful experimental design and quality control,
81 they are however limited by their surface flux footprints (i.e., part of the upstream surface
82 contributing to the measured flux). Moreover, requirements for stationarity can complicate
83 sampling flux contributions from lower frequencies as well (Desjardins et al., 1997; Mahrt,
84 2010)

85 So, a good first order sanity check on tower measured turbulent fluxes would be to
86 check for the closure of the measured surface energy budget, evaluating whether available
87 energy (the difference between measured net radiation and ground heat flux) within the
88 control volume sampled by the tower is balanced by the measured sum of turbulent sensible
89 and latent heat fluxes (Oncley et al., 2007; Foken, 2008; Foken et al., 2010; Mauder et
90 al., 2020). Such a check would also be important to validate land-surface and biological
91 model parameters such as surface flux parameterisations in weather and climate models,
92 water vapor surface conductances in ecosystem and land-surface models or validating model
93 predictions of net ecosystem exchanges (NEE). However, a persistent surface energy balance
94 residual has been reported in prior investigations across multiple sites in multiple ecosystems
95 (Oncley et al., 2007; Foken et al., 2010; Mauder et al., 2020)

96 Simulations and observational studies have shown that there can be larger scale trans-
97 port linked to landscape variability. Based on their analysis of tower measured EC data
98 Bernhofer (1992) had attributed the residuals to large scale non-turbulent transport driven
99 by surface gradients. Finnigan et al. (2003) pointed out that the conventionally-used averag-
100 ing windows of 30 minutes could act as a high pass filter for the data. They also noted that
101 pre-treating tower measured turbulent data by rotating the measurement coordinates so
102 that x-axis of measurement is aligned with the mean horizontal wind could also contribute
103 to the same. Such data processing would remove contributions of motions with periods
104 longer than the averaging times to the covariance being measured. Early Large Eddy Sim-
105 ulation (LES) studies (Kanda et al., 2004; Inagaki et al., 2006; Steinfeld et al., 2007) with
106 idealized surface forcings indicated that transport due to turbulent organized structures
107 and thermally-induced mesoscale structures can cause systematic underestimation of fixed
108 point tower flux measurements. Maronga and Raasch (2013) conducted a LES study us-
109 ing measured sensible and latent heat fluxes as imposed surface boundary conditions over
110 the LITFASS-2003 field experiment domain and diagnosed signals of heterogeneity-induced
111 vertical velocities linked to landscape heterogeneities. Using a wavelet analysis of airborne
112 turbulent data during the BOREAS field experiment, Mauder, Desjardins, and MacPherson
113 (2008) quantified the mesoscale transport across a temperate heterogeneous landscape to
114 be 10% of surface measured available energy and of the same order of magnitude as tower
115 measured residuals over the domain. The LES study by K. Xu et al. (2020) employed sim-
116 ulated towers over idealized heterogeneities. Following a spatio-temporal eddy covariance
117 approach for simulated towers they could account for 95% of the available energy with one
118 tower per 40 km². Such a spatial approach seems to account for the landscape-scale low
119 frequency transport. The recent LES study by Margairaz et al. (2020) over idealized het-
120 erogeneities also shows that fluxes by secondary circulations can account for 5-10% of near
121 surface sensible heat fluxes.

122 These investigations indicate that when surface heterogeneity starts influencing the
123 surface-atmospheric transport, there can be quasi-stationary circulations modulated by the
124 heterogeneity amplitudes and background wind. Such structures could lead to increased
125 advective transport and flux divergences, thereby altering the net transport associated with

126 the turbulent covariance term, measured through the eddy covariance method (Mahrt, 2010;
 127 Mauder et al., 2020). Quantifying and diagnosing such a 3 dimensional transport and hori-
 128 zontal variability of surface atmospheric fluxes over heterogeneous domains in the field calls
 129 for the deployment of intensive instrumentation that can sample the surface atmospheric
 130 exchanges at multiple, overlapping scales (Wulfmeyer et al., 2018). Identification and mea-
 131 surement of such structures and their contributions from field observations call for spatially
 132 resolving measurement techniques, such as a distributed tower network (Oncley et al., 2007;
 133 Mauder, Desjardins, Pettey, et al., 2008; Engelmann & Bernhofer, 2016; Morrison et al.,
 134 2021), airborne measurements (Mahrt, 1998; Strunin & Hiyama, 2004; Bange et al., 2002,
 135 2006; Mauder, Oncley, et al., 2007), scintillometers (Foken et al., 2010; F. Xu et al., 2017;
 136 Meijninger et al., 2006) and LiDAR measurements (Drobniski et al., 1998; Higgins et al.,
 137 2013; Eder et al., 2015) etc. Spectral analysis of tower measured turbulence data can also
 138 give some insight into the nature of flux contributions from the lower frequencies (Y. Zhang
 139 et al., 2010; G. Zhang et al., 2014; Zhou et al., 2019; Gao et al., 2020).

140 Among these measurements, airborne EC measurements are one of the few that can
 141 directly measure the spatial distribution of 3D turbulence across a study domain (Mahrt,
 142 1998, 2010). Moreover, with spatial transects, airborne measurements can directly sam-
 143 ple contributions from larger (of the order of meso- β 20-200 km, meso- γ 2-20 km, from
 144 Orlanski (1975)) scale persistent structures excited by surface heterogeneities. In contrast,
 145 for ground-based measurements these larger scale structures would have to drift by their
 146 field-of-view. Airborne transects through a study domain can also pass through multiple
 147 quasi-stationary eddies, giving robust statistics for the measured fluxes.

148 Here, we use airborne turbulence data collected over a heterogeneous mid-latitude
 149 forested landscape interspersed with creeks and lakes in the Chequamegon-Nicolet National
 150 forest near Park Falls, Wisconsin USA. Through this analysis we aim to address the following
 151 research questions:

- 152 1. Can spatially-resolved airborne eddy covariance identify spatial scales of surface-
 153 atmosphere fluxes over heterogeneous surfaces?
- 154 2. How do spatial scales of surface-atmospheric fluxes vary across the day and across
 155 seasons? What is the role of ABL stability and land-surface variability in modulating
 156 these exchanges?
- 157 3. What are the ensuing implications for improving the surface energy balance closure
 158 or understanding scales of turbulent transport?

159 The airborne measurements were collected as part of the Chequamegon Heterogeneous
 160 Ecosystem Energy-balance Study Enabled by a High-density Extensive Array of Detectors
 161 (CHEESEHEAD19) field experiment (Butterworth et al., 2021), conducted from July to
 162 October 2019. The experimental study design aimed to sample the landscape transition
 163 from late summer to early fall and the associated ABL responses. The CHEESEHEAD19
 164 airborne dataset presents a unique opportunity to analyse long periods of airborne EC
 165 over long legs (30 km) in a heterogeneous region over multiple times a year with differing
 166 patterns of surface sensible and latent heat fluxes. The dataset provides an extensive set
 167 of scenarios to investigate our research questions and derive principles from. To quantify
 168 and spatially localise contributions from all the relevant scales of transport we calculate
 169 the surface atmospheric fluxes through the wavelet cross-scalograms of the turbulent data
 170 (Strunin & Hiyama, 2004, 2005; Mauder, Desjardins, & MacPherson, 2007; Metzger et al.,
 171 2013). A wavelet based analysis can distinguish surface-atmosphere fluxes at multiple scales
 172 and quantify the contributions from larger scales, allowing us to resolve scale transport
 173 across space.

174 To those ends, we pose the following null and alternative hypotheses:

- 175 • H0: Mesoscale transport is an invariant, small fixed fraction of the total flux.

- HA: Persistent contributions of larger scale (in the range of meso- β to meso- γ) fluxes to the daytime sensible and latent heat fluxes exist with diurnal and seasonal variations.

2 Data and Methods

2.1 Experiment description

The Chequamegon Heterogeneous Ecosystem Energy-balance Study Enabled by a High-density Extensive Array of Detectors (CHEESEHEAD19) was a field campaign conducted from June to October 2019, in Chequamegon-Nicolet National Forest, Wisconsin, USA. The experiment was designed to intensively sample and scale land-surface properties and the ABL responses to it across a heterogeneous mid-latitude forested landscape interspersed with creeks and lakes. The two main motivations for the field experiments were to determine how spatial heterogeneity of the surface impacts the local energy balance and atmospheric circulations and to evaluate how the presence or absence of these circulations influence the representativeness of single-point surface fluxes compared to the grid average.

Measurements were made using a suite of observing platforms over a core 10×10 km domain (that would fit within a ‘grid cell’ of a weather/climate model) and a 30×30 km extended domain centred on the Department Of Energy Ameriflux regional tall tower (US PFA 45.9459° N, -90.2723° W). EC fluxes have been measured nearly continuously at the US PFA tall tower since 1996 (Berger et al., 2001) and the study domain is well documented in previous studies that used flux data from the tall tower (Davis et al., 2003; Desai, 2014; Desai et al., 2015). The field campaign collected measurements of ground based and airborne fluxes, atmospheric profiles and surface environment at varying scales. Butterworth et al. (2021) gives a detailed overview of the field experiment design and all of the deployed instrumentation.

Figure 1 shows the land cover classes across the extended domain from the State of Wisconsin Department of Natural Resources Landcover Data (Wiscland 2.0) accessed from <https://dnr.wisconsin.gov/maps/WISCLAND>. The vegetation and land cover within the study domain is characteristic of a mid-latitude temperate forest, dominated by conifers, broadleaf deciduous trees and wetlands. The study domain is also interspersed with open water bodies, the largest being the Flambeau Lake to the North-Eastern sector of the domain. The presence of such a vertically and horizontally heterogeneous surface, with maximum canopy heights ranging from a couple of metres to 35 metres, gives a unique opportunity to study surface atmospheric exchanges over unstructured land-surface heterogeneity where multiple surface properties and roughness elements vary at multiple scales, addressing a crucial gap in our current understanding (Bou-Zeid et al., 2020). Site descriptions of 17 flux tower sites, set up as part of the National Center for Atmospheric Research (NCAR)-Integrated Surface Flux Station (ISFS) network, within the core 10×10 km domain can be found at <http://cheesehead19.org>. This gives an idea about the variation in surface and vegetation properties across the domain. The extended 3-month duration of the field experiment also allows us to sample the shift in the surface energy budget partitioning as the study domain shifts from a latent heat-dominated late summer landscape to a more sensible heat flux-dominated early autumn landscape.

2.2 Airborne intensive observations

Airborne turbulence data were collected over the extended domain with the University of Wyoming King Air (UWKA) research aircraft. The UWKA is a Beechcraft King Air 200T model, a part of the National Science Foundation’s Lower Atmosphere Observation Facility that has been in use for insitu airborne measurements of cloud and boundary layer properties since 1977 (A. Rodi, 2011; Wang et al., 2012). Three seven-day Intensive Observation Periods (referred to as IOPs henceforth) were conducted during the experiment during each

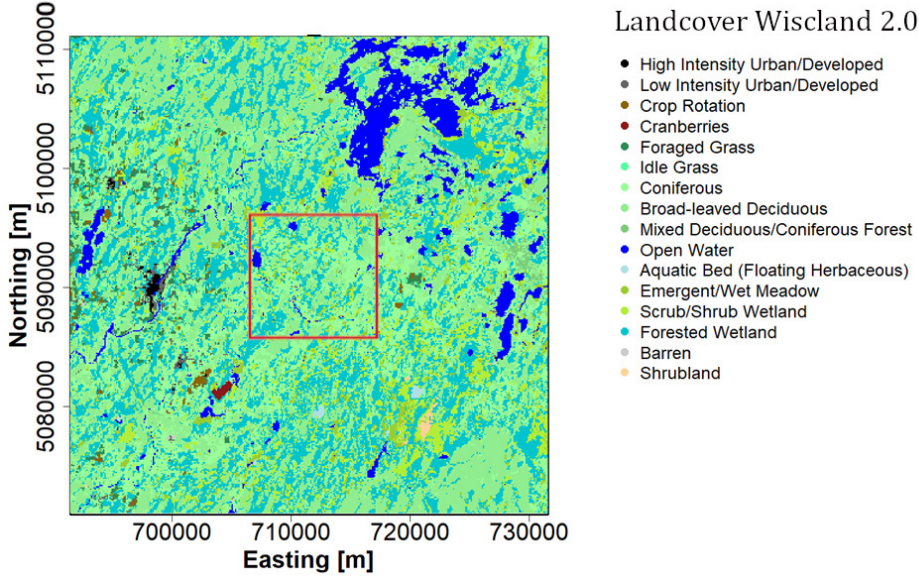


Figure 1: Land Cover classes for a 40×40 km area bounding the study domain from the Wisland 2.0 landcover classification dataset. The 10×10 km core CHEESEHEAD19 domain is shown in the red box.

225 month from July to September when all the available field instrumentation were deployed
 226 simultaneously. During these IOPs the UWKA Research Aircraft flew linear transects across
 227 the domain on four days sampling turbulent measurements of wind velocities, temperature,
 228 water vapor, and CO₂, at a frequency of 25 Hz (Table 1). The airborne experiment was
 229 designed with the help of numerical experiments to maximise spatial coverage over the
 230 domain, ensure adequate sampling of larger scale eddies and ensure crew safety. Metzger et
 231 al. (2021) provides details about the numerical simulations, analysis framework and design
 232 strategy used to come up with the final flight patterns for the airborne measurements.
 233 Figure 2 shows these different patterns and their respective waypoints. Each research flight
 234 pattern was composed of flight transects connecting consecutive waypoints. We refer to
 235 these individual transects as flight legs. The flight legs were designed to be 30 km so that
 236 they extend about 10 km outside of the core 10×10 km domain to ensure that enough
 237 mesoscale contributions to the core 10×10 km domain could be sampled.

238 On each day there was a morning (14:00 - 17:00 Universal Time Coordinated) flight
 239 and an afternoon (19:00 - 22:00 Universal Time Coordinated) research flight. Each Research
 240 Flight (RF) performed 30 km down-and-back transects at 100 m and 400 m above ground
 241 between two consecutive waypoints, alternating between straight and diagonal passes. The
 242 first leg of all transects was at 400 m and the return legs at 100 m. For example, from Table
 243 1, on 2019 July 11th, the morning research flight was RF03 with the WE1 (west-east 1)
 244 flight pattern. For RF03, from Figure 2, the first leg was from waypoint 1 to waypoint 2 at
 245 400 m and the second leg was back to 1 from 2 at 100 m. Then the third leg would be from
 246 1 to 4, diagonally at 400 m and so on.

247 The primary scientific purpose of the higher 400 m legs was to observe the temperature
 248 and moisture profiles using a downward pointing Compact Raman Lidar. The low-altitude
 249 legs were flown at 100 m since this was the lowest altitude deemed safe to fly for the
 250 maximum forest canopy height of 35 m. This also ensures that the measurements taken
 251 were in the surface layer and above the roughness sublayer of the forested domain. Wavelet

Table 1: Dates, times, flight patterns of the flights analysed for all 3 IOPs

Date	Domain start time (UTC)	Domain end time (UTC)	Flight Number	Flight Pattern	Wind Dir (deg)	Wind Speed (m/s)	Short Wave Incoming (W/m ²)
2019-07-09	14:00	16:00	RF01	West-East 2	180	6	643
2019-07-09	19:00	21:00	RF02	West-East 2	210	5	701
2019-07-11	14:00	16:00	RF03	West-East 1	345	3	852
2019-07-11	19:00	21:00	RF04	West-East 1	45	5	829
2019-07-12	14:00	16:00	RF05	West-East 2	225	6	686
2019-07-12	18:00	21:00	RF06	West-East 2	225	5	642
2019-07-13	14:00	16:00	RF07	South-East 2	330	3	833
2019-07-13	19:00	21:00	RF08	South-West 1	330	3	869
2019-08-20	14:00	16:00	RF09	South-East 1	215	3	244
2019-08-20	19:30	22:00	RF10	South-East 1	180	1	648
2019-08-21	14:00	16:30	RF11	South-West 1	0	5	663
2019-08-21	19:00	21:30	RF12	South-West 1	315	6	639
2019-08-23	14:00	16:30	RF15	West-East 2	80	0.5	681
2019-08-23	19:30	21:30	RF16	West-East 2	120	3	703
2019-09-24	14:00	16:30	RF17	South-East 1	230	4	503
2019-09-24	19:00	21:30	RF18	South-East 1	180	5	342
2019-09-25	14:40	17:00	RF19	South-West 1	270	5	573
2019-09-25	19:30	22:00	RF20	South-West 1	310	5	326
2019-09-26	14:00	16:30	RF21	South-East 1	270	3	518
2019-09-26	18:45	21:15	RF22	South-East 1	265	5	422
2019-09-28	14:30	17:00	RF23	West-East 1	353	3	674
2019-09-28	19:00	21:30	RF24	West-East 1	15	3	500

252 cross scalograms of the atmospheric turbulence data from the 100 m legs were used to
 253 calculate the surface atmospheric fluxes during the IOPs.

254 2.3 Wavelet Analysis

255 Wavelet transforms can reveal information localised in both space and frequency do-
 256 mains (Farge 1992, Mahrt et al. 1994) for a given input signal. This distinct property
 257 makes wavelet based time-frequency analysis suited for the analysis of in-homogeneous or
 258 non-stationary geophysics data, unlike other conventional methods such as a Fourier trans-
 259 form or its windowed version (Kumar and Foufoula-Georgiou 1994) that require periodicity.
 260 Airborne measurements over the CHEESEHEAD19 study domain sampled a spatially and
 261 temporally varying surface flux field, including measurements over varying surface roughness
 262 heights, canopy heights and soil properties. In this regard, a wavelet decomposition of the
 263 airborne turbulence measurements over the heterogeneous domain can extract scale-resolved
 264 information and quantify contributions from larger scale quasi-stationary modes induced by
 265 landscape scale heterogeneities. A wavelet analysis also yields a space-scale mapping of the
 266 measured fluxes, throughout the day and across seasons.

267 The wavelet functions and analysis methods were developed for time-frequency anal-
 268 ysis (Farge, 1992; Thomas & Foken, 2005), but since we are working with spatial data,
 269 we've expanded upon the existing methodology to facilitate space-scale analysis. In wavelet
 270 analysis, one starts with choosing a wavelet function or mother wavelet, Ψ , which is lo-
 271 calised in both space and frequency domains and has zero mean (Torrence & Compo, 1998;
 272 Farge, 1992). The mother wavelet of choice for this study is the complex Morlet wavelet,
 273 $\Psi(\eta) = \pi^{-1/4} e^{i\omega_0\eta} e^{-\eta^2/2}$, with the frequency parameter $\omega_0 = 6$ as suggested by Torrence
 274 and Compo (1998). The Morlet wavelet is a complex sine wave modulated by a Gaussian
 275 envelope and has been in use for the analysis of atmospheric turbulence data because the

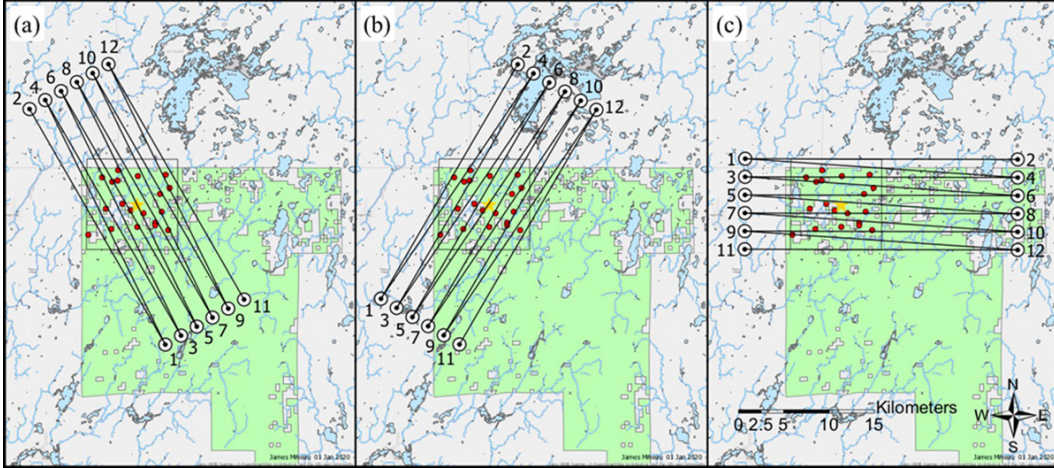


Figure 2: Three sets of waypoints define three distinct flight patterns, named after the starting location and direction of their first waypoint: (a) south-east (SE), (b) south-west (SW), and (c) west-east (WE). Flying the numbered waypoints either in ascending order (SE1, SW1, WE1) or descending order (SE2, SW2, WE2) results in six distinct flight sequences that maximize data coverage under different wind conditions. Map credit: James Mineau, University of Wisconsin – Madison. [Metzger et al. (2021): Figure 14, published by Atmospheric Measurement Techniques, reproduced with permissions under <https://creativecommons.org/licenses/by/4.0/>]

276 resulting wavelet transform offers good localisation in the scale domain (Strunin et al., 2004;
 277 Thomas & Foken, 2005; Mauder, Desjardins, & MacPherson, 2007). The mother wavelet Ψ
 278 can be stretched and squeezed or translated across the spatial domain to construct 'daughter
 279 wavelets' $\Psi_{p,a,b}$ where a is the dilation parameter and b is the translation parameter.

$$\Psi_{p,a,b}(x) = \frac{1}{a^p} \Psi\left(\frac{x-b}{a}\right) = \Psi_p(\eta) \quad (1)$$

280 Here, p is a normalisation parameter and is set as $1/2$ for this study, and η is a non-
 281 dimensional coordinate in the space-scale domain. The wavelet transform is a convolution,
 282 $\int f(x)\Psi_{p,a,b}^* dx$, of a given signal $f(x)$ with the daughter wavelets to yield a series of wavelet
 283 coefficients $T(a,b)$ that are functions of the dilation and translation parameters. $\Psi_{p,a,b}^*$ is
 284 the complex conjugate of $\Psi_{p,a,b}$. Since both the scale and the location of the mother wavelet
 285 filter kernels can be adjusted, such an analysis can yield localised details matched to their
 286 scale (subject to the fundamental Heisenberg uncertainties, Addison (2017)). In the discrete
 287 limit, for a spatial series $f(n)$ with N data points the wavelet coefficients become,

$$T_f(a,b) = \sum_{n=0}^N f(n)\Psi_{p,a,b}^* \quad (2)$$

288 Different localisations or 'daughter wavelets' of the same mother wavelets are scaled and
 289 translated across the input data to extract information about the amplitudes and locations of
 290 matching details corresponding to equivalent amplitudes at corresponding locations present
 291 in the input signal. This allows us to calculate the wavelet spectral energy density (E_f) for
 292 a chosen dilation and locations from the coefficients as $E_f(a,b) = |T_f(a,b)|^2$, referred to as
 293 the wavelet scalogram matrix. Consequently, the variance (σ_f) of the chosen signal, $f(x)$

294 can be calculated by averaging the matrix and summing across the scales,

$$\sigma_f = \frac{\delta j \delta t}{C_\delta N} \sum_{j=0}^J \sum_{n=0}^{N-1} \frac{|T_f(a_j, b_n)|^2}{a_j} \quad (3)$$

295 Here, $\delta t = 0.04$ for the 25 Hz data and δj , the discrete intervals in scale, is set as
 296 0.125, setting up 8 octaves, following Torrence and Compo (1998). C_δ is an admissibility
 297 constant defined for each mother wavelet of choice, to reconstruct the original series from its
 298 wavelet transform. For the complex Morlet wavelet $C_\delta = 0.776$ (Torrence & Compo, 1998).
 299 Similarly, given two signals, $f(n)$ and $g(n)$, a cross-scalogram matrix can be calculated as
 300 $T_f(a, b) \times T_g^*(a, b)$, where $*$ denotes a complex conjugate. Their co-variance can be estimated
 301 by integrating their co-spectral energy spanning the constituent scales across their cross-
 302 scalograms as:

$$cov_{ab} = \frac{\delta j \delta t}{C_\delta N} \sum_{j=0}^J \sum_{n=0}^{N-1} \frac{T_f(a_j, b_n) T_g^*(a_j, b_n)}{a_j} \quad (4)$$

303 A sample wavelet cross-scalogram of vertical wind and water vapour mole fraction
 304 space series is shown in Figure 3 b. Integrating the cross-scalogram in scale and converting
 305 the variance magnitudes to energy units lets us calculate the associated scale-integrated flux
 306 space series, shown in Figure 3 a. The shading in the cross-scalograms denote the amplitude
 307 of the wavelet coefficients. The peaks in the calculated latent heat flux space series can be
 308 seen coinciding with segments of strong amplitudes, which vary throughout the length of
 309 the series reflecting the variability of surface atmospheric transport across the transect.

310 The summation operation in Equation 4 can be performed over any desired subset of
 311 scales to calculate the wavelet covariance between two chosen signals (Torrence & Compo,
 312 1998; Mauder, Desjardins, & MacPherson, 2007). Doing so gives the contribution from
 313 those ranges of scales to the total covariance. This presents the opportunity to quantify
 314 the contributions from different scales over choice of spatial segments by integrating across
 315 subsets of scales without neglecting contributions from scales larger than the choice of spatial
 316 segment. For this study we chose a flux partitioning scale of 2 km to distinguish between
 317 small-scale boundary layer turbulence and larger mesoscale contributions following Mauder,
 318 Desjardins, and MacPherson (2007) and Strunin et al. (2004). The 2 km cutoff serves
 319 as proxy for the maximum boundary layer height, which would be the largest scale for the
 320 turbulent energy producing eddies in the ABL. ABL height shifts are observed in response to
 321 temporal factors such as seasonal and diurnal cycles (Figure 7) as well as spatial variations
 322 in land-cover heterogeneity. However, the 2 km threshold seems to be a good indicator for
 323 the the relative variation in the magnitude of mesoscale fluxes (Section 3.1).

324 2.4 Flux measurement and data processing

325 Wavelet based flux processing of the campaign data was done using the eddy4R family
 326 of open source packages (Metzger et al., 2017). The 25 Hz airborne data product used in this
 327 study was preprocessed by the UWKA research crew to include routine UWKA corrections
 328 and is hosted at the NCAR-Earth Observing Laboratory (EOL) repository as part of the
 329 public CHEESEHEAD19 project data repository (French et al., 2021). Table 2 gives details
 330 of the UWKA instrumentation used for measuring aircraft and atmospheric state variables.
 331 Each research aircraft deployment had a resulting 25 Hz netcdf data file. The data from
 332 these files with all the necessary atmospheric and aircraft state variables were read in to
 333 the eddy4R processing environment. The air temperature, pressure and water vapour mole
 334 fraction data were lag corrected by maximising the cross-correlation with vertical velocity
 335 data (Hartmann et al., 2018). Flight leg start and end times were used to slice the research
 336 flight data into flight leg specific data. This ensured that only data collected during the

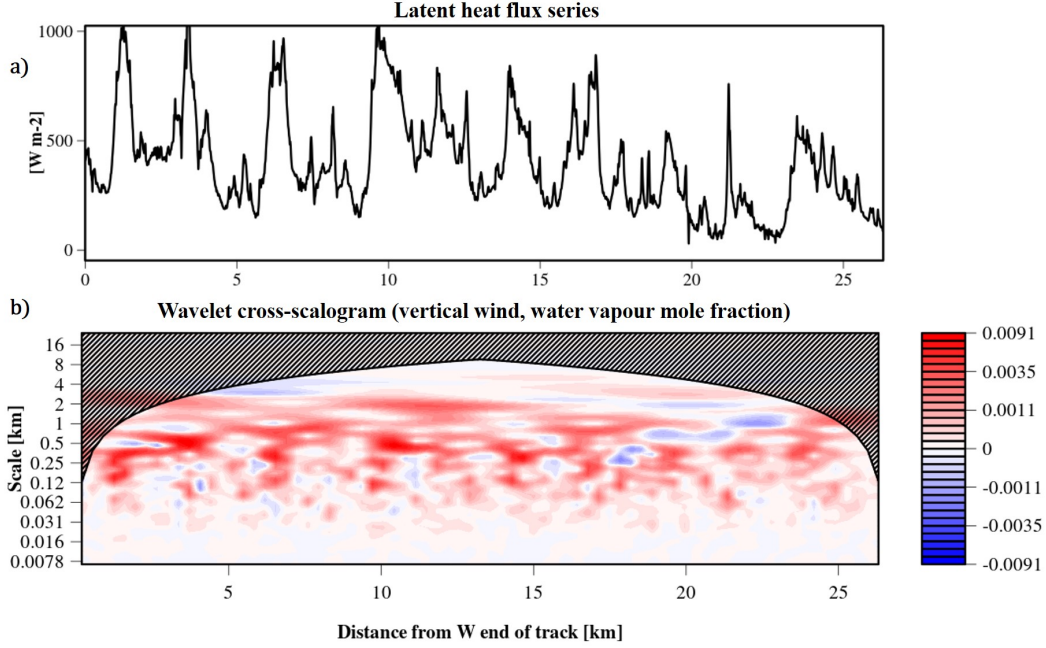


Figure 3: A sample wavelet cross-scalogram (b) between vertical velocity and water vapour mole fraction illustrating the scale-resolved spatial contributions along RF02 flight leg 04. This cross-scalogram is calculated by integrating across spatial scales along the y-axis giving the latent heat flux space series shown in (a). The shading in (b) denotes amplitudes with red shaded regions denoting positive contributions, while blue shades denote negative and white neutral. Hashed portions represent the cone of influence for edge effects.

337 linear transects across the study domain are used for the study and data collected during the
 338 over turnings at the way-point edges are excluded. Convective boundary layer (CBL) height
 339 was measured during the IOP days by two Radiometrics MP-3000A Microwave Radiometers
 340 (MWRs) deployed roughly 45 km west and south to the WLEF tall tower (locations in Figure
 341 1.a Duncan Jr. et al., 2022 and data available from Adler et al., 2021) at the Lakeland and
 342 Prentice airports in Wisconsin. CBL heights from the hourly averaged data product were
 343 also added to the flight leg level data.

344 Flux calculations were performed individually for each flight leg. The missing data
 345 threshold was set to 90%. Each flight leg covered spatial transects of 25 to 30 km, depending
 346 on whether they were horizontal or diagonal along the cardinal wind directions (Section 2.2).
 347 With 25 Hz frequency and an averaged airspeed of 86 m/s, the mean spatial resolution of
 348 the data was 3.5 metres. Hence, the average number of data points for the flight leg level
 349 datasets analysed for each flight was 8200, with datasets ranging from 6500 to 9000 data
 350 points. The minimum daughter wavelet frequency was set at the Nyquist frequency of 12.5
 351 Hz and the maximum depended on the duration of the dataset (averaging to 30 km). The
 352 wavelet frequencies were converted to scale space using the Fourier wavelength for the Morlet
 353 wavelet (Torrence & Compo, 1998). Adaptive, high frequency corrections were applied to the
 354 wavelet scalograms following (Nordbo & Katul, 2013). A spatial series of wavelet covariance
 355 fluxes was calculated from the wavelet cross-scalograms using Equation 4, for overlapping
 356 subintervals of 1000 m (Metzger et al., 2013). The 1000 m subintervals were centred above
 357 each cell of the 100 m resolution Wiscland 2.0 landcover classification dataset for the study
 358 domain (Figure 1, Section 2.5), giving window averaged flux measurements every 100 m.
 359 Random and systematic flux errors were calculated following Lenschow and Stankov (1986)

Table 2: Univerity of Wyoming King Air instrumentation details

Measurement	Instrument	Description
Aircraft State		
3D position, ground velocity, orientation, Body-axis longitudinal/lateral/vertical acceleration	Applanix AV 410 GPS/Inertial Measurement Unit	Applanix Position Orientation System for Airborne Vehicles; combined solid-state/GPS system with real-time differential corrections; higher accuracy post processed data available (Haimov & Rodi, 2013)
Altitude	Stewart Warner APN159 radar altimeter	Altitude above ground level Range:0 - 60000 ft(18288 m); accuracy 1%; resolution: 0.24 ft (0.07 m)
Airspeed	Honeywell Laseref SM Inertial Reference System (IRS)	Range:0-4095 kts; accuracy: 13.5 ft/s ; resolution: 0.0039 kts
flow angles	Rosemount 858AJ five-hole gust probe	Range:+-15; accuracy:0.2; resolution:0.00015
Atmospheric State		
Air temperature	Reverse-flow housing with Minco platinum-resistive element (A. R. Rodi & Spyers-Duran, 1972)	Range: -50 to +50 C; accuracy: 0.5 C ; resolution: 0.006 °C
Wind Components	Applanix AV 410 GPS/Inertial Measurement Unit	Earth relative 3D wind
Atmospheric Pressure	Rosemount 1501 HADS	High Accuracy Digital Sensing module static pressure, corrected for dynamic effects (A. R. Rodi & Leon, 2012) ; Range: 0-1034 mb; accuracy : 0.5 mb, resolution: 0.006 mb
Water vapor	LICOR Li-7500A	LI-COR LI-7500 open-path CO ₂ /H ₂ O Gas Analyzer

360 and Lenschow et al. (1994). The turbulent scale flux space series was calculated by setting
361 the maximum wavelet scale for scalograms at 2 km. The mesoscale flux contributions were
362 then calculated as the difference between fluxes from all scales and the turbulent scale
363 fluxes. While creating summary statistics and figures an absolute threshold of 10 Wm^{-2}
364 was applied for sensible and latent heat fluxes to ensure that the fluxes are well resolved. A
365 hard threshold of $(-400, 1000) \text{ Wm}^{-2}$ was set for the LE space series and $(-50,400) \text{ Wm}^{-2}$
366 for the H series to remove spurious measurements.

367 2.5 Footprint modelling and flux topographies

368 Footprint of a flux measurement refers to the effective finite measurement area upwind
369 of the sensors from where the eddies are being sampled from (Foken et al., 2006). Kljun
370 et al. (2004) is a 1D parameterisation of a backward Lagrangian model (Kljun et al., 2002)
371 in the stable to strongly convective ABL. Since this is not crosswind-integrated, Metzger
372 et al. (2013) combined it with a Gaussian crosswind dispersion function. This is implemented
373 in the analysis currently. The model requirements measurements of friction velocity (u^*),
374 measurement height (z), standard deviation of the vertical wind (σ_w) and the aerodynamic
375 roughness length (z_0). With the exception of z_0 all the other variables are directly measured
376 by the UWKA. z_0 is inferred from a logarithmic wind profile with the integrated universal
377 function for momentum exchange after Businger et al. (1971) in the form of Högström (1988)
378 (Metzger et al., 2013). For each of the 1000 m subintervals geolocated above the centres of
379 the landcover classification dataset an individual footprint weight matrix was calculated as
380 the subintervals were moved forward in space along the flight leg. This generated a footprint
381 weight matrix for every flight leg analysed (Figure 4.a). This matrix is used to weigh and
382 cumulatively sum the landcover contributions along the flight leg to give the space series of
383 land-surface contribution to the flux series (Figures 4.b, 4.c). Latent heat flux space series
384 presented in Figure 4.c is the same series whose cross-scalogram was presented in Figure
385 3.b.

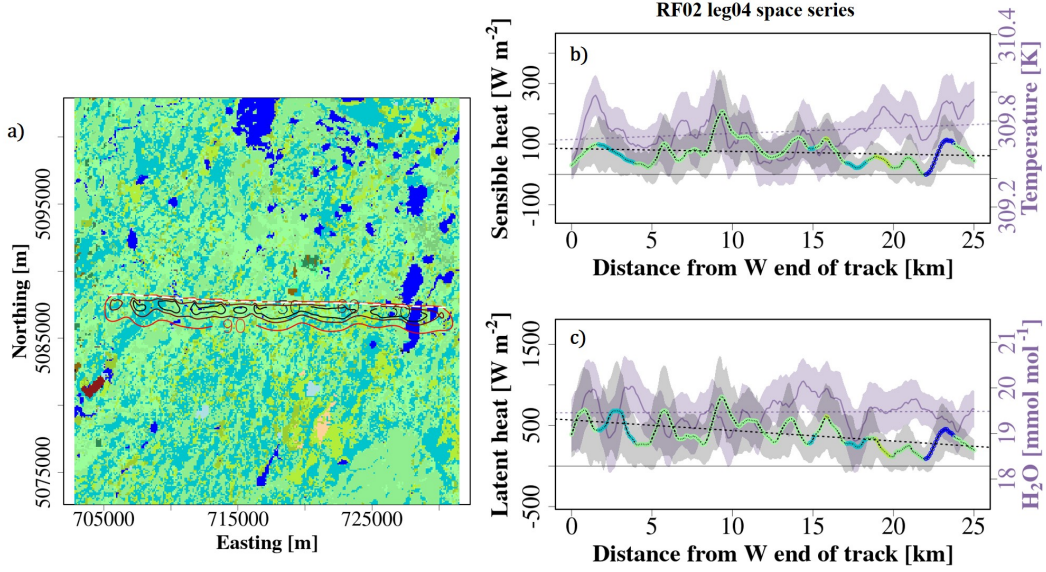


Figure 4: Footprint weights and window averaged flux space series calculated for RF02 flight leg 04. a) Cumulative flux footprint along the flight leg (shown in white dashed lines). Contour lines show 30, 60 and 90% source area contributions to the fluxes measured. b) Space series of measured air temperature (purple line) and calculated sensible heat flux (black line with coloured dots). Shading around each line indicate the random sampling errors. colour of the circles in the flux series indicate the dominating land cover type. Legend in Figure 1. c) Space series of measured water vapour mole fraction (purple line) and calculated latent heat flux (black line with coloured dots). Coloured and shaded the same as b. 251 flux estimates were calculated at each 100 m grid cells located below the flight leg as seen in a. Giving a 1000 m window averaged version of Figure 3.a.

386 To investigate how the flux contributions vary over the course of a research flight and
 387 spatially over the domain, the measured fluxes are back-projected to their surface source as
 388 gridded two-dimensional data following the flux topography method of Mauder, Desjardins,
 389 and MacPherson (2008). Flux topographies are the footprint-weighted flux contributions
 390 measured across the domain from the airborne data (Amiro, 1998). The flux topographies
 391 are calculated over a 10×10 km CHEESEHEAD19 domain sub-set at the 100 m resolution of
 392 the flux space series. The calculated fluxes are projected back to the surface grid, weighted
 393 at each grid cell by the cumulative flux footprint from all the sub intervals in a processed
 394 flight leg.

395 For each flight leg from a RF, a flux topography was calculated, then the cumulative
 396 footprint weighted contribution (F_{ij}) for a RF was calculated at each grid cell in space
 397 (Kohnert et al., 2017) according to Equation 5.

$$F_{ij} = \frac{\sum_j^N (\sum_i^M f_{i,j} * g_{i,j})}{\sum_j^N (\sum_i^M g_{i,j})} \quad (5)$$

398 In Equation 5, f denotes the flux magnitudes measured, g the footprint weights, with the
 399 number of flight legs going from j to N and indices i to M denoting the number of footprint
 400 weights. For example, for RF02 leg 04, the calculated flux space series (Figures 4.b and 4.c)
 401 were projected on to the flux footprint source area shown in Figure 4.a, weighed in space by
 402 the footprint weights. Source areas with low footprint values (< 0.05%) are excluded from

the analysis. This procedure was repeated for all the flight legs of RF02 using Equation 5 to calculate the cumulative, footprint weighted spatial distribution of the measured fluxes.

3 Results

We start by looking into the scale composition of the fluxes measured across the domain in Section 3.1. To illustrate the seasonal variation and evolution of measured turbulent and mesoscale fluxes we present the seasonally averaged and scale-separated contributions across the IOPs in Section 3.2. Following this, we present the domain-averaged and scale-separated diel data of the fluxes for each of the IOPs. Then the flight averages for all of the research flights analysed here are also presented. In Section 3.3 we discuss the observed relationship between mesoscale transport and local ABL stability. Then, we investigate the composition of land cover contributions within the footprint of flight legs and how those might relate to the observed mesoscale transport in Section 3.4.

3.1 Scale-resolved fluxes

Wavelet cospectra for the sensible and latent heat fluxes were calculated for all research flights analysed (Figure 4, 5, 6) to investigate the scale-resolved contributions to surface fluxes across the domain. The wavelet cross-scalograms from each flight leg were averaged across the space domain. These were then ensemble averaged across all flight legs that make up a research flight. The cospectra are not normalized to retain the relative magnitudes of the sensible and latent heat fluxes as well as to illustrate the flux magnitudes measured during the different flight campaign days. The flux cospectra follow a $2/3$ rd power law scaling in the small scales, indicating the inertial subrange of atmospheric turbulence (Kaimal & Finnigan, 1994). The cospectral power drops suddenly after about 7m, which is reasonable considering the spatial resolution of the UWKA high frequency data is 3 to 4 metres, with the average flight speed of 86 m/s and data resolution of 25 Hz. Both semi-log and log-log depictions are included to illustrate the spatial scales spanning the inertial subrange and turbulence production ranges as well as cospectral magnitudes and spectral power variability in the larger scales.

The latent heat flux cospectra calculated for research flights in the July IOP (Figures 5.a and 5.c) reveal a clustering of secondary maxima between 1 and 2 kilometres. The inertial subrange for most of the flights ends around 200 m, which would allow these peaks to be in the production scales for turbulence or signals of larger scale non-turbulent structures. The secondary maxima are less prominent in RF02 and RF03 LE cospectra, both with larger magnitude for the measured turbulent fluxes. Their peak is around a spatial scale of 800 m. The peak flux magnitude for the IOP is also from these two flights and is of the order of 1000 Wm^{-2} . However, the sensible heat flux cospectra for the July IOP do not reveal any such clustering. The cospectra in their log-log representation flatten out into the production scales of turbulence around 200 m for most of the flights (Figure 5.d). The magnitudes are also more variable between different flight days, with the peaks in the turbulence production scales reaching out to 300 Wm^{-2} . H cospectral power reduces for the spatial scales larger than 2 km while the LE cospectra still has power in the larger scales.

The prominent clustering of secondary peaks is no longer present in the latent heat flux cospectra for the August IOP research flights (Figure 6.a). Cospectra for RF 15 and RF 16 show maximum flux magnitudes around spatial scales of 2000 m and 1200 m respectively (Figures 6.a and 6.b). Research flights 10, 11 and 12 have LE local maxima around spatial scale of 500 m to 1 km. These three flights measured peak latent heat flux magnitudes of the order of 1000 Wm^{-2} while the other flights have their maxima around 600 Wm^{-2} . For the LE cospectra, spectral power in the large scales are similar order of magnitude as the July IOP measured values. The sensible heat flux cospectra for August IOP (Figure 6.a) are similar to the July IOP cospectra. They are broader in the turbulence production scales than the latent heat flux cospectra (Figure 6.b), with spatial scales ranging from 300 m to

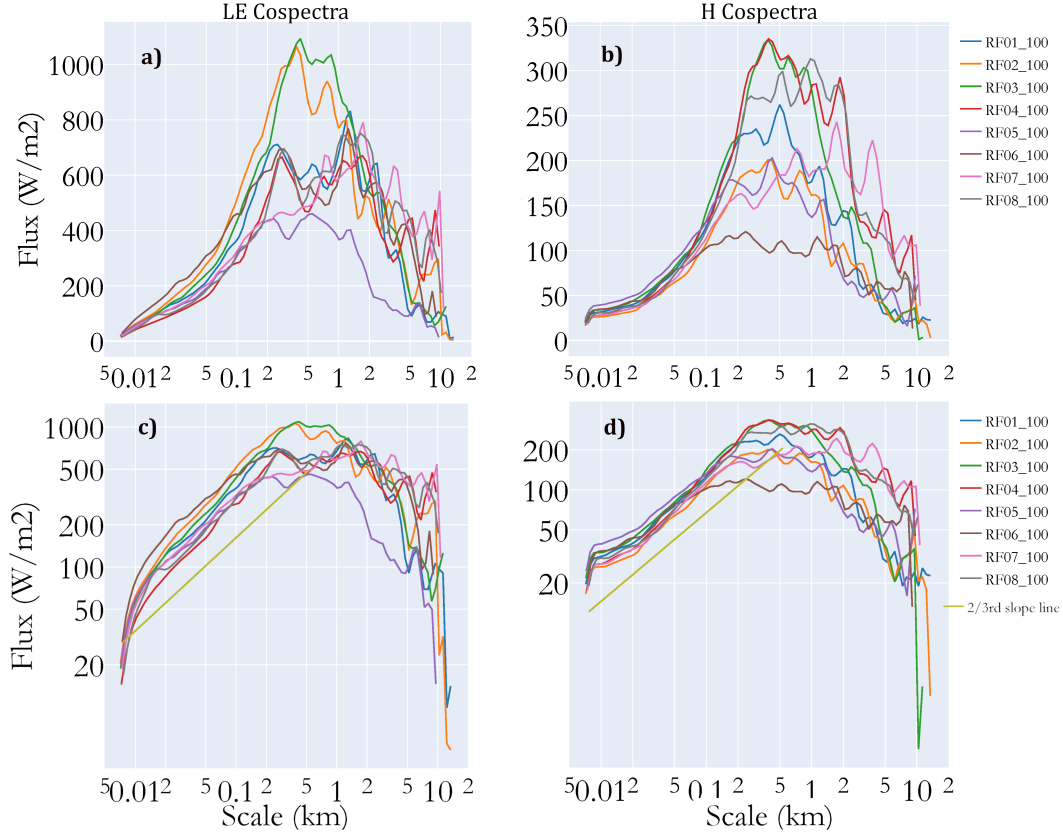


Figure 5: Wavelet cospectra for latent (a,c) and sensible heat (b,d) fluxes measured during each research flight at 100m above ground during the July IOP. Cospectra were calculated for each flight leg during the research flights and then ensemble averaged over all the flight legs used in the analysis. The first row, shows a semi-log depiction and the second row shows a log-log representation. Different colours indicate different Research Flights and the 2/3 slope line.

2 km. RF09 has stands out with a low measured H cospectral power due to a rain event during early morning. Apart from this research flight, the other flights measured peak fluxes in the 200 to 300 Wm^{-2} range.

Most of the sensible heat flux cospectra for research flights in the September IOP show a shorter range of spatial scales in the turbulence production scales (Figure 6 d). Research flights 17 and 18 stand out with a broader range of spatial scales in the turbulence production range. The peak cospectral power for sensible heat fluxes are also higher in the September IOP, with values reaching around 400 Wm^{-2} . Compared to the July and August sensible heat flux cospectra, the September cospectral data show lesser power in the larger scales. The latent heat flux cospectral peaks are smaller than the values in the other two IOPs and more variable between different flight days. LE cospectra for RF 19 has a maximum around 800 Wm^{-2} while RF 17 has a double maxima, both around 300 Wm^{-2} . Such a prominent double peak nature is only seen in the RF17 LE cospectra, with the first maxima around 200 m spatial scale and the second one at 1200 m. A more diffused double peak structure is seen in the cospectra for RF 19, where the peaks are of the same order of magnitude, at around 400 m and 1 km.

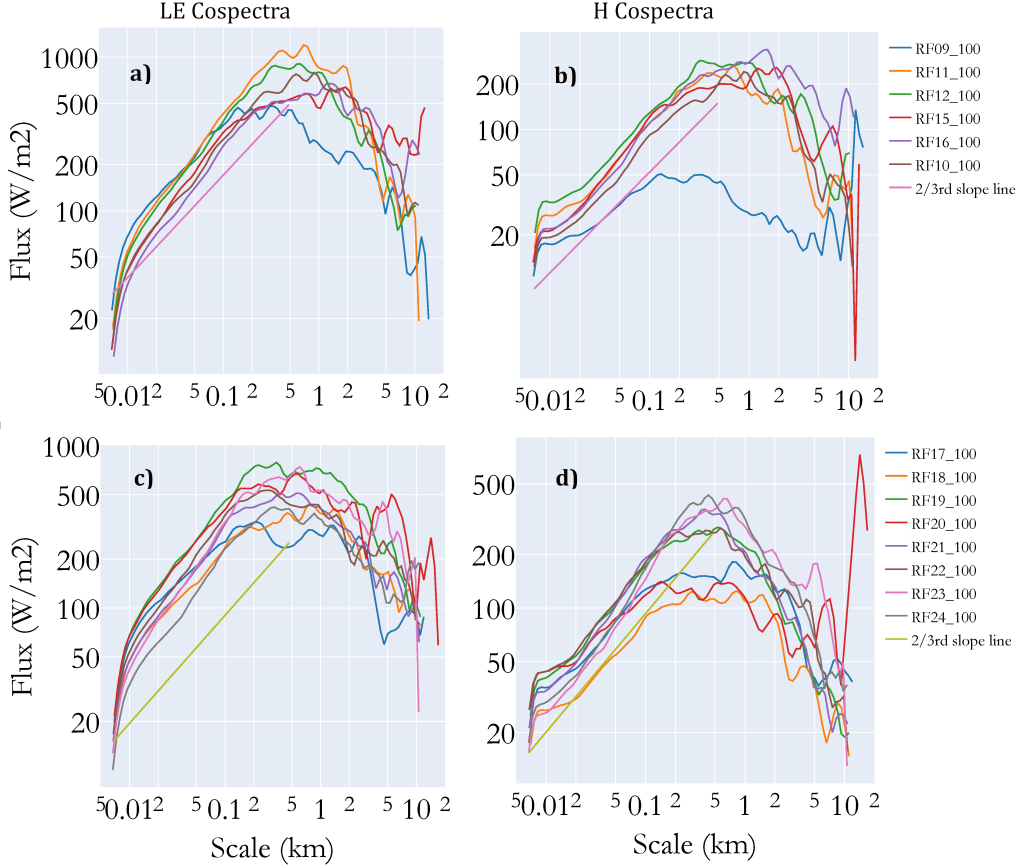


Figure 6: Wavelet cospectra for latent (a,c) and sensible heat(b,d) fluxes measured during each research flight at 100 m above ground during the August(a,b) and September(c,d) IOP. The first row show cospectra for the August IOP flights and the second row show cospectra for the September IOP flights. Cospectra were calculated for each flight leg during the research flights and then ensemble averaged over all the flight legs used in the analysis. Different colours indicate different Research Flights and the 2/3 slope line.

469 The heat flux cospectra do not show a distinct separation of the energy producing
 470 turbulent scales and mesoscales of atmospheric motion. The ABL height provides a theo-
 471 retical maximum for the largest scales of atmospheric turbulence. ABL height was measured
 472 during the IOP days by two Radiometrics MP-3000A Microwave Radiometers (MWRs)
 473 deployed roughly 45 km west and south to the Ameriflux tall tower (locations in Figure 1.a
 474 Duncan Jr et al. (2022) and data available from Adler et al. (2021)) at the Lakeland
 475 and Prentice airports in Wisconsin. Duncan Jr et al. (2022) gives an overview of the instruments
 476 and presents a validation of the ABL height data with radiosonde measurements during the
 477 field experiment. Figure 7 presents the distribution of the hourly averaged boundary layer
 478 height measurements, averaged over both the instruments and colored by the time of day.
 479 Little change is observed in the median ABL height measured across the IOPs. The bound-
 480 ary layer height increase with the development of the convective boundary layer can also
 481 be seen. During the July IOP, save for three data points, most values are bound between
 482 300 m and 1500 m. The range of values broaden for the next two IOPs. For the August
 483 IOP, the boundary layer height measurements range from 200 m to 1800 m and for the
 484 September IOP they range from 200 m to 2000 m. These measurements indicate that 2 km
 485 is a reasonable order of magnitude threshold for the large scale structure/transport across

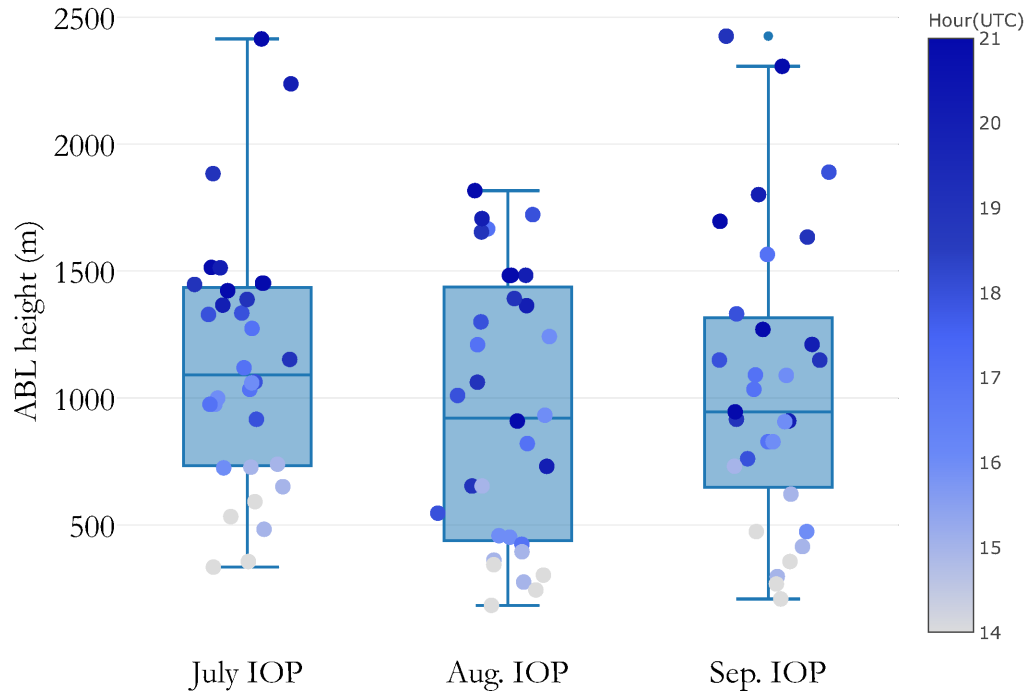


Figure 7: Distribution of hourly Microwave Radiometer measured ABL height during the IOPs (data from Adler et al. (2021)), colored by the time of day.

486
487

the IOPs and can help partition the contributions from the largest scales of boundary layer turbulence and mesoscale structures.

3.2 Seasonal and diurnal variations

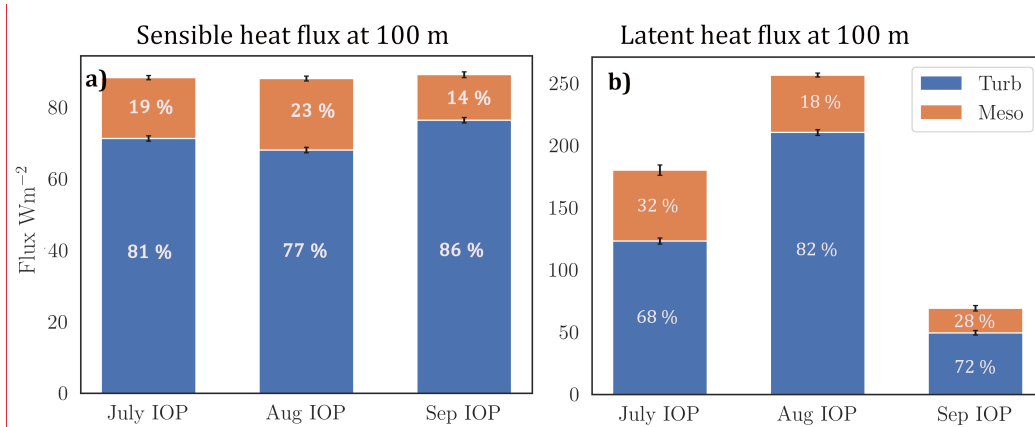


Figure 8: Mean turbulent (blue) and mesoscale (orange) (a) H and (b) LE fluxes for the three IOPs showing seasonal flux transitions. The flux percentages of the total are shown in white within the bars.

IOP averaged flux magnitudes reflect the seasonal shift in the landscape (Figure 8). IOPs were conducted from late summer in the start of July to early autumn at the end of September 2019. In July the study domain is latent heat flux-dominated and towards the end of September as senescence starts to set in, it transitions to a sensible heat flux-dominated landscape. The mean sensible heat flux magnitude for all scales does not change substantially between the three IOPs and remains around $89 Wm^{-2}$. However, there is a substantial variation in the magnitudes of the latent heat fluxes measured across the months. The measured total LE is higher than the total H in the July and August IOPs, increasing from $179 \pm 5 Wm^{-2}$ to $256 \pm 3 Wm^{-2}$ and then reduces to $69 \pm 3 Wm^{-2}$ in the September IOP (Figure 8 and Table S1), falling below the total sensible heat flux measured ($89 \pm 1 Wm^{-2}$). The percentage mesoscale and turbulent contributions to the total measured fluxes also show a seasonal variation for the sensible and latent heat fluxes. For the sensible heat flux, the percentage turbulent contribution for the July IOP is 81%, which reduces to a further 77% in August and then increases to 86% in September. Similarly, for latent heat fluxes, the percentage turbulent contribution for the July IOP is the least, at 68%, increasing to 82% in August and then decreasing to 72% for September. When a particular heat flux dominated the surface atmospheric exchange it also had the lowest percentage mesoscale contribution among the IOPs. In August when the total (turbulent + mesoscale) latent heat flux magnitude is at its maximum at $256 \pm 3 Wm^{-2}$, the mesoscale fraction of the same is at its minimum, at 18%. Similarly, when the evaporative fraction is at its minimum September at 0.76, the sensible heat mesoscale fraction is also at a minimum at 14%.

The sensible heat flux data averaged across the domain and all flight days shows a diurnal cycle for all of the IOPs (Figure 9 column 1, black lines). The calculated turbulent scale fluxes follow the same patterns closely, but mesoscale fluxes do not. For the July IOP data, the total sensible heat flux peaks at $128.8 \pm 1.31 Wm^{-2}$ around 16:20 UTC. In August the sensible heat flux maximum is of the same order, at $121.1 \pm 1.3 Wm^{-2}$ but shifted to later in the afternoon around 20:20 UTC (Figure 9.c). The measured fluxes in the August IOP also show sustained values of the order of $100 Wm^{-2}$ from late morning to after noon (15:50-20:30 UTC) until later in the day towards the end of the afternoon. The September IOP sensible heat flux data has a more pronounced peak at $148.7 \pm 1.5 Wm^{-2}$. Our scale analysis reveals that this clear diurnal signal is present only for the turbulent scale fluxes

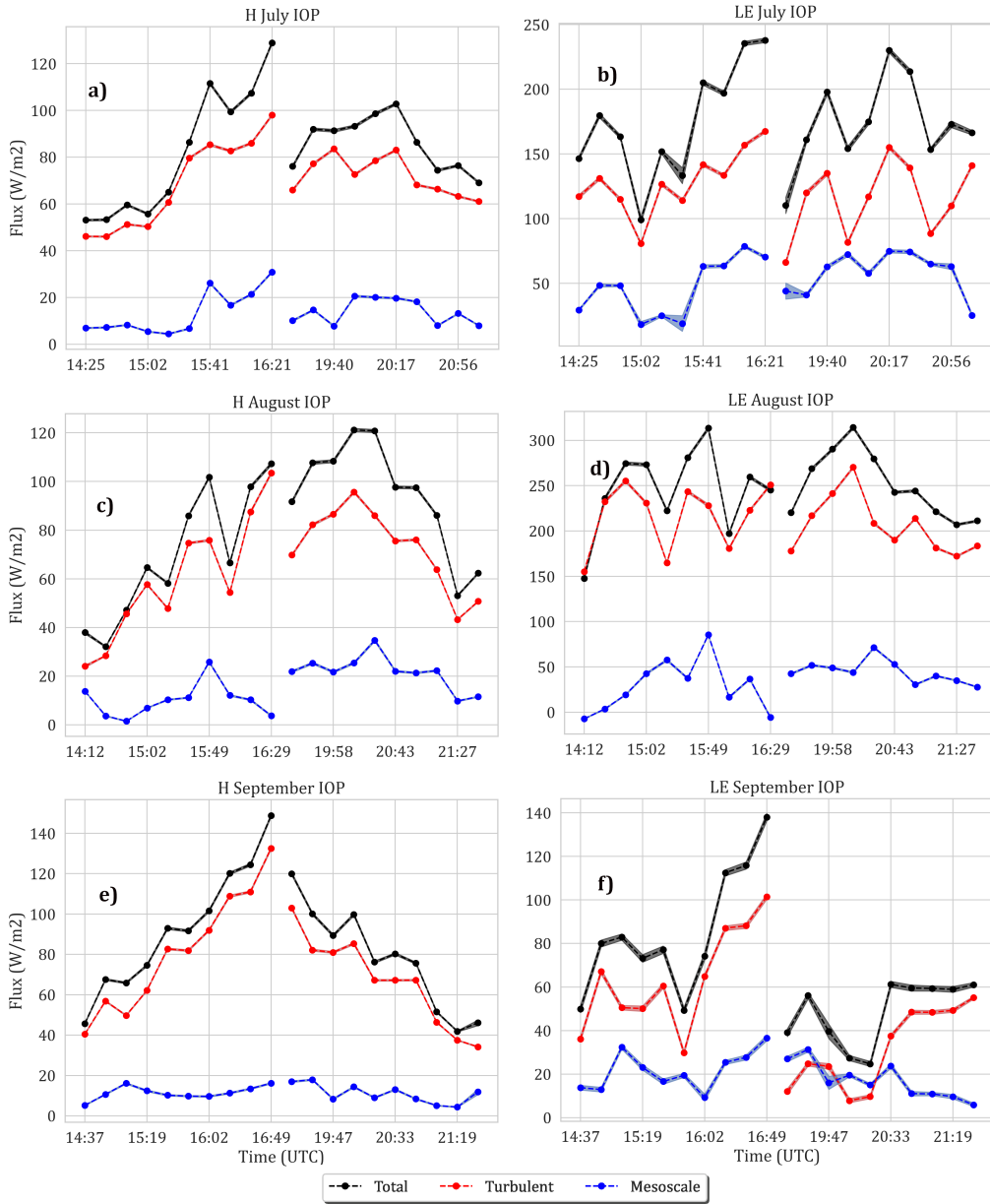


Figure 9: H and LE fluxes averaged for flight legs at the same time across all analysed days for the three IOPs. Every day had 2 RFs, a morning and afternoon flight. Every flight had 20 flight legs, numbered 1 to 20. Each data point is the mean value of fluxes measured from all flight legs at the same time of day in an IOP. The scale-resolved diel time series is shown. x axis shows the mean time of those flight legs in UTC. Since the x axis is ordered according to the flight leg timings, the 2.5 hours break between the end of the morning leg and the start of the afternoon leg is included as discontinuities in the plots. The first column shows the sensible heat flux values (subplots a, c and e) and the second column shows the latent heat flux values (subplots b, d and f). Each row shows data for an IOP (a,b July IOP; c,d August IOP; e, f September IOP).

521 which follow the total fluxes diel pattern closely for most of the flight day. In the July IOP
522 the calculated mesoscale sensible heat fluxes peak around $30.8 \pm 0.8 \text{ Wm}^{-2}$ before noon
523 and in the afternoon there are sustained values around 20 Wm^{-2} till later in the evening
524 towards the end of the research flights. This can also be seen reflected in the difference
525 between the total and turbulent flux diel plots in Figure 9 a. Similarly for the August IOP,
526 mesoscale fluxes show sustained values in the afternoon around 25 Wm^{-2} , peaking at 34.8
527 $\pm 1 \text{ Wm}^{-2}$. Sensible heat mesoscale values are the lowest in the September IOP as observed
528 earlier in the IOP averaged data. The median value for the IOP data is 11 Wm^{-2} , and the
529 maximum value observed was $18 \pm 0.7 \text{ Wm}^{-2}$ around 19:30 UTC.
530 The latent heat fluxes do not show such a clear diurnal variation for the domain averaged
531 data. The domain averaged flux magnitudes are of the same order of magnitudes as the
532 IOP averaged values presented earlier.

533 The total fluxes measured for all research flights analysed is presented in Figure 10.
534 This picture at a research flight level reflects the seasonal variation detailed in Figure 8.
535 Flux measurements from RF 2 (July 9th afternoon) and RF 3 (July 11th morning) stand
536 out in the July IOP data (July 09 - 13) with total fluxes measured at 430.2 Wm^{-2} and
537 436.5 Wm^{-2} . This is due to increased contributions from turbulent latent heat fluxes for
538 the two flights (Figure S2). The mesoscale contributions measured were of the same order of
539 magnitude as other days of the IOP. Similarly, RF 23 (Sep. 28th morning) stands out in the
540 September IOP (Sep. 24 - 28) with measured turbulent fluxes the same order of magnitude
541 as the late summer IOPs. This was due to an increase in the measured turbulent latent
542 heat fluxes (Figure S6) due to a rain event earlier that day.

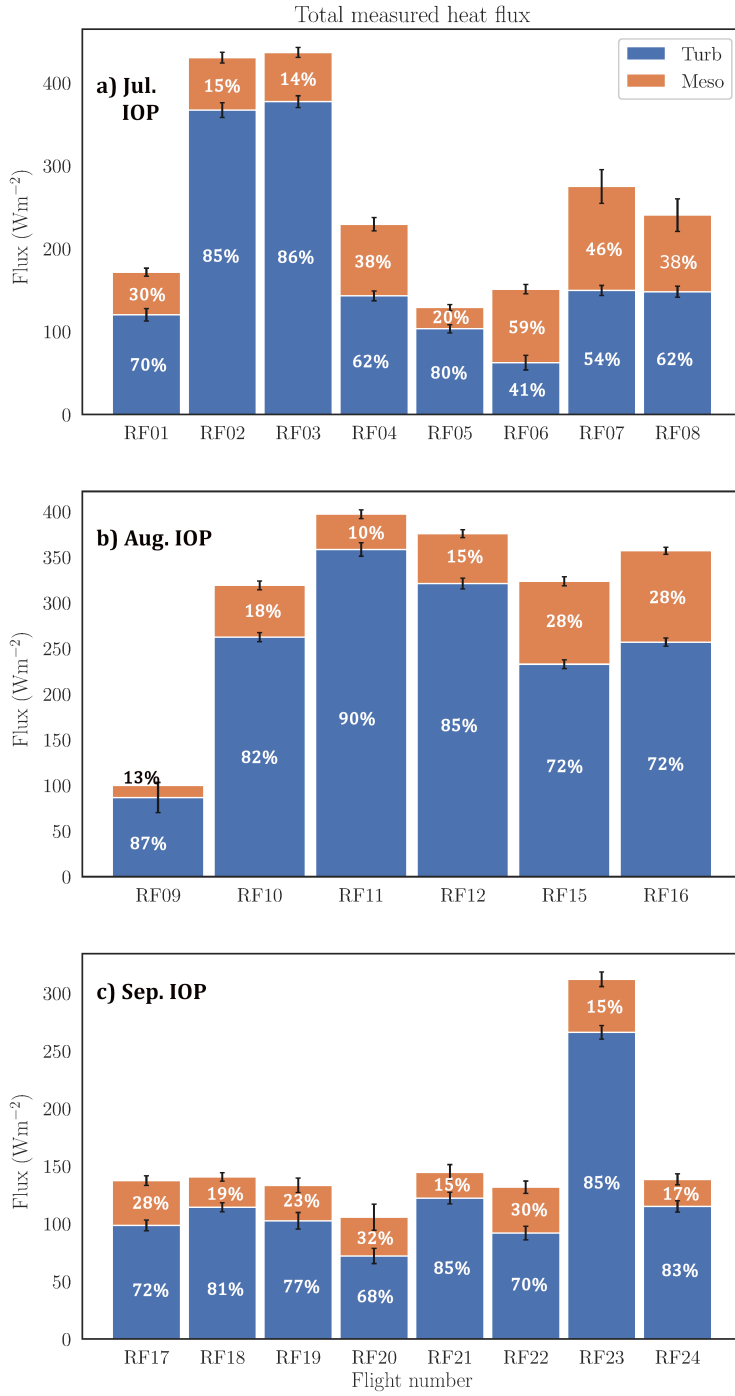


Figure 10: Total ($H + LE$) fluxes measured on each research flight for all the processed research flight data. The first (a) panel shows flights for the July IOP, the second (b) panel for the August IOP and the third (c) for the September IOP. Each bar graph represents the mean, scale-resolved flux for a research flight. The x axis shows the research flights and y axis flux magnitudes. Turbulent fluxes in blue and mesoscale fluxes in orange. Percentage contributions in white numbers.

543

3.3 ABL and land–surface drivers of transport

544

3.3.1 ABL dynamics

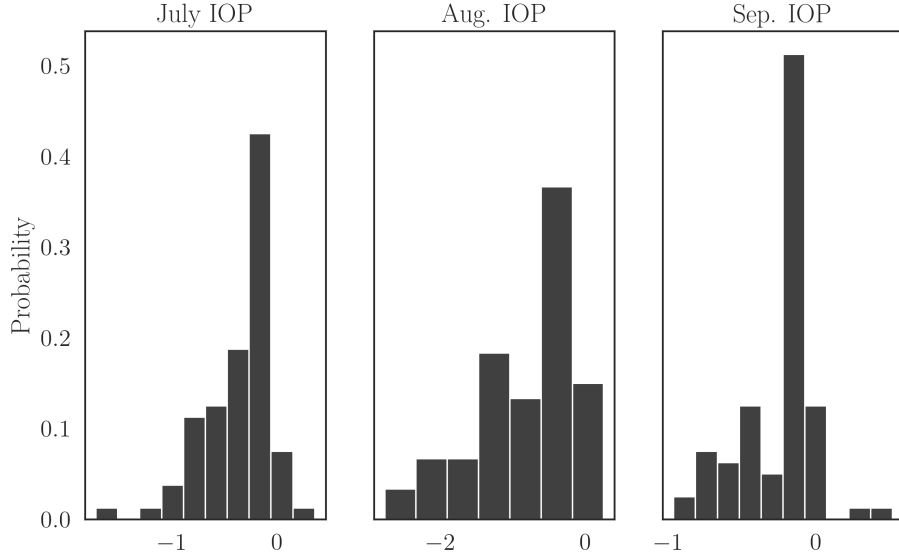


Figure 11: Probability distributions for the atmospheric boundary layer stability parameter, ζ for the three IOPs. ζ values were calculated over 1000 m subintervals along a flight leg. The median values calculated per flight leg are presented here.

545

546

547

548

549

550

551

552

553

554

555

The Obukhov length (Obukhov, 1946; Monin & Obukhov, 1954) was calculated for each of the 1000 m flux calculation windows (Section 2.4) as $L = -u^{*3}\overline{\theta_{v0}}/kgQ_{v0}$. Here, u^* is the measured surface friction velocity (turbulent velocity scale representative of surface shear stress); $g/\overline{\theta_{v0}}$, a buoyancy parameter where g is the gravitational acceleration and $\overline{\theta_{v0}}$ the average surface virtual potential temperature; k is the von Kármán constant set as 0.4 and Q_{v0} the calculated surface kinematic vertical heat flux ($\overline{w'\theta'_v}$) of the virtual potential temperature θ_v . The values used for u^* , $\overline{\theta_{v0}}$ and Q_{v0} were the local averages calculated over the 1000 m spatial subintervals. Since L has units of length, a non-dimensional turbulent surface layer stability parameter $\zeta = \frac{z}{L}$, where z is the measurement height, can be defined (Stull, 1988). Negative values of ζ close to 0 indicate a statically neutral surface layer and as the value decreases, the surface layer becomes more statically unstable.

556

557

558

559

560

561

562

ζ values were calculated like so for all the flight legs analysed giving 250 to 300 values per space series for every leg. The median values were calculated for every flight leg as representative of the spatial transect over the heterogeneous domain. Normalised histograms of median ζ values show that the August IOP is more convective than the other two IOPs with more data points within the $\zeta < -1$ range (Figure 11). On the other hand the September IOP looks strongly shear driven, with most of the data falling within $\zeta \in [-1, 0)$. In this regard, the July and September IOPs seem to be dynamically similar.

563

564

565

566

567

To understand how scale-separated contributions vary with ABL dynamics, we compare the probability density functions (PDFs) of mesoscale flux fractions between shear driven ($\zeta \in (-1, 1]$) and convectively driven ($\zeta \in (-20, 1]$) ABLs. The mesoscale fractions of the total flux contributions are calculated for each of the 1000 m subintervals for sensible and latent heat flux space series. Based on the calculated ζ values of their subinterval,

568 the mesoscale flux fraction data were grouped into neutral and unstable categories for all
 569 three IOPs. For all six subsets, outlier removal was done for the mesoscale percentage
 570 values based on median absolute deviations (Iglewicz & Hoaglin, 1993). Using data from all
 571 the subintervals gives us a good number of data points for robust statistical analysis. For
 572 N_s denoting the number of data points for neutral, shear driven ABL and N_c denoting the
 573 number of data points for unstable, free convectively driven ABL, the July IOP data had
 574 $N_s = 15428$ and $N_c = 2203$. Likewise, for the August IOP $N_s = 9298$ and $N_c = 5158$, and
 575 for the September IOP $N_s = 17041$ and $N_c = 1308$.

576 Kernel density estimations (KDEs) are used to calculate PDFs from the airborne spatial
 577 data. KDEs are a way to estimate the continuous, non-parametric PDF of a given distribu-
 578 tion of random variable using smoothing window functions or kernels (Scott, 1979, 2015). A
 579 histogram of the data can provide a non-parametric estimate of the underlying probability
 580 density when the bin counts are normalised by the total sample size and multiplied by the
 581 bin width. This conventional discrete PDF representation of the data in a histogram uses
 582 stacked rectangular bars. In KDEs, a window function (such as a Gaussian kernel with a
 583 chosen bandwidth) is employed instead of rectangular bars to estimate a continuous PDF
 584 of the data.

585 In this study we use Gaussian kernels with a sample size depended band width, given by
 586 a rule-of-thumb bandwidth estimate $h = N^{-1/(1+d)}$, where N is the number of data points
 587 and d the number of dimensions (1 for the univariate distributions here) following Scott
 588 (2015). PDFs were calculated using KDEs for the mesoscale flux fraction distributions in the
 589 neutral and unstable regimes. For the sensible heat flux distributions, the two distributions
 590 were found to be significantly different from each other for all 3 IOPs using the Mann-
 591 Whitney U rank test with 95% confidence. The PDFs show statistically significant higher
 592 fraction of mesoscale transport observed in convectively driven ABLs across all the three
 593 IOPs (Figure 12).

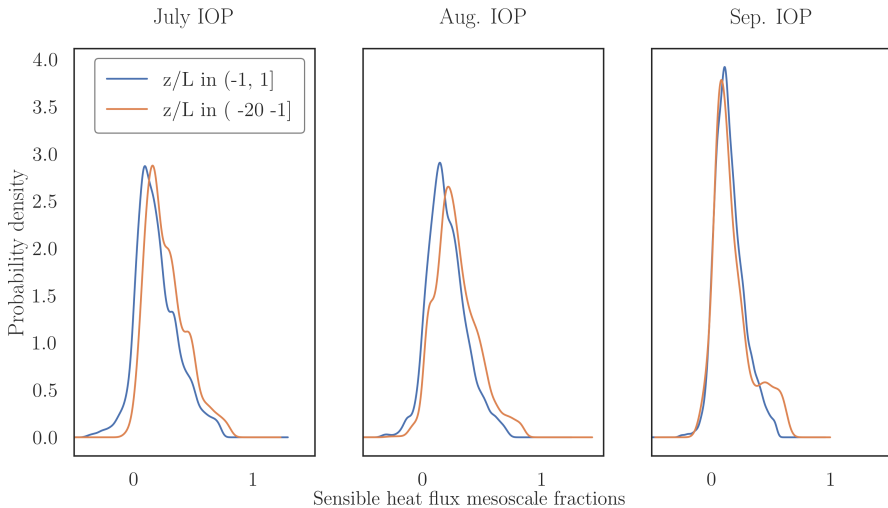


Figure 12: Probability density functions for sensible heat flux mesoscale fractions calculated from kernel density estimates. Mesoscale flux fractions of the total fluxes were calculated over 1000 m subintervals for the flux space series from every flight leg.

594 For latent heat fluxes, the kernel density estimates of mesoscale fraction distributions
 595 for the July and August IOPs show higher mesoscale fluxes for convective cases (Figure
 596 13). Performing a Mann-Whitney U rank test again showed that the distributions are sig-

597 nificantly different for the two stability regimes at 95% confidence. However, for September
 598 IOP the mesoscale transport does not have a preference between a shear or convectively
 599 driven ABL. Even though July and September IOPs have similar ABL stability distribu-
 600 tions their latent heat mesoscale transport does not show the same behaviour, hinting at
 the role of seasonality through changing surface characteristics and insolation.

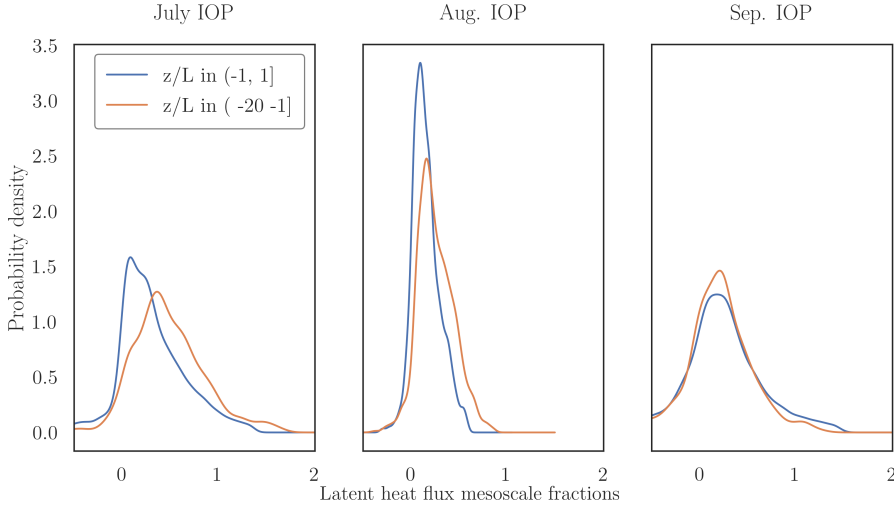


Figure 13: Probability density functions for latent heat flux mesoscale fractions calculated from kernel density estimates. Mesoscale flux fractions of the total fluxes are calculated over 1000 m subintervals for the flux space series from every flight leg.

601

602 The PDFs of sensible and latent heat mesoscale fractions show values when the flux
 603 fractions are > 1 and < 0 (albeit near-zero for the sensible heat distributions when mesoscale
 604 fractions are > 1). These occur when the measured mesoscale and turbulent fluxes are out of
 605 phase with each other. For both sensible and latent heat fluxes, the histograms of turbulent
 606 and mesoscale fluxes when the mesoscale fraction is greater than 1 show higher, positive
 607 values of mesoscale fluxes and lower negative values of turbulent scale fluxes (Figure S8).
 608 Indicating that the mesoscale fluxes dominate such instances, driving the fraction to be
 609 over 1. Similarly for mesoscale fractions < 0 , the sensible heat flux histograms for scale-
 610 resolved fluxes show higher, positive values for turbulent fluxes and lower negative values
 611 for mesoscale fluxes causing the mesoscale fraction of the total flux to be negative (Figure
 612 S7). The same phase difference between turbulent and mesoscale fluxes can be seen in the
 613 latent heat fluxes too, although they behave more uniformly.

614 The surface layer friction velocity, u^* can capture the magnitude of surface Reynolds'
 615 stress as a velocity scale. For the 1000 m spatial subintervals it is calculated from the
 616 vertical momentum fluxes as $u^* = (\overline{u'w'^2} + \overline{v'w'^2})^{1/4}$. Similarly, the convective velocity scale
 617 $w^* = (\frac{g}{\theta_v} z_i \overline{w'\theta_v})^{1/3}$ captures the importance of free convection as a velocity scale. It follows
 618 that, u^*/w^* is a non-dimensional parameter that can succinctly capture the competing
 619 effects of free and forced convection in the ABL. If the ABL is strongly shear driven, one
 620 would expect higher u^* values and lower w^* values, leading to higher values for u^*/w^* and
 621 vice versa for a free convectively driven ABL. Kernel density estimates of u^*/w^* calculated
 622 reflect the ζ distribution characteristics for the 3 IOPs seen earlier in Figure 11. September
 623 IOP has a median u^*/w^* value of 0.55, higher than the July (0.45) and August (0.43) IOPs,
 624 indicating more shear driven surface atmospheric transport. Similarly, the distributions for

625 July and August IOPs were also similar, with the august IOP having a slightly lower median
 626 value indicating more convectively driven transport.

627 A binned scatter plot can help to succinctly visualise non-parametric relationship be-
 628 tween two random variables. It has been a popular tool in applied microeconomics to
 629 visualise the conditional expectations in large datasets (Chetty & Szeidl, 2005; Chetty et
 630 al., 2009; Starr & Goldfarb, 2020). We use the *binsreg* in Python ([https://nppackages](https://nppackages.github.io/binsreg/)
 631 [.github.io/binsreg/](https://nppackages.github.io/binsreg/)) as introduced in Cattaneo et al. (2019). The number of bins for
 632 the independent variable of interest is calculated such that it minimises the integrated mean
 633 squared error of the binned scatter (much like a piece wise linear regression). The distri-
 634 bution of the predictor variable is then divided into equal quantiles corresponding to the
 635 chosen number of bins and the conditional means of the second variable is calculated.

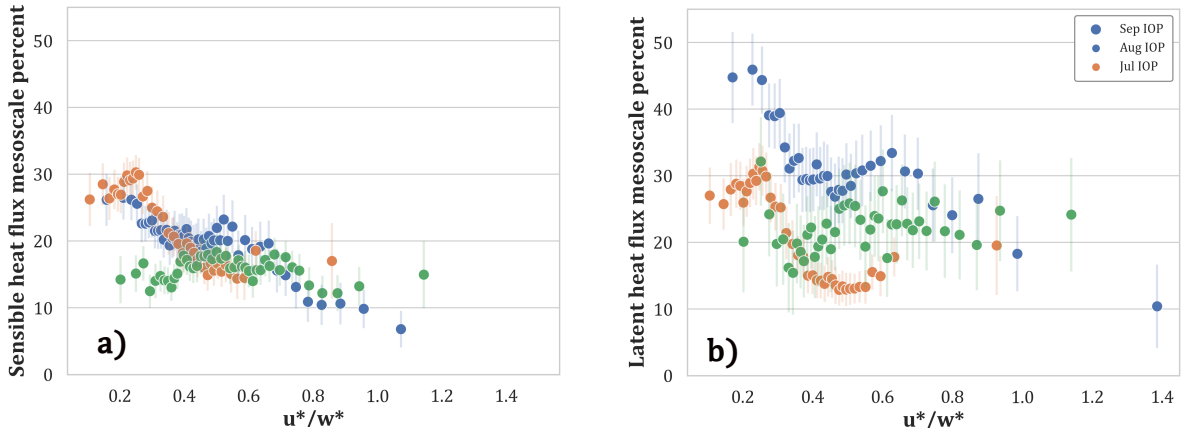


Figure 14: Binned scatter plots of mesoscale flux percentages vs u^*/w^* for all three IOPs. Bin values of the flux fractions plotted are calculated as conditional means for the u^*/w^* bins. 95% confidence limits of the mean values are shown as vertical lines at each bin estimate.

636 The mesoscale H percentages show a decreasing trend with increasing u^*/w^* values
 637 in July and August IOPs indicating higher mesoscale transport during more convective
 638 scenarios (Figure 14.a). This is especially clear in the almost flat scatter for the shear driven
 639 September IOP data which also has lower magnitudes, with the same order of magnitude
 640 throughout the range of u^*/w^* values. The highest values in July and August IOPs are of the
 641 same order of magnitude. July IOP shows the lowest percentage values for $u^*/w^* \geq 0.7$.
 642 The latent heat mesoscale flux percentages do not behave similarly to the sensible heat
 643 flux mesoscale fractions (Figure 14.b). Mesoscale fractions measured during the July and
 644 August IOPs are higher at lower u^*/w^* values but they are not of the same magnitude.
 645 This separation between the magnitudes of the July and August IOP values persists across
 646 the range of u^*/w^* values although both the scatters have similar shapes. The August IOP
 647 has lower mesoscale LE percentages at lower u^*/w^* values than the July IOP unlike the H
 648 mesoscale percentages. The August IOP data also shows the lowest values for mesoscale
 649 LE percentages for $u^*/w^* > 0.4$ while July IOP values are consistently the highest across
 650 the u^*/w^* range. The same behaviour is seen in the IOP averaged mesoscale percentages
 651 in Figure 8.b where the mesoscale LE percentage for August IOP is the lowest at 18%.
 652 Meanwhile, the LE mesoscale percentages during the more shear driven September IOP
 653 for $u^*/w^* > 0.4$ show values higher than August IOP. Figure 8.b also shows high (29%)

mesoscale fluxes for LE in the September IOP. There is also more variation in the September IOP LE values when compared with the H mesoscale percentages for the same time.

3.3.2 Flux contributions by land cover

The land cover class data from wiscland 2.0 database as shown in Figure 1 for the 40×40 km domain was grouped into open water (9% domain area composition), wetlands (34%), deciduous broadleaf forests (30%), shrubs/grass/open land (3.5%), coniferous (22%) and mixed forests (1.3%). Fractional footprint contributions from each of the land cover classes were calculated for each research flight (Figure 15). Wetlands dominate the footprint contributions to the measured fluxes across IOPs as they do for the study domain surface area. They were most prominently sampled during the September IOP research flights of September 24th and 26th, when the UWKA flew a South-East flight pattern with moderate to strong Southerly and South-Westerly winds (Table 1). Further breaking down the wetland class, we find that most of the contributions come from the forested wetlands that account for 27% of the domain area. The deciduous broadleaf forests and conifers were sampled fairly equally across the IOPs. Although open water bodies showed strong local contributions to the flux space series (For example the blue dots highlighted in the space series shown in Figure 4.b and 4.c) the averaged contribution during a research flight reflect their lower percentage area composition.

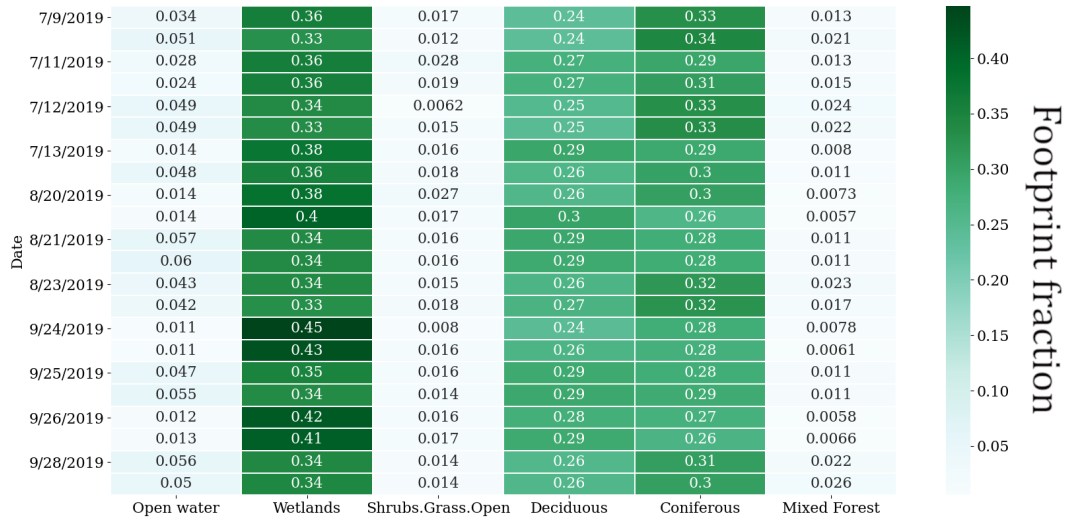


Figure 15: Heat map of fractional footprint contributions from the major land cover classes within the study domain for each research flight. The land cover classes are presented in columns and the airborne campaign dates are presented along rows. The first row for every date corresponds to the morning flight and the second row the afternoon flight. The numbers inside the boxes show fractional footprint contributions and they are coloured according to the colour bar

For a more detailed investigation of flux footprint contributions with time, IOP averaged, scale-separated footprint contributions were calculated (Figure 16). For all research flights analysed, the land cover class with the maximum footprint contribution to the measured fluxes at each 1000 m subinterval was picked. This was then grouped by their respec-

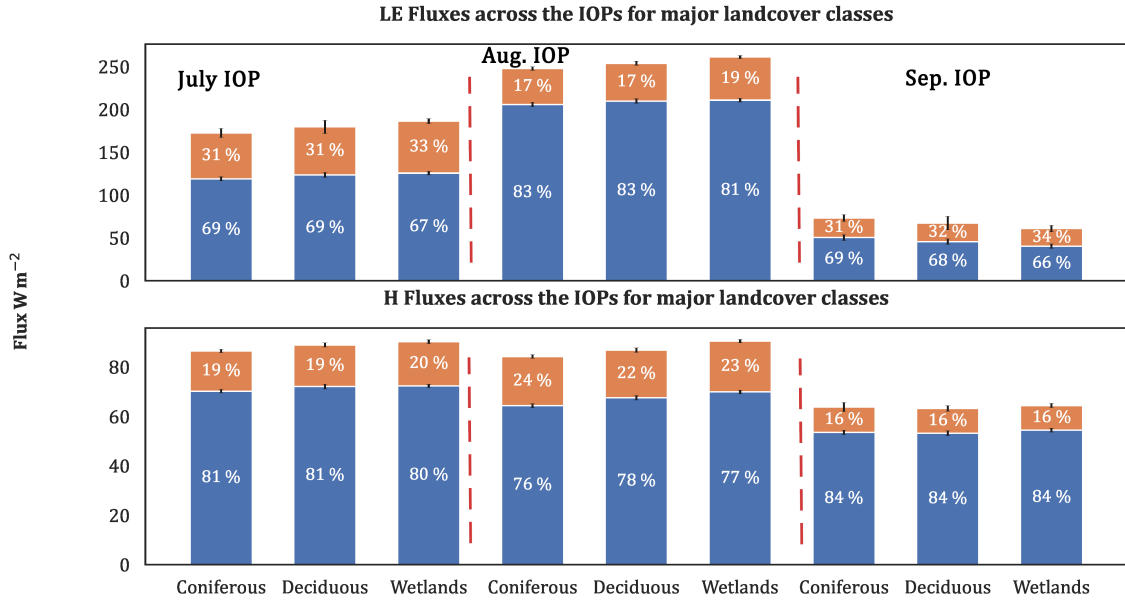


Figure 16: Turbulent and mesoscale sensible and latent heat fluxes measured for the major land cover classes across the IOPs. Turbulent fluxes in blue and mesoscale fluxes in orange. Panel on top shows the LE and panel at the bottom shows H. Bar graphs for each of the three IOPs are separated by vertical dashed red lines and ordered as contributions from coniferous, deciduous forests and wetlands within each IOP group.

676 tive IOP to calculate the scale-separated fluxes for each IOP from all the land cover classes.
 677 The same overall pattern across the IOPs seen in Figure 8 is repeated in Figure 16 as well,
 678 with regards to the magnitudes of the fluxes across IOPs and the scale-resolved percentages.
 679 The sensible heat flux magnitudes measured are fairly consistent across the IOPs while the
 680 latent heat fluxes show strong seasonality between the IOPs. Although wetlands contribute
 681 the most to flux footprints, the scale-composition of the fluxes do not change substantially
 682 between the land cover classes. The highest mesoscale LE percentage was measured in the
 683 September IOP with all the major landcover classes averaging around 32% and the most H
 684 mesoscale percentage values were measured in the July IOP, averaging at 23% between all
 685 3 land cover classes.

686 The kernel density estimates for mesoscale fractions did not show significant differences
 687 between the three major land cover classes.

688 3.4 Space scale resolved fluxes

689 We present a case study for one good flight, with a sample flux topography for a
 690 summertime morning flight, RF03, conducted on July 11th, 2019 from 09:20 to 11:30 CDT
 691 (Central Day Time, 5 hours behind UTC). The flight did east-west transects across the
 692 domain, starting from the northern edge and moving to the south. Aircraft logs for the
 693 day mention observing shallow cumulus clouds indicating local convection and weak winds
 694 for this day. This ensured that the flight transects had a good footprint coverage over the
 695 domain for this research flight.

696 Spatially resolved sensible and latent heat flux topography maps (Figure 17.a) show
 697 similar order of magnitude values as the IOP averaged behaviour in Figure 8. The spatial
 698 distribution patterns of both the fluxes do not look similar with latent heat flux showing more
 699 spatial variability than the sensible heat flux and dominating over the latter. The percentage
 700 mesoscale contributions for the two fluxes are qualitatively similar over the western part of
 701 the domain but show differing spatial patterns towards the eastern sections (Figure 17.b).
 702 These flux topographies illustrate the fact that the CHEESEHEAD19 tower sites inside the
 703 study domain sample differing Bowen ratios within the same 10×10 km domain and there are
 704 spatially varying, concomitant mesoscale surface-atmospheric transport. This would imply
 705 that not all of the towers are sampling the same flux transport and the mesoscale transport
 706 associated with their locations would also be different. The flux topographies indicate
 707 stronger mesoscale contributions towards the southern edge of the domain in the sensible
 708 heat flux plots (Figure 17.b). This is due to the inherent time dependency in calculating the
 709 topographies from the flight transects. Each research flight duration is about 2 hours. This
 710 particular flight started measurements at the north end of the domain in early morning and
 711 by the time it reached the southern edge it was close to noon and by then a fully developed
 712 CBL would have formed. Sensible heat mesoscale fluxes develop more later in the day as
 713 well (Figure 9.a, 9.c). The scale-resolved fluxes for latent heat for this flight indicate that
 714 the turbulent and meso peaks do not align in space (Figure 18.a). Flux topographies for
 715 research flights in the August and September IOPs are presented in the supplement along
 716 with the standard error percentages for the footprint weighted fluxes (Gatz & Smith, 1995)
 717 following Kohnert et al. (2017).

718 The inherent time dependency of the topographies leads to source strength non-stationarity,
 719 since the surface heat flux magnitudes change over the course of the measurement. This
 720 makes the flux topographies harder to interpret. A fusion Land Surface Temperature (LST)
 721 product over the domain (Desai et al., 2021) for the measurement time shows a high ampli-
 722 tude west-east band in the centre (Figure 18.b). Mesoscale gradients can be observed close
 723 to this band in the latent heat flux plots of Figures 18.b and 18.c. However, since the large
 724 scale transport would be from quasi stationary structures we can't directly link the same to
 725 land cover or LST gradients in our current analysis framework.

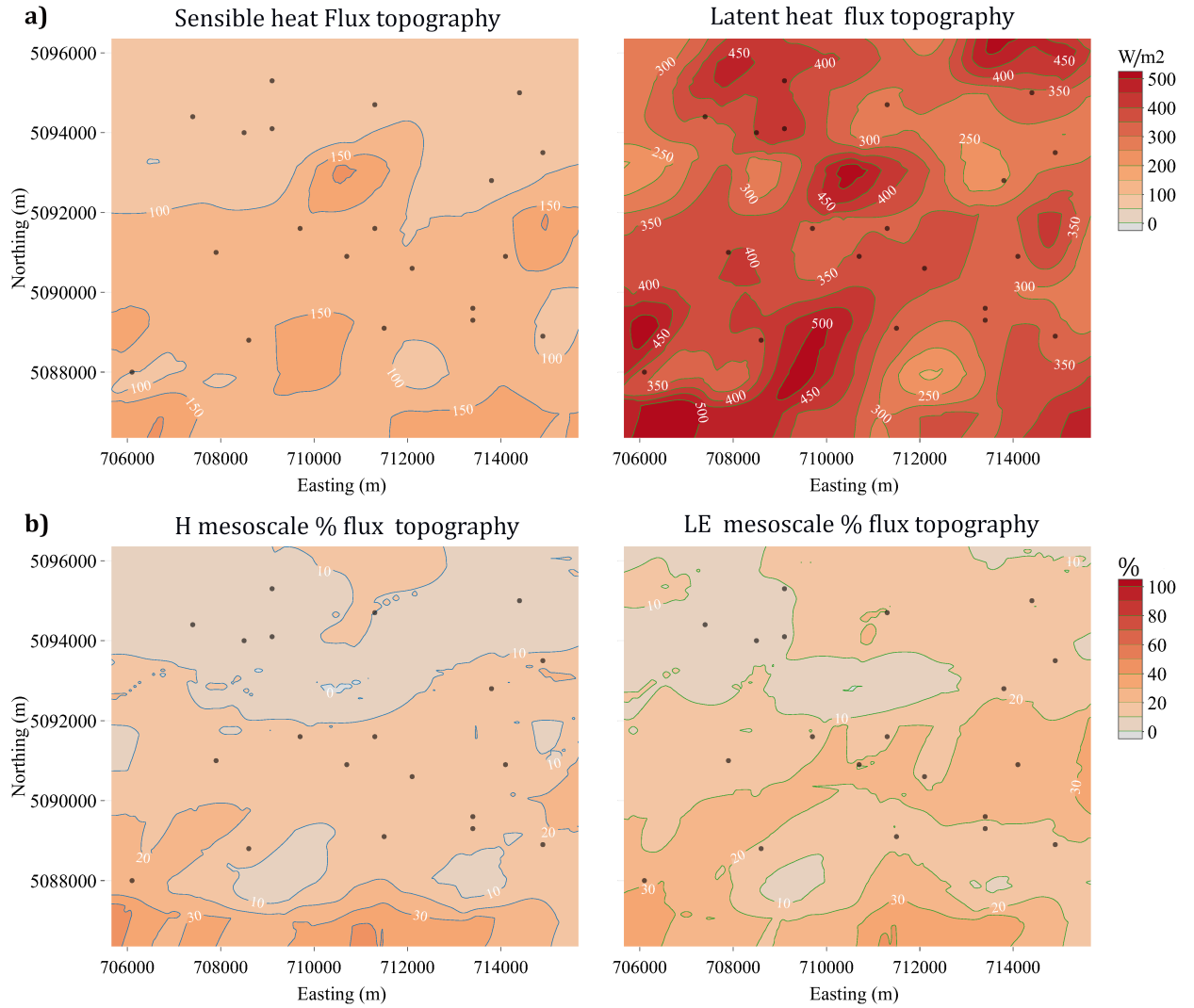


Figure 17: Flux topographies for RF 03 in the July IOP, 11 July 09:20 to 11:20 CDT over the 10×10 km CHEESEHEAD19 core domain. The brown dots are the NCAR-ISFS tower locations. The top row (a) shows the sensible (left) and latent (right) heat flux topographies. The percentage mesoscale contributions to the fluxes are shown in the bottom row (b) below their flux topographies.

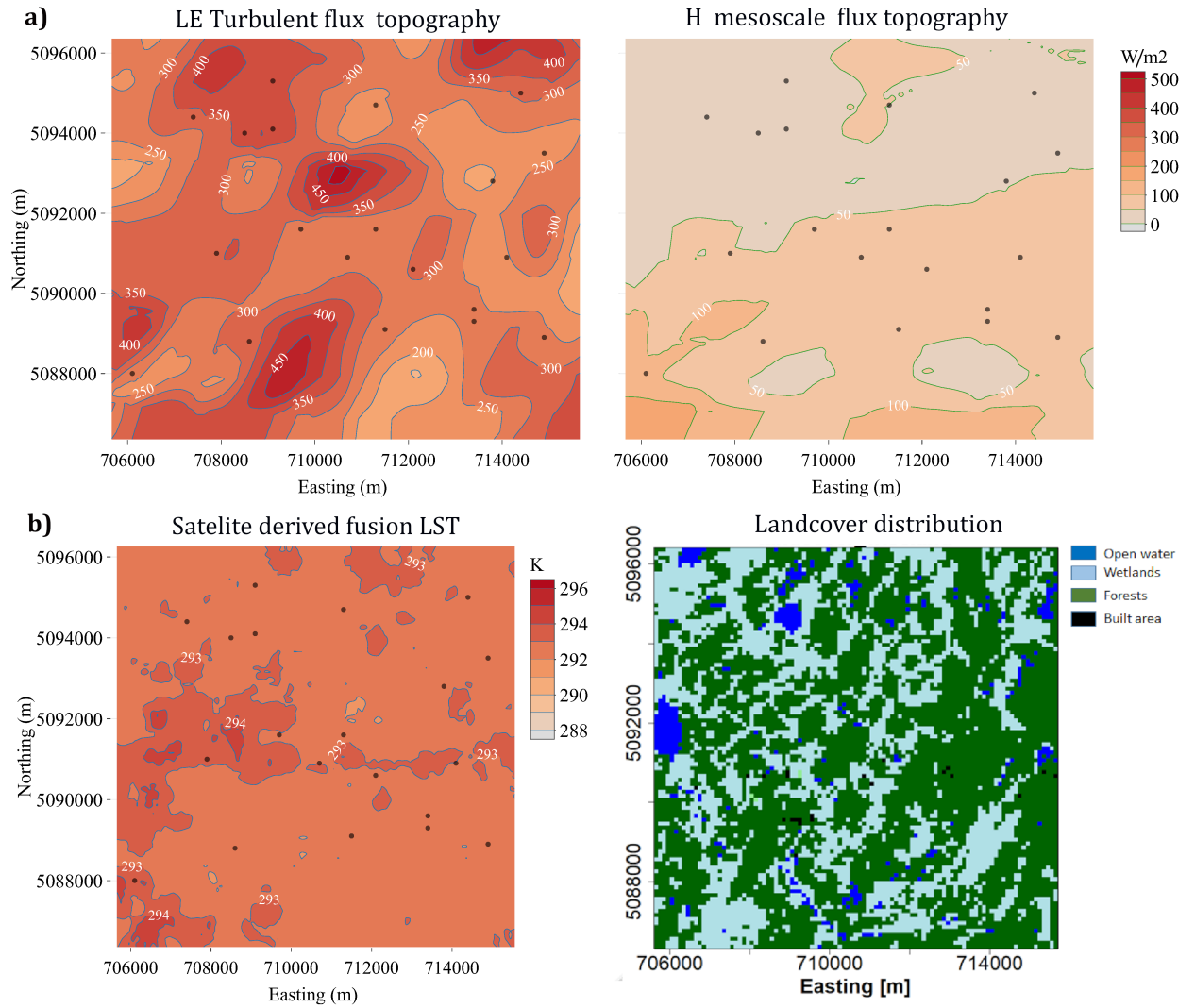


Figure 18: (a) scale-resolved, turbulent (left) and mesoscale (right) topographies for the latent heat flux and (b) distribution of land-surface properties LST (left, from Desai et al. (2021)) and land-surface classes (right, from Wiscland 2.0) across the domain.

726 4 Discussion

727 Implications for Surface-Atmospheric Transport and Surface Energy Budget 728 closure

729 Airborne measurements sampled across the heterogeneous study domain could resolve
730 the constituent surface-atmospheric transport scales. The aircraft campaign experiment
731 design allowed us to measure the diel and seasonal shifts in surface energy balance and
732 investigate its impact on the scales of surface atmospheric transport. We observed higher
733 fractions of mesoscale transport for sensible and latent heat fluxes in convectively driven
734 ABLs as shown in the KDE plots (Figure 12 and Figure 13) in Section 3.3. Previous
735 observational studies have noted the inverse relationship between tower measured surface
736 energy balance imbalance and u^* (Stoy et al., 2013; Eder et al., 2015), indicating that strong
737 mechanical mixing in shear driven ABL leads to larger turbulent transport. Our findings also
738 indicate the same, that lower frequency transport seems to have a preference for convectively
739 driven boundary layers. The dependency of latent heat fluxes is more complicated than the
740 sensible heat flux transport.

741 Using data from the LITFASS 2003 field experiment in Germany Foken (2008) and
742 Foken et al. (2010) showed that area averaged surface flux measurements reduce the surface
743 energy budget residuals. This, combined with the observations that the residuals are worse
744 for sites with more heterogeneous surfaces, leads to his hypothesis that what has remained
745 unaccounted for in the budgets could be the transport due to quasi-stationary secondary
746 circulations tied to landscape heterogeneity. The synthesis study by Stoy et al. (2013) found
747 consistent energy balance non closures across the sites and more importantly, noted that non-
748 closure is linked to the degree of landscape heterogeneity, quantified using MODIS products
749 and GLOBEstat elevation data. Since then a growing body of research has suggested that
750 quasi-stationary low-frequency eddies in the ABL tied to land–surface heterogeneity can
751 play an important role in surface-atmospheric transport.

752 LES studies with homogeneous (S. T. Salesky et al., 2017; Li & Bou-Zeid, 2011) and
753 heterogeneous (Margairaz et al. (2020), idealised heterogeneities) surface forcings have ob-
754 served secondary circulations in the ABL transition from convective rolls to a cellular struc-
755 ture as the ABL becomes more convectively unstable. Margairaz et al. (2020) notes that for
756 their simulations, with imposed surface temperature heterogeneities in irregular rectangular
757 patches, the convective-cell structure adjusts to the imposed surface temperature variations.
758 The surface atmospheric transport associated with these circulations would be missed by
759 tower based measurements unless they are either swept across the spatially-stationary mea-
760 suring points by the mean wind or only if the point measurements happen to be in their
761 vicinity (Mahrt, 2010; Charuchittipan et al., 2014). These studies along with observations
762 of better closure with longer averaging times and spatial measurements have led to a lead-
763 ing hypothesis that the surface energy balance closure problem is in fact a problem of scale
764 (Foken, 2008; Foken et al., 2010; Mauder et al., 2020)

765 Large scale organisations in the form of longitudinal roll vortices, aligned with the mean
766 wind can be generated in daytime convective boundary layers (Etling & Brown, 1993) while
767 stationary circulations can also be induced by horizontal variations in surface roughness
768 and heat flux (Desjardins et al., 1997; Sun et al., 1998). LES studies have shown that
769 over homogeneous surfaces, strongly unstable conditions can lead to the formation of stand-
770 ing convective cells akin to those that form in Rayleigh-Benard convection (Kanda et al.,
771 2004; De Roo & Mauder, 2018). Over heterogeneous surfaces these free convective cells
772 tend to become quasi-stationary secondary circulations, tied to the surface temperature,
773 roughness or vegetation gradients (Inagaki et al., 2006; Maronga & Raasch, 2013). Such
774 secondary circulation cells can lead to a persistent local-mean advective transport, leading
775 to an underestimation of surface energy exchange (Morrison et al., 2021)

776 Desai et al. (2021) presents a 50 m resolution fusion LST product for the same study
 777 domain, derived using a fusion of land–surface model and satellite products. They note that
 778 the spatial standard deviation of the fusion product increases towards autumn and is also
 779 high for summer afternoons, with higher LST spatial gradients. This could be playing a role
 780 in the higher sensible heat mesoscale fluxes observed in the late morning and afternoon for
 781 the July and August IOPs (Figures 9.a and 9.b)

782 In this regard, using wavelet methods on high-frequency airborne data has allowed us to
 783 retain the larger scale surface-atmosphere transport across the heterogeneous study domain
 784 and account for relevant transport scales. Figure 19 shows an IOP averaged representation
 785 of the scale resolved fluxes presented in Figures 5, 6, and 7. We do not see a prominent
 786 separation of scales between the turbulent and mesoscale regimes as was reported in the
 787 similar study of Mauder, Desjardins, and MacPherson (2007). There is a secondary peak in
 788 the LE cospectra for the July IOP around 1200m, which persisted across multiple research
 789 flights throughout the day (Figures 5.a and 5.c). Nonetheless, the flux cospectra show
 790 consistent and substantial contributions from the mesoscales > 2 km. Cospectra calculated
 791 for the July and August IOPs show higher values in the larger scales compared to the
 792 September IOP cospectrum for both H and LE. The H copsectra for July and August IOPs
 793 also show a flattening for scales greater than 5 km. An increase in the magnitude and
 794 range of turbulent scales is also seen between the August and September H copsectra. For
 795 the LE July and August IOP cospectra, the mesoscale contributions are around the same
 796 magnitude. The IOP averaged cospectra for LE also suggest that even with 30 km flight legs
 797 we might still be missing contributions from larger scales, with the cospectra tails ending
 798 around 150 to 200 Wm^{-2} .

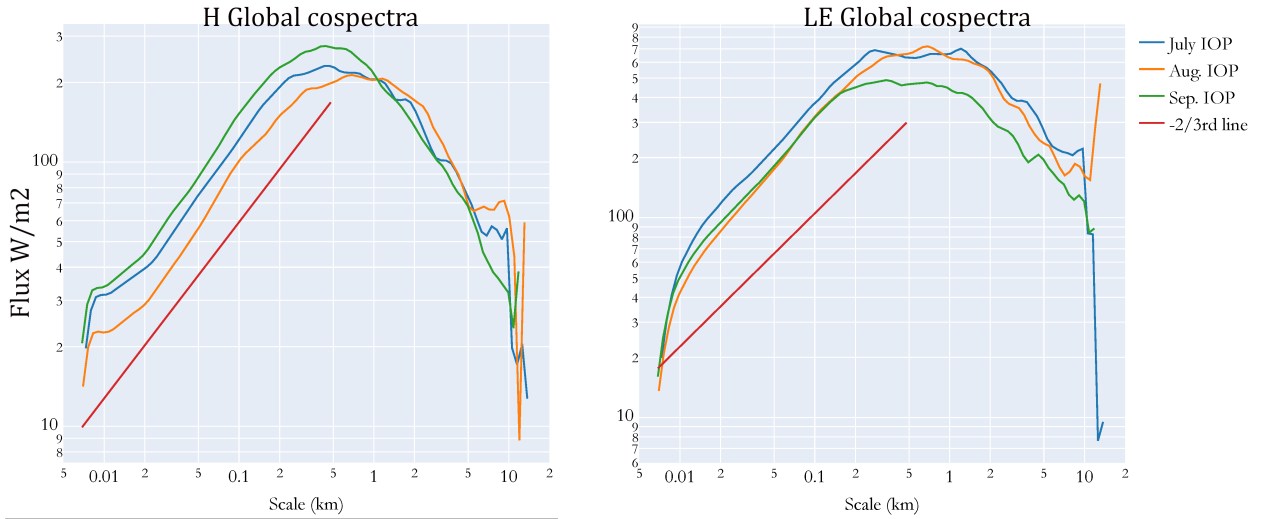


Figure 19: Global cospectra for H and LE for the 3 IOPs. Presented here are the ensemble averages of the wavelet cospectra presented in Figures 5 and 6.

799 Looking at the scale-averaged picture, we see that the mesoscale contributions are not
 800 a fixed fraction of the total or turbulent fluxes but vary throughout the day and as the
 801 landscape undergoes seasonal transitions (Figure 8 and Figure 9). The scale-separated
 802 sensible and latent heat fluxes do not behave similarly either. During the August IOP,
 803 (08/20 to 08/23), the measured Bowen ratio is the lowest at 0.3 and this IOP has the lowest
 804 mesoscale fraction for latent heat fluxes. Similarly, during the September IOP in early
 805 autumn (09/24 to 09/28) , the Bowen ratio is the highest at 1.3 and mesoscale sensible
 806 heat flux fraction was the lowest during this IOP. The total mesoscale flux percentages for

807 July IOP = 29%, August IOP = 20% and September IOP = 21%. The total percentages
 808 are closer in magnitude because of the seasonal sensible and latent heat flux balance. It is
 809 interesting to note that the August and September IOPs with very different Bowen ratios
 810 have the same mesoscale flux percentages.

811 The scale analysis of surface-atmospheric transport can provide valuable input for pro-
 812 cess based parametric correction methods for the tower-measured surface energy imbalance.
 813 Wanner et al. (2022) presents a parametric non-local correction factor for surface energy
 814 imbalance extending De Roo et al. (2018) work by incorporating the effects of idealised het-
 815 erogeneities using data from the LES work by (Margairaz et al., 2020). Mauder et al. (2021)
 816 (De Roo & Mauder, 2018) method for three midlatitude flux tower sites and found satisfac-
 817 tory results. Currently work is underway to extend the Wanner et al. (2022) method for
 818 the CHEESEHEAD19 flux towers and our results on the magnitudes and diel and seasonal
 819 variations of mesoscale fluxes can provide valuable order of magnitude benchmarks while
 820 correcting for the bias in eddy-covariance measurements due to the presence of large-scale
 821 dispersive fluxes.

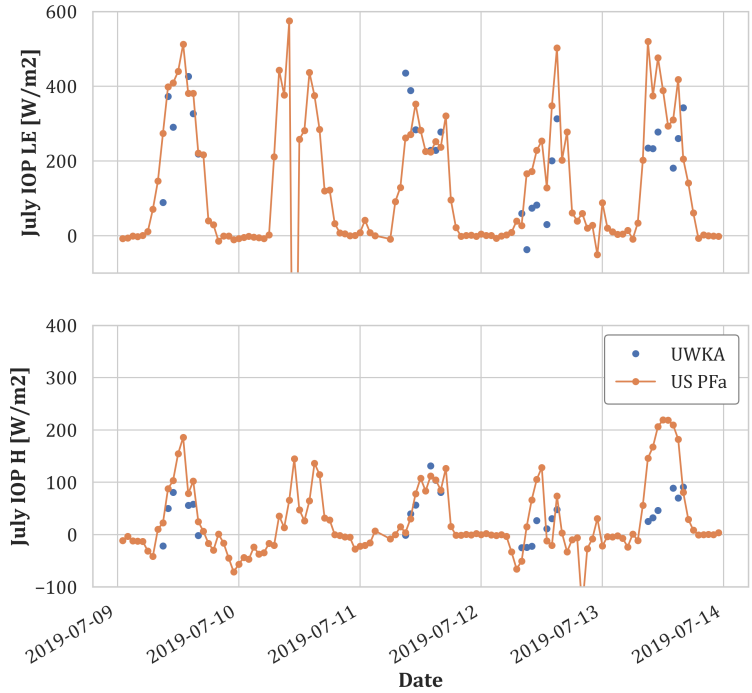


Figure 20: Hourly flux measurements from the UWKA flights and the 122 m tower measurements from the Ameriflux regional tall tower, US Pfa, at the center of the study domain. Data shown for the July IOP. The UWKA flux space series was averaged to hourly data points to match the hourly time resolution of the tower measurements.

822 We did a comparative study of the aircraft fluxes with flux measurements at 122 m
 823 height from the Ameriflux tall tower at the center of the study domain (US Pfa). The tall
 824 tower did not have reliable flux data at 122 m height during the August and September
 825 IOPs but the comparisons for the July IOP is presented in Figure 20. US Pfa makes hourly

826 flux measurements and at 122 m measurement height has a much broader flux footprint
 827 than the CHEESEHEAD19 flux towers, with maximum measurement height at 32 m. Here,
 828 the wavelet analysis based airborne fluxes compare reasonably well with the tall tower flux
 829 measurements made over a 1 hour averaging window that could include landscape level
 830 fluxes.

831 We tried to extend this approach by comparing total (H+LE) footprint weighted flux
 832 measurements from the flux topographies to the total flux measured by the NCAR-ISFS
 833 towers in the domain. The flux topographies calculated present a direct and physics-based
 834 flux map over the domain for the research flights analysed, providing a scale-resolved spatial
 835 distribution of sensible and latent heat fluxes. They show persistent areas of large scale flux
 836 contributions within the study domain which could be linked to variations of land–surface
 837 properties. However, they are also inherently limited by the foot prints of airborne transects
 838 and can only be extrapolated within those flight transect footprints. Flux measurement in
 839 space from the topography was matched with the flux measurement from the tower located
 840 in the same 100×100 grid point in space and corresponding to the same time as the UWKA
 841 data sample. However, for all case studies conducted with six research flights over three
 842 days in the three IOPs (July 11, August 21 and September 24) the scatter plots between
 843 fluxes values from the topography grid and the tower measured values did not show any
 844 clear relationships. This could be because of the vertical flux divergences between the tower
 845 measurement heights and the 100m aircraft measurement height, random errors of tower
 846 and flux measurements compounding each other etc.

847 One should be careful while interpreting footprint weighted flux maps to study surface-
 848 atmospheric transport. The experimental design introduces a temporal element to the
 849 topographies calculated in this study. Even though spatially adjacent flight transects during
 850 a single flight are only about 6-8 minutes apart, a research flight across the domain takes
 851 about 2.5 hours, imprinting the diel pattern to a calculated flux topography. Kohnert et
 852 al. (2017) and Rey-Sanchez et al. (2022) present a flux map based approach to detecting
 853 methane hotspots from aircraft and tower measurements, respectively. Unlike methane
 854 fluxes, surface heat fluxes have a strong diurnal cycle. Hence, attributing sources for the
 855 fluxes solely based on aircraft measured flux topography maps and linking the horizontal flux
 856 gradients and surface gradients can be complicated. This presents impactful opportunities
 857 to parsimoniously combine aircraft and tower data, when available as is the case for the
 858 CHEESEHEAD19 experiment, to arrive at a space-time aligned view of surface fluxes. The
 859 airborne campaign numerical experiment design involved calculating space and time resolved
 860 flux maps across the domain from simulated tower and aircraft data (from candidate flight
 861 patterns) using a machine learning approach with the land–surface properties as drivers
 862 (Figure 12 in Metzger et al. (2021)).

863 5 Conclusions

864 We present a systematic regional-scale observational analysis over a heterogeneous
 865 domain that quantifies the multi-scale nature of sub-grid scaling and patterning. The
 866 CHEESEHEAD19 field experiment provided a unique dataset to diagnose and quantify
 867 the diel and seasonal contributions from large scale transport over the study domain as its
 868 surface energy balance shifts from a more latent heat flux-dominated late summer landscape
 869 to a more sensible heat flux-dominated early autumn landscape.

870 Using airborne measurements from this comprehensive field experiment dataset we
 871 sought to answer whether spatially resolved airborne eddy covariance can identify spatial
 872 scales of surface-atmosphere fluxes over heterogeneous surfaces? Applying wavelet analysis
 873 to the airborne flux measurements from the field experiment data allowed us to evaluate and
 874 spatially resolve the mesoscale contributions at 100 metres above ground over the heteroge-
 875 neous landscape. We looked at the diel and seasonal variability of the scale-resolved fluxes.
 876 The measured latent heat flux magnitudes had more pronounced seasonal changes than the

877 sensible heat fluxes. Meanwhile, the measured domain-averaged sensible heat flux values
 878 had a more pronounced diurnal cycle. We observed larger mesoscale transport for sensible
 879 heat fluxes in convectively driven ABLs across the three IOP scenarios, while for latent
 880 heat fluxes only the July and August IOPs showed more fractional mesoscale transport in
 881 convectively driven ABLs. For the September IOP, which had mostly shear driven ABL
 882 cases, we did not find any significant change between the fractional mesoscale transport in
 883 convectively and shear driven ABLs. We hypothesise that the larger scale transport mea-
 884 sured in our study could be linked to organized structures in the ABL as has been reported
 885 in previous numerical (Kanda et al., 2004; Inagaki et al., 2006; S. Salesky & Anderson, 2020;
 886 Margairaz et al., 2020) and observational (Eder et al., 2015; Morrison et al., 2021) studies.
 887 The flux topography case studies indicate that the mesoscale transport spatial variability
 888 would be missed by tower measurements in the domain. Areas of persistent contributions
 889 in the domain could be linked to the presence of co-located forested wetlands, creating
 890 roughness and thermal surface heterogeneities.

891 From our observations and analyses we reject our null hypothesis that the mesoscale
 892 transport is an invariant, small fixed fraction of total flux. We conclude that our alternate
 893 hypothesis, persistent contributions of larger scale (meso- β to meso- γ) fluxes to the daytime
 894 sensible and latent heat fluxes exist with diurnal and seasonal variations, holds. We report
 895 substantial dissimilarities between the sensible and latent heat flux transport suggesting
 896 different physical mechanisms under play, warranting further investigations. The analysis
 897 helps further our understanding of the interactions between surface spatial heterogeneity
 898 and lower atmosphere feed-backs. Measurements of flux contributions over heterogeneous
 899 landscapes have not been studied well. In particular the shifts associated with seasonal,
 900 landscape level transitions as is covered in this study. We believe that this study, by high-
 901 lighting the importance of larger-scale sub-grid transport, adds a critical piece of information
 902 in assimilating and integrating observations and model outputs at multiple scales.

903 6 Open Research

904 All of the CHEESEHEAD19 observations including UWKA airborne measurements are
 905 archived at the NCAR EOL repository at [https://www.eol.ucar.edu/field_projects/](https://www.eol.ucar.edu/field_projects/cheesehead)
 906 [cheesehead](https://www.eol.ucar.edu/field_projects/cheesehead).

907 The eddy4R v.0.2.0 software framework used to generate eddy-covariance flux esti-
 908 mates can be freely accessed at <https://github.com/NEONScience/eddy4R>. The eddy4R
 909 turbulence v0.0.16 and Environmental Response Functions v0.0.5 software modules for ad-
 910 vanced airborne data processing were accessed under Terms of Use for this study ([https://](https://www.eol.ucar.edu/content/cheesehead-code-policy-appendix)
 911 www.eol.ucar.edu/content/cheesehead-code-policy-appendix) and are available upon
 912 request. The current version of the production code is hosted following a development and
 913 systems operation (DevOps) framework for collaborative software development. The De-
 914 vOps framework allows for a portable, reproducible and extensible EC processing software
 915 capabilities that are modular and version controlled using GitHub. The code base is main-
 916 tained as Docker images to preserve the same dependencies and ensure reproducibility and
 917 portability across platforms.

918 Pre-processed input data for the Eddy4R flux processing routines and the calculated
 919 scale-resolved fluxes are available at the Ecometeorology lab UW server at [http://co2.aos](http://co2.aos.wisc.edu/data/CHEESEHEAD-incoming/uwka_waveletfluxes/)
 920 [.wisc.edu/data/CHEESEHEAD-incoming/uwka_waveletfluxes/](http://co2.aos.wisc.edu/data/CHEESEHEAD-incoming/uwka_waveletfluxes/). The python code used to
 921 create figures for the manuscript is available at [https://github.com/sreenathpaleri/](https://github.com/sreenathpaleri/CHEESEHEAD/blob/analysis/scripts/UWKA/manuscript/plot_MS.py)
 922 [CHEESEHEAD/blob/analysis/scripts/UWKA/manuscript/plot_MS.py](https://github.com/sreenathpaleri/CHEESEHEAD/blob/analysis/scripts/UWKA/manuscript/plot_MS.py)

923 Acknowledgments

924 This material is based in part upon work supported by the National Science Foundation
 925 through the CHEESEHEAD19 project (grant no. AGS-1822420) and the NEON Program

(grant no. DBI-0752017). The National Ecological Observatory Network is a program sponsored by the National Science Foundation and operated under cooperative agreement by Battelle. Brian Butterworth was additionally supported by the NOAA Physical Sciences Laboratory. Katrin Kohnert and Andrei Serafimovich were supported by the Helmholtz Association of German Research Centres through a Helmholtz Young Investigators Group grant (grant VH-NG-821) and by the European Union’s Horizon 2020 research and innovation program under grant agreement No 72789. We also recognize that our field research occurs on the traditional territories of the Ojibwe people, which have been unjustly ceded and whose ancestors were the original scientists and naturalists who stewarded the land, air, and waters we are fortunate to observe, reflect, and hopefully help continue to flourish.

References

- Addison, P. S. (2017). *The illustrated wavelet transform handbook: introductory theory and applications in science, engineering, medicine and finance*. CRC press.
- Adler, B., Bianco, L., Duncan, J., Turner, D., & Wilczak, J. (2021). *NOAA microwave radiometer data and thermodynamic profile retrievals. version 3.0*. UCAR/NCAR - Earth Observing Laboratory. Retrieved 2022-10-02, from <https://data.eol.ucar.edu/dataset/592.017> ([Dataset] Artwork Size: 6 data files, 2 ancillary/documentation files, 15 GiB Medium: ZIP: PKZIP (application/zip) Pages: 6 data files, 2 ancillary/documentation files, 15 GiB Version Number: 3.0 Type: dataset) doi: 10.26023/Y0W2-8BAG-6Y0A
- Amiro, B. (1998, April). Footprint climatologies for evapotranspiration in a boreal catchment. *Agricultural and Forest Meteorology*, *90*(3), 195–201. Retrieved 2022-04-12, from <https://linkinghub.elsevier.com/retrieve/pii/S0168192397000968> doi: 10.1016/S0168-1923(97)00096-8
- Aubinet, M., Grelle, A., Ibrom, A., Rannik, Ü., Moncrieff, J., Foken, T., ... Vesala, T. (1999). Estimates of the Annual Net Carbon and Water Exchange of Forests: The EUROFLUX Methodology. In *Advances in Ecological Research* (Vol. 30, pp. 113–175). Elsevier. Retrieved 2020-10-13, from <https://linkinghub.elsevier.com/retrieve/pii/S0065250408600185> doi: 10.1016/S0065-2504(08)60018-5
- Aubinet, M., Vesala, T., & Papale, D. (Eds.). (2012). *Eddy Covariance: A Practical Guide to Measurement and Data Analysis*. Dordrecht: Springer Netherlands. Retrieved 2020-10-13, from <http://link.springer.com/10.1007/978-94-007-2351-1> doi: 10.1007/978-94-007-2351-1
- Avissar, R., & Schmidt, T. (1998). An Evaluation of the Scale at which Ground-Surface Heat Flux Patchiness Affects the Convective Boundary Layer Using Large-Eddy Simulations. *JOURNAL OF THE ATMOSPHERIC SCIENCES*, *55*, 24.
- Baldocchi, D., Falge, E., Gu, L., Olson, R., Hollinger, D., Running, S., ... Wofsy, S. (2001, November). FLUXNET: A New Tool to Study the Temporal and Spatial Variability of Ecosystem-Scale Carbon Dioxide, Water Vapor, and Energy Flux Densities. *Bulletin of the American Meteorological Society*, *82*(11), 2415 – 2434. Retrieved from https://journals.ametsoc.org/view/journals/bams/82/11/1520-0477_2001_082_2415_fantts_2.3_co_2.xml (Place: Boston MA, USA Publisher: American Meteorological Society) doi: 10.1175/1520-0477(2001)082<2415:FANTTS>2.3.CO;2
- Bange, J., Beyrich, F., & Engelbart, D. A. M. (2002, December). Airborne measurements of turbulent fluxes during LITFASS-98: Comparison with ground measurements and remote sensing in a case study. *Theoretical and Applied Climatology*, *73*(1-2), 35–51. Retrieved 2021-03-01, from <http://link.springer.com/10.1007/s00704-002-0692-6> doi: 10.1007/s00704-002-0692-6
- Bange, J., Spieß, T., Herold, M., Beyrich, F., & Hennemuth, B. (2006, October). Turbulent fluxes from Helipod flights above quasi-homogeneous patches within the LITFASS area. *Boundary-Layer Meteorology*, *121*(1), 127–151. Retrieved 2021-01-01, from <http://link.springer.com/10.1007/s10546-006-9106-0> doi: 10.1007/s10546-006

- 979 -9106-0
- 980 Berger, B. W., Davis, K. J., Yi, C., Bakwin, P. S., & Zhao, C. L. (2001, April). Long-Term
981 Carbon Dioxide Fluxes from a Very Tall Tower in a Northern Forest: Flux Measure-
982 ment Methodology. *Journal of Atmospheric and Oceanic Technology*, *18*(4), 529–
983 542. Retrieved 2022-05-12, from [http://journals.ametsoc.org/doi/10.1175/1520-0426\(2001\)018<0529:LTCDFD>2.0.CO;2](http://journals.ametsoc.org/doi/10.1175/1520-0426(2001)018<0529:LTCDFD>2.0.CO;2) doi: 10.1175/1520-0426(2001)018<0529:LTCDFD>2.0.CO;2
- 984
985
- 986 Bernhofer, C. (1992). Applying a simple three-dimensional eddy correlation system for
987 latent and sensible heat flux to contrasting forest canopies. *Theoretical and Applied*
988 *Climatology*, *46*(2-3), 163–172. Retrieved 2020-12-15, from <http://link.springer.com/10.1007/BF00866096> doi: 10.1007/BF00866096
- 989
- 990 Bou-Zeid, E., Anderson, W., Katul, G. G., & Mahrt, L. (2020, July). The Persistent
991 Challenge of Surface Heterogeneity in Boundary-Layer Meteorology: A Review.
992 *Boundary-Layer Meteorology*. Retrieved 2020-09-30, from <http://link.springer.com/10.1007/s10546-020-00551-8> doi: 10.1007/s10546-020-00551-8
- 993
- 994 Businger, J. A., Wyngaard, J. C., Izumi, Y., & Bradley, E. F. (1971). Flux-profile relation-
995 ships in the atmospheric surface layer. *Journal of Atmospheric Sciences*, *28*(2), 181
996 - 189. Retrieved from https://journals.ametsoc.org/view/journals/atmsc/28/2/1520-0469_1971_028_0181_fprita_2_0_co_2.xml doi: 10.1175/1520-0469(1971)028<0181:FPRITA>2.0.CO;2
- 997
998
- 999 Butterworth, B. J., Desai, A. R., Townsend, P. A., Petty, G. W., Andresen, C. G., Bertram,
1000 T. H., ... Wilczak, J. M. (2021). Connecting Land–Atmosphere Interactions to Sur-
1001 face Heterogeneity in CHEESEHEAD19. *Bulletin of the American Meteorological So-*
1002 *ciety*, *102*(2), E421 – E445. Retrieved from <https://journals.ametsoc.org/view/journals/bams/102/2/BAMS-D-19-0346.1.xml> (Place: Boston MA, USA Publisher:
1003 American Meteorological Society) doi: 10.1175/BAMS-D-19-0346.1
- 1004
- 1005 Cattaneo, M. D., Crump, R. K., Farrell, M. H., & Feng, Y. (2019). Binscatter regressions.
1006 *arXiv preprint arXiv:1902.09615*. ([Software])
- 1007
- 1008 Charuchittipan, D., Babel, W., Mauder, M., Leps, J.-P., & Foken, T. (2014, September).
1009 Extension of the Averaging Time in Eddy-Covariance Measurements and Its Effect on
1010 the Energy Balance Closure. *Boundary-Layer Meteorology*, *152*(3), 303–327. Retrieved
1011 2020-10-13, from <http://link.springer.com/10.1007/s10546-014-9922-6> doi:
10.1007/s10546-014-9922-6
- 1012
- 1013 Chetty, R., Looney, A., & Kroft, K. (2009). Salience and taxation: Theory and evidence.
American economic review, *99*(4), 1145–77.
- 1014
- 1015 Chetty, R., & Szeidl, A. (2005). Marriage, housing, and portfolio choice: A test of grossman-
laroque. *Mimeo graph, UC-Berkeley*.
- 1016
- 1017 Davis, K. J., Bakwin, P. S., Yi, C., Berger, B. W., Zhao, C., Teclaw,
R. M., & Isebrands, J. G. (2003). The annual cycles of CO₂ and
1018 H₂O exchange over a northern mixed forest as observed from a very
1019 tall tower. *Global Change Biology*, *9*(9), 1278–1293. Retrieved 2022-03-
1020 28, from <http://onlinelibrary.wiley.com/doi/abs/10.1046/j.1365-2486.2003.00672.x>
1021 (.eprint: <https://onlinelibrary.wiley.com/doi/pdf/10.1046/j.1365-2486.2003.00672.x>) doi: 10.1046/j.1365-2486.2003.00672.x
- 1022
- 1023 De Roo, F., & Mauder, M. (2018, April). The influence of idealized surface heterogeneity
1024 on virtual turbulent flux measurements. *Atmospheric Chemistry and Physics*, *18*(7),
1025 5059–5074. Retrieved 2020-11-17, from <https://acp.copernicus.org/articles/18/5059/2018/> doi: 10.5194/acp-18-5059-2018
- 1026
- 1027 De Roo, F., Zhang, S., Huq, S., & Mauder, M. (2018, December). A semi-empirical model
1028 of the energy balance closure in the surface layer. *PLOS ONE*, *13*(12), e0209022.
1029 Retrieved 2019-12-23, from <http://dx.plos.org/10.1371/journal.pone.0209022>
1030 doi: 10.1371/journal.pone.0209022
- 1031
- 1032 Desai, A. R. (2014, February). Influence and predictive capacity of climate anomalies
1033 on daily to decadal extremes in canopy photosynthesis. *Photosynthesis Research*,
119(1-2), 31–47. Retrieved 2022-03-28, from <http://link.springer.com/10.1007/>

- 1034 s11120-013-9925-z doi: 10.1007/s11120-013-9925-z
- 1035 Desai, A. R., Khan, A. M., Zheng, T., Paleri, S., Butterworth, B., Lee, T. R., ... Metzger,
1036 S. (2021, October). Multi-Sensor Approach for High Space and Time Resolution
1037 Land Surface Temperature. *Earth and Space Science*, 8(10). Retrieved 2022-01-
1038 24, from <https://onlinelibrary.wiley.com/doi/10.1029/2021EA001842> doi: 10
1039 .1029/2021EA001842
- 1040 Desai, A. R., Xu, K., Tian, H., Weishampel, P., Thom, J., Baumann, D., ... Kolka, R.
1041 (2015, February). Landscape-level terrestrial methane flux observed from a very tall
1042 tower. *Agricultural and Forest Meteorology*, 201, 61–75. Retrieved 2022-03-28, from
1043 <https://linkinghub.elsevier.com/retrieve/pii/S0168192314002688> doi: 10
1044 .1016/j.agrformet.2014.10.017
- 1045 Desjardins, R. L., MacPherson, J. I., Mahrt, L., Schuepp, P., Pattey, E., Neumann, H.,
1046 ... Joiner, D. W. (1997, December). Scaling up flux measurements for the bo-
1047 real forest using aircraft-tower combinations. *Journal of Geophysical Research: At-
1048 mospheres*, 102(D24), 29125–29133. Retrieved 2021-01-01, from [http://doi.wiley
1049 .com/10.1029/97JD00278](http://doi.wiley.com/10.1029/97JD00278) doi: 10.1029/97JD00278
- 1050 Drobinski, P., Brown, R. a., Flamant, P. H., & Pelon, J. (1998, September). Evidence of Or-
1051 ganized Large Eddies by Ground-Based Doppler Lidar, Sonic Anemometer and Sodar.
1052 *Boundary-Layer Meteorology*, 88(3), 343–361. Retrieved 2022-03-09, from [http://
1053 link.springer.com/10.1023/A:1001167212584](http://link.springer.com/10.1023/A:1001167212584) doi: 10.1023/A:1001167212584
- 1054 Duncan Jr, J. B., Bianco, L., Adler, B., Bell, T., Djalalova, I. V., Riihimaki, L., ... others
1055 (2022). Evaluating convective planetary boundary layer height estimations resolved
1056 by both active and passive remote sensing instruments during the cheesehead19 field
1057 campaign. *Atmospheric Measurement Techniques*, 15(8), 2479–2502.
- 1058 Eder, F., Schmidt, M., Damian, T., Träumner, K., & Mauder, M. (2015, January).
1059 Mesoscale Eddies Affect Near-Surface Turbulent Exchange: Evidence from Lidar
1060 and Tower Measurements. *Journal of Applied Meteorology and Climatology*, 54(1),
1061 189–206. Retrieved 2019-07-26, from [http://journals.ametsoc.org/doi/10.1175/
1062 JAMC-D-14-0140.1](http://journals.ametsoc.org/doi/10.1175/JAMC-D-14-0140.1) doi: 10.1175/JAMC-D-14-0140.1
- 1063 Engelmann, C., & Bernhofer, C. (2016, October). Exploring Eddy-Covariance Measure-
1064 ments Using a Spatial Approach: The Eddy Matrix. *Boundary-Layer Meteorology*,
1065 161(1), 1–17. Retrieved 2022-03-09, from [http://link.springer.com/10.1007/
1066 s10546-016-0161-x](http://link.springer.com/10.1007/s10546-016-0161-x) doi: 10.1007/s10546-016-0161-x
- 1067 Etling, D., & Brown, R. A. (1993, August). Roll vortices in the planetary boundary layer:
1068 A review. *Boundary-Layer Meteorology*, 65(3), 215–248. Retrieved 2019-06-26, from
1069 <http://link.springer.com/10.1007/BF00705527> doi: 10.1007/BF00705527
- 1070 Farge, M. (1992). WAVELET TRANSFORMS AND THEIR APPLICATIONS TO TUR-
1071 BULENCE. , 64.
- 1072 Finnigan, J. J., Clement, R., Malhi, Y., Leuning, R., & Cleugh, H. (2003, April). A
1073 Re-Evaluation of Long-Term Flux Measurement Techniques Part I: Averaging and
1074 Coordinate Rotation. *Boundary-Layer Meteorology*, 107(1), 1–48. Retrieved 2020-12-
1075 10, from <http://link.springer.com/10.1023/A:1021554900225> doi: 10.1023/A:
1076 1021554900225
- 1077 Foken, T. (2008, September). THE ENERGY BALANCE CLOSURE PROBLEM: AN
1078 OVERVIEW. *Ecological Applications*, 18(6), 1351–1367. Retrieved 2020-10-12, from
1079 <http://doi.wiley.com/10.1890/06-0922.1> doi: 10.1890/06-0922.1
- 1080 Foken, T. (2017). *Micrometeorology*. Berlin, Heidelberg: Springer Berlin Heidelberg. Re-
1081 trieved 2020-10-13, from <http://link.springer.com/10.1007/978-3-642-25440-6>
1082 doi: 10.1007/978-3-642-25440-6
- 1083 Foken, T., Mauder, M., Liebethal, C., Wimmer, F., Beyrich, F., Leps, J.-P., ... Bange, J.
1084 (2010, July). Energy balance closure for the LITFASS-2003 experiment. *Theoretical
1085 and Applied Climatology*, 101(1-2), 149–160. Retrieved 2020-10-12, from [http://
1086 link.springer.com/10.1007/s00704-009-0216-8](http://link.springer.com/10.1007/s00704-009-0216-8) doi: 10.1007/s00704-009-0216-8
- 1087 Foken, T., Wimmer, F., Mauder, M., Thomas, C., & Liebethal, C. (2006). Some aspects of
1088 the energy balance closure problem. *Atmos. Chem. Phys.*, 8.

- 1089 French, J., Oolman, L., & Plummer, D. (2021). *University of Wyoming King Air (UWKA)*
 1090 *High Rate Flight Level Data. Version 1.0*. UCAR/NCAR - Earth Observing Labo-
 1091 ratory. Retrieved 2022-03-30, from <https://data.eol.ucar.edu/dataset/592.146>
 1092 ([Dataset] Artwork Size: 24 data files, 2 ancillary/documentation files, 3 GiB Medium:
 1093 NetCDF: Network Common Data Form (application/x-netcdf) Pages: 24 data files,
 1094 2 ancillary/documentation files, 3 GiB Version Number: 1.0 Type: dataset) doi:
 1095 10.26023/5B70-4VP5-XY0V
- 1096 Gao, Z., Liu, H., Chen, X., Huang, M., Missik, J. E. C., Yao, J., ... Mcfarland, D. P. (2020,
 1097 July). Enlarged Nonclosure of Surface Energy Balance With Increasing Atmospheric
 1098 Instabilities Linked to Changes in Coherent Structures. *Journal of Geophysical Re-*
 1099 *search: Atmospheres*, 125(14). Retrieved 2020-12-12, from [https://onlinelibrary](https://onlinelibrary.wiley.com/doi/abs/10.1029/2020JD032889)
 1100 [.wiley.com/doi/abs/10.1029/2020JD032889](https://onlinelibrary.wiley.com/doi/abs/10.1029/2020JD032889) doi: 10.1029/2020JD032889
- 1101 Gatz, D. F., & Smith, L. (1995, June). The standard error of a weighted mean concentra-
 1102 tion—I. Bootstrapping vs other methods. *Atmospheric Environment*, 29(11), 1185–
 1103 1193. Retrieved 2021-01-10, from [https://linkinghub.elsevier.com/retrieve/](https://linkinghub.elsevier.com/retrieve/pii/135223109400210C)
 1104 [pii/135223109400210C](https://linkinghub.elsevier.com/retrieve/pii/135223109400210C) doi: 10.1016/1352-2310(94)00210-C
- 1105 Haimov, S., & Rodi, A. (2013, October). Fixed-Antenna Pointing-Angle Calibration of
 1106 Airborne Doppler Cloud Radar. *Journal of Atmospheric and Oceanic Technology*,
 1107 30(10), 2320–2335. Retrieved 2022-05-12, from [http://journals.ametsoc.org/doi/](http://journals.ametsoc.org/doi/10.1175/JTECH-D-12-00262.1)
 1108 [10.1175/JTECH-D-12-00262.1](http://journals.ametsoc.org/doi/10.1175/JTECH-D-12-00262.1) doi: 10.1175/JTECH-D-12-00262.1
- 1109 Hartmann, J., Gehrman, M., Kohnert, K., Metzger, S., & Sachs, T. (2018). New calibra-
 1110 tion procedures for airborne turbulence measurements and accuracy of the methane
 1111 fluxes during the AirMeth campaigns. , 11(7), 4567–4581. Retrieved 2022-09-22, from
 1112 <https://amt.copernicus.org/articles/11/4567/2018/> (Publisher: Copernicus
 1113 GmbH) doi: 10.5194/amt-11-4567-2018
- 1114 Higgins, C. W., Pardyjak, E., Froidevaux, M., Simeonov, V., & Parlange, M. B. (2013,
 1115 December). Measured and Estimated Water Vapor Advection in the Atmospheric
 1116 Surface Layer. *Journal of Hydrometeorology*, 14(6), 1966–1972. Retrieved 2022-03-
 1117 09, from <http://journals.ametsoc.org/doi/10.1175/JHM-D-12-0166.1> doi: 10
 1118 .1175/JHM-D-12-0166.1
- 1119 Högström, U. (1988). Non-dimensional wind and temperature profiles in the atmospheric
 1120 surface layer: A re-evaluation. , 42(1), 55–78. Retrieved 2022-09-23, from [https://](https://doi.org/10.1007/BF00119875)
 1121 doi.org/10.1007/BF00119875 doi: 10.1007/BF00119875
- 1122 Iglewicz, B., & Hoaglin, D. C. (1993). *How to detect and handle outliers* (Vol. 16). Asq
 1123 Press.
- 1124 Inagaki, A., Letzel, M. O., Raasch, S., & Kanda, M. (2006). Impact of Surface Heterogeneity
 1125 on Energy Imbalance: A Study Using LES. *Journal of the Meteorological Society of*
 1126 *Japan*, 84(1), 187–198. Retrieved 2019-07-25, from [http://joi.jlsc.jst.go.jp/](http://joi.jlsc.jst.go.jp/JST.JSTAGE/jmsj/84.187?from=CrossRef)
 1127 [JST.JSTAGE/jmsj/84.187?from=CrossRef](http://joi.jlsc.jst.go.jp/JST.JSTAGE/jmsj/84.187?from=CrossRef) doi: 10.2151/jmsj.84.187
- 1128 Kaimal, J. C., & Finnigan, J. J. (1994). *Atmospheric boundary layer flows: their structure*
 1129 *and measurement*. New York: Oxford University Press.
- 1130 Kanda, M., Inagaki, A., Letzel, M. O., Raasch, S., & Watanabe, T. (2004, March). LES
 1131 Study of the Energy Imbalance Problem with Eddy Covariance Fluxes. *Boundary-*
 1132 *Layer Meteorology*, 110(3), 381–404. Retrieved 2019-06-26, from [http://link](http://link.springer.com/10.1023/B:BOUN.0000007225.45548.7a)
 1133 [.springer.com/10.1023/B:BOUN.0000007225.45548.7a](http://link.springer.com/10.1023/B:BOUN.0000007225.45548.7a) doi: 10.1023/B:BOUN
 1134 .0000007225.45548.7a
- 1135 Kljun, N., Calanca, P., Rotach, M. W., & Schmid, H. P. (2004, September). A Sim-
 1136 ple Parameterisation for Flux Footprint Predictions. *Boundary-Layer Meteorology*,
 1137 112(3), 503–523. Retrieved 2021-01-01, from [http://link.springer.com/10.1023/](http://link.springer.com/10.1023/B:BOUN.0000030653.71031.96)
 1138 [B:BOUN.0000030653.71031.96](http://link.springer.com/10.1023/B:BOUN.0000030653.71031.96) doi: 10.1023/B:BOUN.0000030653.71031.96
- 1139 Kljun, N., Rotach, M., & Schmid, H. (2002, May). A Three-Dimensional Backward
 1140 Lagrangian Footprint Model For A Wide Range Of Boundary-Layer Stratifications.
 1141 *Boundary-Layer Meteorology*, 103(2), 205–226. Retrieved 2021-01-01, from [http://](http://link.springer.com/10.1023/A:1014556300021)
 1142 link.springer.com/10.1023/A:1014556300021 doi: 10.1023/A:1014556300021
- 1143 Kohnert, K., Serafimovich, A., Metzger, S., Hartmann, J., & Sachs, T. (2017, December).

- 1144 Strong geologic methane emissions from discontinuous terrestrial permafrost in the
 1145 Mackenzie Delta, Canada. *Scientific Reports*, 7(1), 5828. Retrieved 2019-12-21, from
 1146 <http://www.nature.com/articles/s41598-017-05783-2> doi: 10.1038/s41598-017-
 1147 -05783-2
- 1148 Lenschow, D. H., Mann, J., & Kristensen, L. (1994, June). How Long
 1149 Is Long Enough When Measuring Fluxes and Other Turbulence Statistics?
 1150 *Journal of Atmospheric and Oceanic Technology*, 11(3), 661 – 673.
 1151 Retrieved from [https://journals.ametsoc.org/view/journals/atot/11/3/1520-
 1152 -0426_1994_011_0661_hlilew_2_0_co_2.xml](https://journals.ametsoc.org/view/journals/atot/11/3/1520-0426_1994_011_0661_hlilew_2_0_co_2.xml) (Place: Boston MA, USA Publisher:
 1153 American Meteorological Society) doi: 10.1175/1520-0426(1994)011<0661:HLILEW>2
 1154 .0.CO;2
- 1155 Lenschow, D. H., & Stankov, B. B. (1986, June). Length Scales in the Convective
 1156 Boundary Layer. *Journal of Atmospheric Sciences*, 43(12), 1198 – 1209.
 1157 Retrieved from [https://journals.ametsoc.org/view/journals/atsc/43/12/1520-
 1158 -0469_1986_043_1198_lsitcb_2_0_co_2.xml](https://journals.ametsoc.org/view/journals/atsc/43/12/1520-0469_1986_043_1198_lsitcb_2_0_co_2.xml) (Place: Boston MA, USA Publisher:
 1159 American Meteorological Society) doi: 10.1175/1520-0469(1986)043<1198:LSITCB>2
 1160 .0.CO;2
- 1161 Li, D., & Bou-Zeid, E. (2011, August). Coherent Structures and the Dissimilarity of
 1162 Turbulent Transport of Momentum and Scalars in the Unstable Atmospheric Surface
 1163 Layer. *Boundary-Layer Meteorology*, 140(2), 243–262. Retrieved 2020-12-21, from
 1164 <http://link.springer.com/10.1007/s10546-011-9613-5> doi: 10.1007/s10546-011-
 1165 -9613-5
- 1166 Mahrt, L. (1998). Flux Sampling Errors for Aircraft and Towers. *JOURNAL OF ATMOSPHERIC AND OCEANIC TECHNOLOGY*, 15, 14.
- 1167
 1168 Mahrt, L. (2010, April). Computing turbulent fluxes near the surface: Needed improve-
 1169 ments. *Agricultural and Forest Meteorology*, 150(4), 501–509. Retrieved 2020-10-12,
 1170 from <https://linkinghub.elsevier.com/retrieve/pii/S0168192310000389> doi:
 1171 10.1016/j.agrformet.2010.01.015
- 1172 Margairaz, F., Pardyjak, E. R., & Calaf, M. (2020, June). Surface Thermal Hetero-
 1173 geneities and the Atmospheric Boundary Layer: The Relevance of Dispersive
 1174 Fluxes. *Boundary-Layer Meteorology*, 175(3), 369–395. Retrieved 2020-10-13, from
 1175 <http://link.springer.com/10.1007/s10546-020-00509-w> doi: 10.1007/s10546-
 1176 -020-00509-w
- 1177 Maronga, B., & Raasch, S. (2013, January). Large-Eddy Simulations of Surface Heterogene-
 1178 ity Effects on the Convective Boundary Layer During the LITFASS-2003 Experiment.
 1179 *Boundary-Layer Meteorology*, 146(1), 17–44. Retrieved 2019-06-26, from [http://
 1180 link.springer.com/10.1007/s10546-012-9748-z](http://link.springer.com/10.1007/s10546-012-9748-z) doi: 10.1007/s10546-012-9748-z
- 1181 Mauder, M., Desjardins, R. L., & MacPherson, I. (2007, July). Scale analysis of airborne
 1182 flux measurements over heterogeneous terrain in a boreal ecosystem: SCALE ANAL-
 1183 YSIS OF FLUX MEASUREMENTS. *Journal of Geophysical Research: Atmospheres*,
 1184 112(D13), n/a–n/a. Retrieved 2019-07-25, from [http://doi.wiley.com/10.1029/
 1185 2006JD008133](http://doi.wiley.com/10.1029/2006JD008133) doi: 10.1029/2006JD008133
- 1186 Mauder, M., Desjardins, R. L., & MacPherson, I. (2008, December). Creating Surface Flux
 1187 Maps from Airborne Measurements: Application to the Mackenzie Area GEWEX
 1188 Study MAGS 1999. *Boundary-Layer Meteorology*, 129(3), 431–450. Retrieved 2019-12-
 1189 21, from <http://link.springer.com/10.1007/s10546-008-9326-6> doi: 10.1007/
 1190 s10546-008-9326-6
- 1191 Mauder, M., Desjardins, R. L., Pattey, E., Gao, Z., & van Haarlem, R. (2008, July). Mea-
 1192 surement of the Sensible Eddy Heat Flux Based on Spatial Averaging of Continuous
 1193 Ground-Based Observations. *Boundary-Layer Meteorology*, 128(1), 151–172. Re-
 1194 trieved 2022-03-09, from <http://link.springer.com/10.1007/s10546-008-9279-9>
 1195 doi: 10.1007/s10546-008-9279-9
- 1196 Mauder, M., Foken, T., & Cuxart, J. (2020, May). Surface-Energy-Balance Closure over
 1197 Land: A Review. *Boundary-Layer Meteorology*. Retrieved 2020-06-10, from [http://
 1198 link.springer.com/10.1007/s10546-020-00529-6](http://link.springer.com/10.1007/s10546-020-00529-6) doi: 10.1007/s10546-020-00529-6

- 1200 Mauder, M., Ibrom, A., Wanner, L., De Roo, F., Brügger, P., Kiese, R., & Pilegaard, K.
 1201 (2021, June). *Options to correct local turbulent flux measurements for large-scale fluxes*
 1202 *using a LES-based approach* (preprint). Others (Wind, Precipitation, Temperature,
 1203 etc.)/In Situ Measurement/Data Processing and Information Retrieval. Retrieved
 1204 2021-07-07, from <https://amt.copernicus.org/preprints/amt-2021-126/> doi:
 1205 10.5194/amt-2021-126
- 1206 Mauder, M., Oncley, S. P., Vogt, R., Weidinger, T., Ribeiro, L., Bernhofer, C., ... Liu, H.
 1207 (2007, April). The energy balance experiment EBEX-2000. Part II: Intercomparison
 1208 of eddy-covariance sensors and post-field data processing methods. *Boundary-Layer*
 1209 *Meteorology*, *123*(1), 29–54. Retrieved 2020-11-29, from [http://link.springer.com/](http://link.springer.com/10.1007/s10546-006-9139-4)
 1210 [10.1007/s10546-006-9139-4](http://link.springer.com/10.1007/s10546-006-9139-4) doi: 10.1007/s10546-006-9139-4
- 1211 Meijninger, W. M. L., Beyrich, F., Lüdi, A., Kohsiek, W., & Bruin, H. A. R. D. (2006,
 1212 October). Scintillometer-Based Turbulent Fluxes of Sensible and Latent Heat Over
 1213 a Heterogeneous Land Surface – A Contribution to Litfass-2003. *Boundary-Layer*
 1214 *Meteorology*, *121*(1), 89–110. Retrieved 2022-02-09, from [https://doi.org/10.1007/](https://doi.org/10.1007/s10546-005-9022-8)
 1215 [s10546-005-9022-8](https://doi.org/10.1007/s10546-005-9022-8) doi: 10.1007/s10546-005-9022-8
- 1216 Metzger, S., Durden, D., Paleri, S., Sühling, M., Butterworth, B. J., Florian, C., ... Desai,
 1217 A. R. (2021, November). Novel approach to observing system simulation experiments
 1218 improves information gain of surface–atmosphere field measurements. *Atmospheric*
 1219 *Measurement Techniques*, *14*(11), 6929–6954. Retrieved 2022-01-25, from [https://](https://amt.copernicus.org/articles/14/6929/2021/)
 1220 amt.copernicus.org/articles/14/6929/2021/ doi: 10.5194/amt-14-6929-2021
- 1221 Metzger, S., Durden, D., Sturtevant, C., Luo, H., Pingintha-Durden, N., Sachs, T., ...
 1222 Desai, A. R. (2017, August). eddy4R 0.2.0: a DevOps model for community-
 1223 extensible processing and analysis of eddy-covariance data based on R, Git, Docker,
 1224 and HDF5. *Geoscientific Model Development*, *10*(9), 3189–3206. Retrieved 2019-11-
 1225 07, from <https://www.geosci-model-dev.net/10/3189/2017/> ([Software]) doi:
 1226 10.5194/gmd-10-3189-2017
- 1227 Metzger, S., Junkermann, W., Mauder, M., Butterbach-Bahl, K., Trancón y Widemann,
 1228 B., Neidl, F., ... Foken, T. (2013, April). Spatially explicit regionalization of air-
 1229 borne flux measurements using environmental response functions. *Biogeosciences*,
 1230 *10*(4), 2193–2217. Retrieved 2019-12-20, from [https://www.biogeosciences.net/](https://www.biogeosciences.net/10/2193/2013/)
 1231 [10/2193/2013/](https://www.biogeosciences.net/10/2193/2013/) doi: 10.5194/bg-10-2193-2013
- 1232 Monin, A., & Obukhov, A. (1954). Osnovnye zakonomernosti turbulentnogo peremeshivaniya
 1233 v prizemnom sloe atmosfery (basic laws of turbulent mixing in the atmosphere near
 1234 the ground). *Trudy geofiz. inst. AN SSSR*, *24*(151), 163–187.
- 1235 Morrison, T., Calaf, M., Higgins, C. W., Drake, S. A., Perelet, A., & Pardyjak, E. (2021,
 1236 August). The Impact of Surface Temperature Heterogeneity on Near-Surface Heat
 1237 Transport. *Boundary-Layer Meteorology*, *180*(2), 247–272. Retrieved 2022-03-09,
 1238 from <https://link.springer.com/10.1007/s10546-021-00624-2> doi: 10.1007/
 1239 [s10546-021-00624-2](https://link.springer.com/10.1007/s10546-021-00624-2)
- 1240 Nordbo, A., & Katul, G. (2013, January). A Wavelet-Based Correction Method
 1241 for Eddy-Covariance High-Frequency Losses in Scalar Concentration Measurements.
 1242 *Boundary-Layer Meteorology*, *146*(1), 81–102. Retrieved 2019-12-21, from [http://](http://link.springer.com/10.1007/s10546-012-9759-9)
 1243 link.springer.com/10.1007/s10546-012-9759-9 doi: 10.1007/s10546-012-9759-9
- 1244 Obukhov, A. (1946). Turbulentnost'v temperaturnoj-neodnorodnoj atmosfere. *Trudy Inst.*
 1245 *Theor. Geofiz. AN SSSR*, *1*, 95–115.
- 1246 Oncley, S. P., Foken, T., Vogt, R., Kohsiek, W., DeBruin, H. A. R., Bernhofer, C., ...
 1247 Weidinger, T. (2007, March). The Energy Balance Experiment EBEX-2000. Part I:
 1248 overview and energy balance. *Boundary-Layer Meteorology*, *123*(1), 1–28. Retrieved
 1249 2020-11-29, from <http://link.springer.com/10.1007/s10546-007-9161-1> doi:
 1250 [10.1007/s10546-007-9161-1](http://link.springer.com/10.1007/s10546-007-9161-1)
- 1251 Orlanski, I. (1975). A rational subdivision of scales for atmospheric processes. *Bulletin of*
 1252 *the American Meteorological Society*, 527–530.
- 1253 Pielke, R. A., Sr., Avissar, R., Raupach, M., Dolman, A. J., Zeng, X., & Denning, A. S.

- 1254 (1998). Interactions between the atmosphere and terrestrial ecosystems: influence on
 1255 weather and climate. *Global Change Biology*, 4(5), 461–475. Retrieved from [https://](https://onlinelibrary.wiley.com/doi/abs/10.1046/j.1365-2486.1998.t01-1-00176.x)
 1256 onlinelibrary.wiley.com/doi/abs/10.1046/j.1365-2486.1998.t01-1-00176.x
 1257 (_eprint: [https://onlinelibrary.wiley.com/doi/pdf/10.1046/j.1365-2486.1998.t01-1-](https://onlinelibrary.wiley.com/doi/pdf/10.1046/j.1365-2486.1998.t01-1-00176.x)
 1258 [00176.x](https://onlinelibrary.wiley.com/doi/pdf/10.1046/j.1365-2486.1998.t01-1-00176.x)) doi: <https://doi.org/10.1046/j.1365-2486.1998.t01-1-00176.x>
- 1259 Rey-Sanchez, C., Arias-Ortiz, A., Kasak, K., Chu, H., Szutu, D., Verfaillie, J., & Baldocchi,
 1260 D. (2022). Detecting hot spots of methane flux using footprint-weighted flux maps.
 1261 *Journal of Geophysical Research: Biogeosciences*, 127(8), e2022JG006977.
- 1262 Rodi, A. (2011). King of the air: The evolution and capabilities of wyoming’s observation
 1263 aircraft. *Meteorological Technology International*, 44–47.
- 1264 Rodi, A. R., & Leon, D. C. (2012). Correction of static pressure on a research aircraft
 1265 in accelerated flight using differential pressure measurements. *Atmospheric Measure-*
 1266 *ment Techniques*, 5(11), 2569–2579. Retrieved from [https://amt.copernicus.org/](https://amt.copernicus.org/articles/5/2569/2012/)
 1267 [articles/5/2569/2012/](https://amt.copernicus.org/articles/5/2569/2012/) doi: 10.5194/amt-5-2569-2012
- 1268 Rodi, A. R., & Spyers-Duran, P. A. (1972). Analysis of Time Response of Airborne
 1269 Temperature Sensors. *Journal of Applied Meteorology and Climatology*, 11(3), 554
 1270 – 556. Retrieved from [https://journals.ametsoc.org/view/journals/apme/11/](https://journals.ametsoc.org/view/journals/apme/11/3/1520-0450_1972_011_0554_aotroa_2_0_co_2.xml)
 1271 [3/1520-0450_1972_011_0554_aotroa_2_0_co_2.xml](https://journals.ametsoc.org/view/journals/apme/11/3/1520-0450_1972_011_0554_aotroa_2_0_co_2.xml) (Place: Boston MA, USA Pub-
 1272 lisher: American Meteorological Society) doi: 10.1175/1520-0450(1972)011<0554:
 1273 AOTROA>2.0.CO;2
- 1274 Salesky, S., & Anderson, W. (2020, September). Coherent Structures Modulate Atmospheric
 1275 Surface Layer Flux-Gradient Relationships. *Physical Review Letters*, 125(12), 124501.
 1276 Retrieved 2020-10-20, from [https://link.aps.org/doi/10.1103/PhysRevLett.125](https://link.aps.org/doi/10.1103/PhysRevLett.125.124501)
 1277 [.124501](https://link.aps.org/doi/10.1103/PhysRevLett.125.124501) doi: 10.1103/PhysRevLett.125.124501
- 1278 Salesky, S. T., Chamecki, M., & Bou-Zeid, E. (2017, April). On the Nature of the Tran-
 1279 sition Between Roll and Cellular Organization in the Convective Boundary Layer.
 1280 *Boundary-Layer Meteorology*, 163(1), 41–68. Retrieved 2020-12-21, from [http://](http://link.springer.com/10.1007/s10546-016-0220-3)
 1281 link.springer.com/10.1007/s10546-016-0220-3 doi: 10.1007/s10546-016-0220-3
- 1282 Scott, D. W. (1979). On optimal and data-based histograms. *Biometrika*, 66(3), 605–610.
- 1283 Scott, D. W. (2015). *Multivariate density estimation: theory, practice, and visualization*.
 1284 John Wiley & Sons.
- 1285 Starr, E., & Goldfarb, B. (2020). Binned scatterplots: A simple tool to make research easier
 1286 and better. *Strategic Management Journal*, 41(12), 2261–2274.
- 1287 Steinfeld, G., Letzel, M. O., Raasch, S., Kanda, M., & Inagaki, A. (2007, March). Spa-
 1288 tial representativeness of single tower measurements and the imbalance problem with
 1289 eddy-covariance fluxes: results of a large-eddy simulation study. *Boundary-Layer Me-*
 1290 *teorology*, 123(1), 77–98. Retrieved 2019-06-26, from [http://link.springer.com/](http://link.springer.com/10.1007/s10546-006-9133-x)
 1291 [10.1007/s10546-006-9133-x](http://link.springer.com/10.1007/s10546-006-9133-x) doi: 10.1007/s10546-006-9133-x
- 1292 Stoy, P. C., Mauder, M., Foken, T., Marcolla, B., Boegh, E., Ibrom, A., ... Varlagin, A.
 1293 (2013, April). A data-driven analysis of energy balance closure across FLUXNET
 1294 research sites: The role of landscape scale heterogeneity. *Agricultural and Forest*
 1295 *Meteorology*, 171-172, 137–152. Retrieved 2019-12-19, from [https://linkinghub](https://linkinghub.elsevier.com/retrieve/pii/S0168192312003413)
 1296 [.elsevier.com/retrieve/pii/S0168192312003413](https://linkinghub.elsevier.com/retrieve/pii/S0168192312003413) doi: 10.1016/j.agrformet.2012
 1297 .11.004
- 1298 Strunin, M. A., & Hiyama, T. (2004, November). Applying wavelet transforms to analyse
 1299 aircraft-measured turbulence and turbulent fluxes in the atmospheric boundary layer
 1300 over eastern Siberia. *Hydrological Processes*, 18(16), 3081–3098. Retrieved 2019-07-26,
 1301 from <http://doi.wiley.com/10.1002/hyp.5750> doi: 10.1002/hyp.5750
- 1302 Strunin, M. A., & Hiyama, T. (2005, December). Spectral Structure of Small-Scale Tur-
 1303 bulent and Mesoscale Fluxes in the Atmospheric Boundary Layer over a Thermally
 1304 Inhomogeneous Land Surface. *Boundary-Layer Meteorology*, 117(3), 479–510. Re-
 1305 trieved 2019-07-26, from <http://link.springer.com/10.1007/s10546-005-2188-2>
 1306 [doi: 10.1007/s10546-005-2188-2](http://link.springer.com/10.1007/s10546-005-2188-2)
- 1307 Strunin, M. A., Hiyama, T., Asanuma, J., & Ohata, T. (2004, June). Aircraft Observations
 1308 of the Development of Thermal Internal Boundary Layers and Scaling of the Convec-

- 1309 tive Boundary Layer Over Non-Homogeneous Land Surfaces. *Boundary-Layer Meteorology*, 111(3), 491–522. Retrieved 2019-07-11, from <http://link.springer.com/10.1023/B:BOUN.0000016542.72958.e9> doi: 10.1023/B:BOUN.0000016542.72958.e9
- 1310
- 1311
- 1312 Stull, R. B. (1988). An Introduction to Boundary Layer Meteorology. In R. B. Stull (Ed.),
- 1313 *An Introduction to Boundary Layer Meteorology* (pp. 1–27). Dordrecht: Springer
- 1314 Netherlands. Retrieved 2021-01-01, from [http://link.springer.com/10.1007/978-](http://link.springer.com/10.1007/978-94-009-3027-8_1)
- 1315 [94-009-3027-8_1](http://link.springer.com/10.1007/978-94-009-3027-8_1) doi: 10.1007/978-94-009-3027-8_1
- 1316 Sun, J., Desjardins, R., Mahrt, L., & MacPherson, I. (1998, October). Transport of carbon
- 1317 dioxide, water vapor, and ozone by turbulence and local circulations. *Journal of*
- 1318 *Geophysical Research: Atmospheres*, 103(D20), 25873–25885. Retrieved 2020-10-13,
- 1319 from <http://doi.wiley.com/10.1029/98JD02439> doi: 10.1029/98JD02439
- 1320 Thomas, C., & Foken, T. (2005, April). Detection of long-term coherent exchange over
- 1321 spruce forest using wavelet analysis. *Theoretical and Applied Climatology*, 80(2-4),
- 1322 91–104. Retrieved 2020-04-22, from [http://link.springer.com/10.1007/s00704-](http://link.springer.com/10.1007/s00704-004-0093-0)
- 1323 [004-0093-0](http://link.springer.com/10.1007/s00704-004-0093-0) doi: 10.1007/s00704-004-0093-0
- 1324 Torrence, C., & Compo, G. P. (1998). A Practical Guide to Wavelet Analysis. *Bulletin of*
- 1325 *the American Meteorological Society*, 79(1), 18.
- 1326 Wang, Z., French, J., Vali, G., Wechsler, P., Haimov, S., Rodi, A., . . . Pazmany, A. L. (2012,
- 1327 May). Single Aircraft Integration of Remote Sensing and In Situ Sampling for the
- 1328 Study of Cloud Microphysics and Dynamics. *Bulletin of the American Meteorological*
- 1329 *Society*, 93(5), 653–668. Retrieved 2022-04-12, from [https://journals.ametsoc](https://journals.ametsoc.org/doi/10.1175/BAMS-D-11-00044.1)
- 1330 [.org/doi/10.1175/BAMS-D-11-00044.1](https://journals.ametsoc.org/doi/10.1175/BAMS-D-11-00044.1) doi: 10.1175/BAMS-D-11-00044.1
- 1331 Wanner, L., Calaf, M., & Mauder, M. (2022). Incorporating the effect of heterogeneous
- 1332 surface heating into a semi-empirical model of the surface energy balance closure. *PloS*
- 1333 *one*, 17(6), e0268097.
- 1334 Wulfmeyer, V., Turner, D. D., Baker, B., Banta, R., Behrendt, A., Bonin, T., . . . Weck-
- 1335 werth, T. (2018, August). A New Research Approach for Observing and Character-
- 1336 izing Land–Atmosphere Feedback. *Bulletin of the American Meteorological Society*,
- 1337 99(8), 1639–1667. Retrieved 2019-12-24, from [http://journals.ametsoc.org/doi/](http://journals.ametsoc.org/doi/10.1175/BAMS-D-17-0009.1)
- 1338 [10.1175/BAMS-D-17-0009.1](http://journals.ametsoc.org/doi/10.1175/BAMS-D-17-0009.1) doi: 10.1175/BAMS-D-17-0009.1
- 1339 Xu, F., Wang, W., Wang, J., Xu, Z., Qi, Y., & Wu, Y. (2017, August). Area-averaged evap-
- 1340 otranspiration over a heterogeneous land surface: aggregation of multi-point EC flux
- 1341 measurements with a high-resolution land-cover map and footprint analysis. *Hydrology*
- 1342 *and Earth System Sciences*, 21(8), 4037–4051. Retrieved 2020-10-12, from [https://](https://hess.copernicus.org/articles/21/4037/2017/)
- 1343 hess.copernicus.org/articles/21/4037/2017/ doi: 10.5194/hess-21-4037-2017
- 1344 Xu, K., Sühling, M., Metzger, S., Durden, D., & Desai, A. R. (2020, April). Can Data
- 1345 Mining Help Eddy Covariance See the Landscape? A Large-Eddy Simulation Study.
- 1346 *Boundary-Layer Meteorology*. Retrieved 2020-05-08, from [http://link.springer](http://link.springer.com/10.1007/s10546-020-00513-0)
- 1347 [.com/10.1007/s10546-020-00513-0](http://link.springer.com/10.1007/s10546-020-00513-0) doi: 10.1007/s10546-020-00513-0
- 1348 Zhang, G., Leclerc, M. Y., Duarte, H. F., Durden, D., Werth, D., Kurzeja, R., & Parker,
- 1349 M. (2014, March). Multi-scale decomposition of turbulent fluxes above a forest
- 1350 canopy. *Agricultural and Forest Meteorology*, 186, 48–63. Retrieved 2021-01-20,
- 1351 from <https://linkinghub.elsevier.com/retrieve/pii/S0168192313003006> doi:
- 1352 10.1016/j.agrformet.2013.11.010
- 1353 Zhang, Y., Liu, H., Foken, T., Williams, Q. L., Liu, S., Mauder, M., & Liebethal, C.
- 1354 (2010, August). Turbulence Spectra and Cospectra Under the Influence of Large
- 1355 Eddies in the Energy Balance Experiment (EBEX). *Boundary-Layer Meteorology*,
- 1356 136(2), 235–251. Retrieved 2020-10-13, from [http://link.springer.com/10.1007/](http://link.springer.com/10.1007/s10546-010-9504-1)
- 1357 [s10546-010-9504-1](http://link.springer.com/10.1007/s10546-010-9504-1) doi: 10.1007/s10546-010-9504-1
- 1358 Zhou, Y., Li, D., & Li, X. (2019, August). The Effects of Surface Heterogeneity Scale on
- 1359 the Flux Imbalance under Free Convection. *Journal of Geophysical Research: Atmo-*
- 1360 *spheres*, 2018JD029550. Retrieved 2019-12-19, from [https://onlinelibrary.wiley](https://onlinelibrary.wiley.com/doi/abs/10.1029/2018JD029550)
- 1361 [.com/doi/abs/10.1029/2018JD029550](https://onlinelibrary.wiley.com/doi/abs/10.1029/2018JD029550) doi: 10.1029/2018JD029550

Supporting Information for ”Space - scale resolved surface-atmospheric fluxes across a heterogeneous mid-latitude forested landscape”

Sreenath Paleri ¹, Ankur R. Desai ¹, Stefan Metzger ^{2,1}, David Durden ²,

Brian J. Butterworth ^{3,4}, Matthias Mauder ^{5,6}, Katrin Kohnert ^{7 *}, Andrei

Serafimovich ^{7 †}

¹Department of Atmospheric and Oceanic Sciences, University of Wisconsin-Madison, Madison, Wisconsin, USA

²Battelle, National Ecological Observatory Network, 1685 38th Street, Boulder, Colorado, USA

³Cooperative Institute for Research in Environmental Sciences, University of Colorado, Boulder, Colorado, USA

⁴NOAA Physical Sciences Laboratory, Boulder, Colorado, USA

⁵Institute of Hydrology and Meteorology, Technische Universität Dresden, Dresden, Germany

⁶Institute of Meteorology and Climate Research – Atmospheric Environmental Research, Karlsruhe Institute of Technology,

Garmisch-Partenkirchen, Germany

⁷ GFZ German Research Centre for Geosciences, Telegrafenberg, Potsdam, Germany

Corresponding author: Sreenath Paleri, Dept of Atmospheric and Oceanic Sciences, University of Wisconsin-Madison, Madison, WI 53706, USA. (paleri@wisc.edu)

*Now at: German Council of Experts on
Climate Change, Berlin, Germany

†Now at: Deutscher Wetterdienst,
Offenbach, Germany

Contents of this file

1. Table S1
2. Figures S1 to S18

Table S1. IOP averaged scale-resolved heat fluxes. RMS error values scaled by $\sqrt{N_{samples}}$

IOP	Total LE	Total H	Turb. LE	Meso. LE	Turb. H	Meso. H
July	179.98 ± 4.78	88.31 ± 0.94	123.07 ± 2.40	56.92 ± 4.14	71.25 ± 0.74	17.05 ± 0.58
Aug.	256.44 ± 2.92	88.04 ± 1.02	210.28 ± 2.38	46.16 ± 1.69	68.02 ± 0.78	20.01 ± 0.66
Sep.	69.01 ± 2.86	89.13 ± 1.13	49.36 ± 1.87	19.65 ± 2.17	76.36 ± 0.78	12.77 ± 0.81

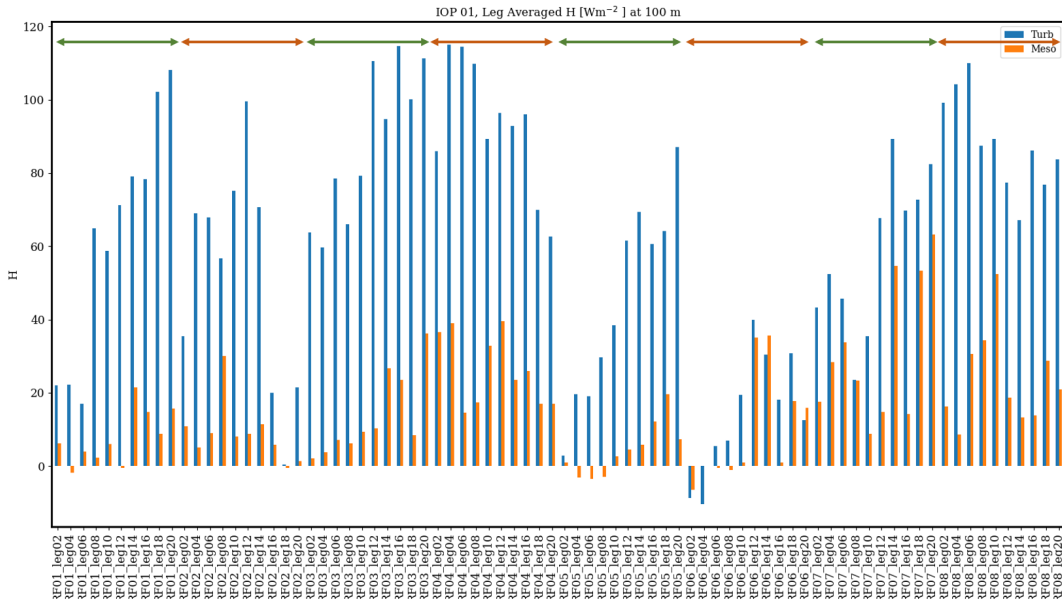


Figure S1. Flight leg averaged, scale-resolved sensible heat fluxes at 100m for the July IOP. x axis shows flight leg names. Arrows at the top of the figure span the length of one research flight. Green arrows cover morning flights and orange arrows cover afternoon flights.

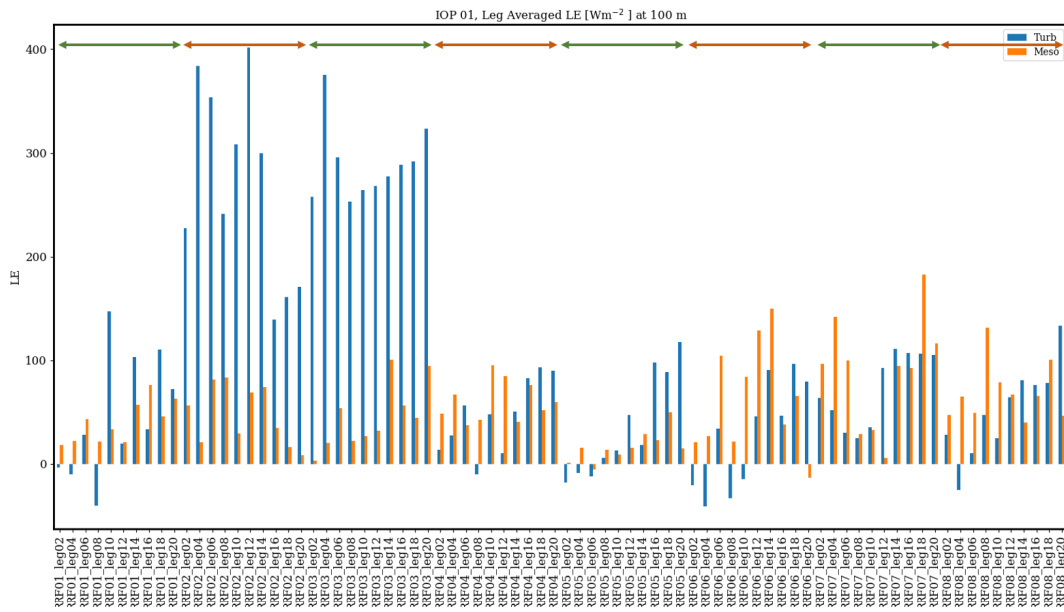


Figure S2. Flight leg averaged, scale-resolved latent heat fluxes at 100m for the July IOP. x axis shows flight leg names. Arrows at the top of the figure span the length of one research flight. Green arrows cover morning flights and orange arrows cover afternoon flights.

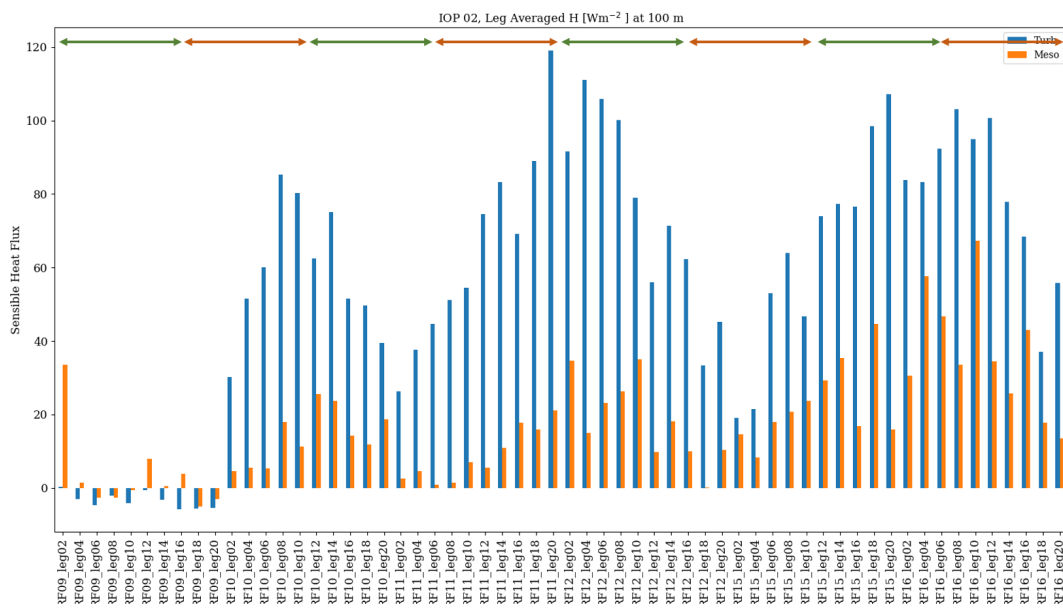


Figure S3. Flight leg averaged, scale-resolved sensible heat fluxes at 100m for the August IOP. x axis shows flight leg names. Arrows at the top of the figure span the length of one research flight. Green arrows cover morning flights and orange arrows cover afternoon flights.

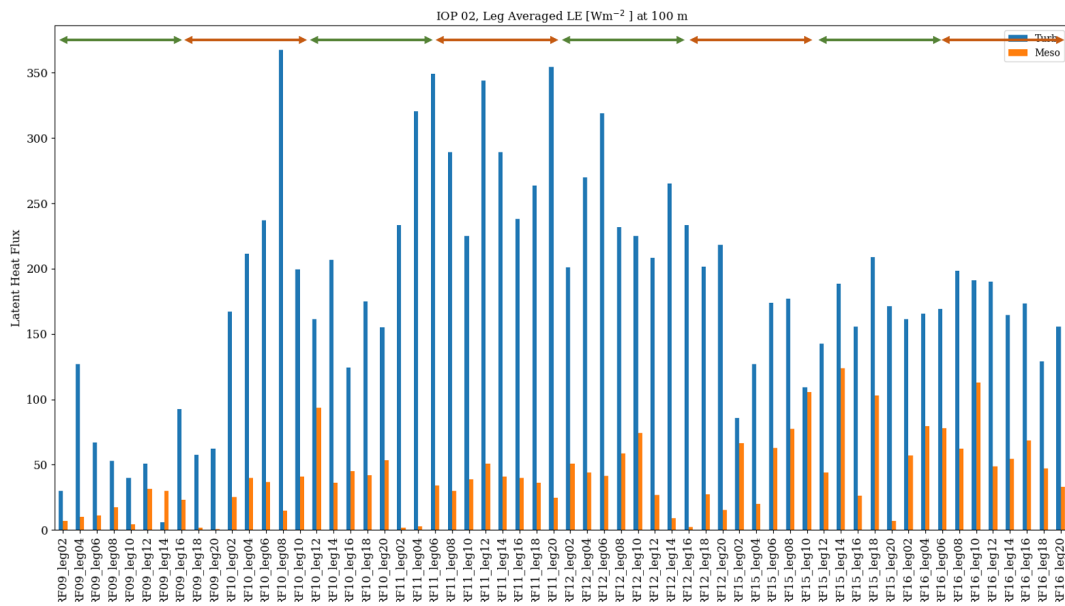


Figure S4. Flight leg averaged, scale-resolved latent heat fluxes at 100m for the August IOP. x axis shows flight leg names. Arrows at the top of the figure span the length of one research flight. Green arrows cover morning flights and orange arrows cover afternoon flights.

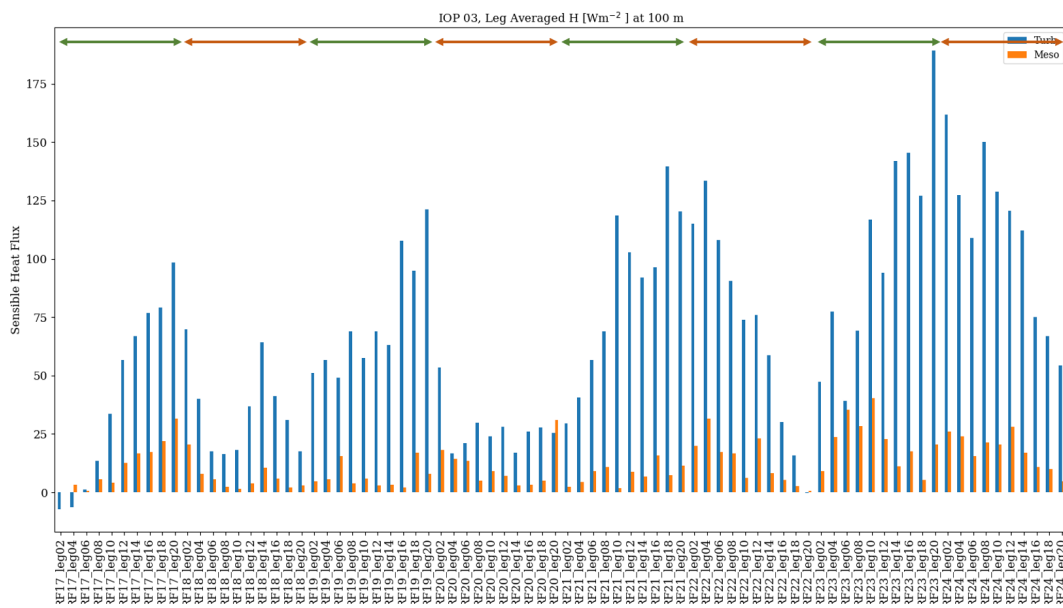


Figure S5. Flight leg averaged, scale-resolved sensible heat fluxes at 100m for the September IOP. x axis shows flight leg names. Arrows at the top of the figure span the length of one research flight. Green arrows cover morning flights and orange arrows cover afternoon flights.

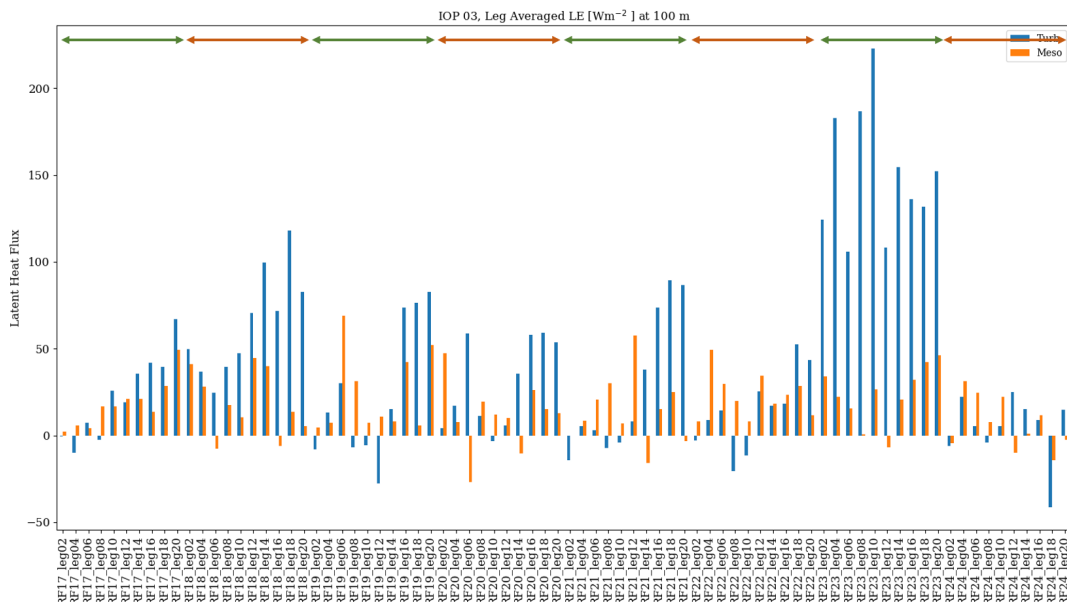


Figure S6. Flight leg averaged, scale-resolved latent heat fluxes at 100m for the September IOP. x axis shows flight leg names. Arrows at the top of the figure span the length of one research flight. Green arrows cover morning flights and orange arrows cover afternoon flights.

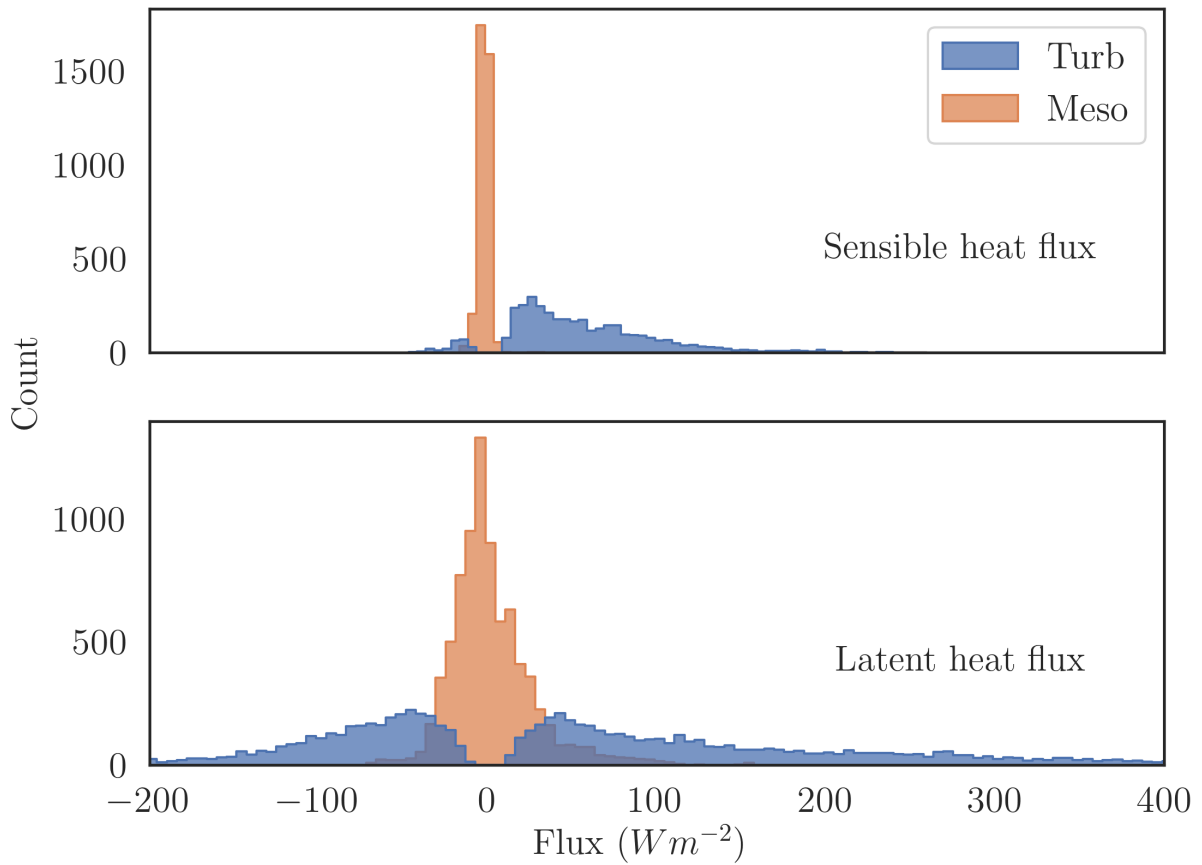


Figure S7. Histograms of turbulent and mesoscale fluxes for cases when the measured mesoscale fractions are lesser than 0

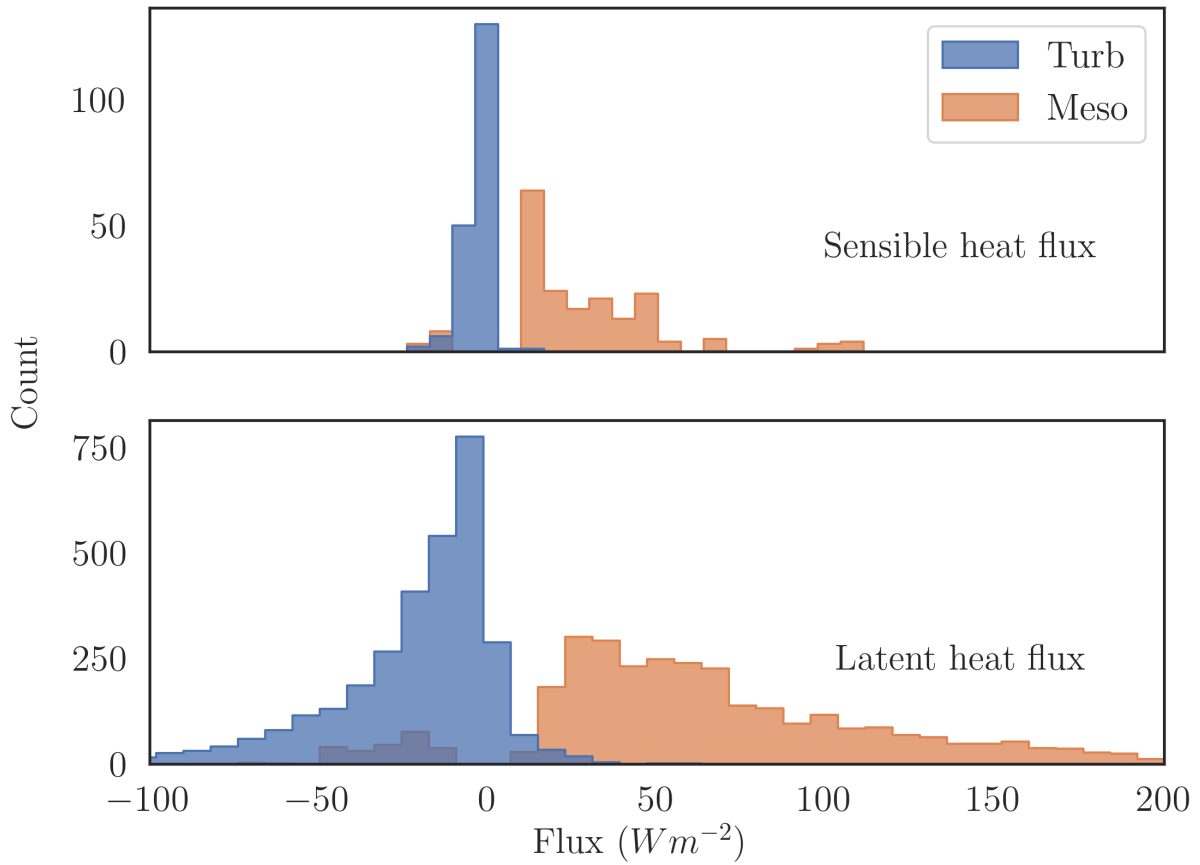


Figure S8. Histograms of turbulent and mesoscale fluxes for cases when the measured mesoscale fractions are greater than 1

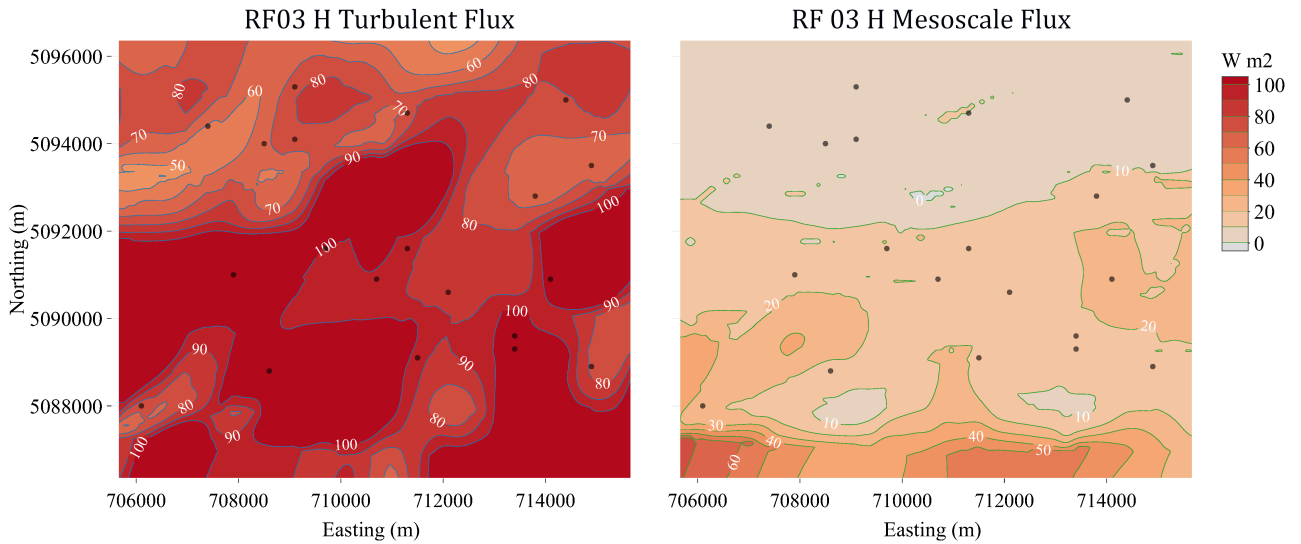


Figure S9. Turbulent (left) and mesoscale (right) sensible heat flux topographies for Research Flight 03 in the July IOP, 11 Jul. 09:20 to 11:20 CDT, over the 10x10 km CHEESEHEAD core domain. The brown dots are the NCAR-ISFS tower locations.

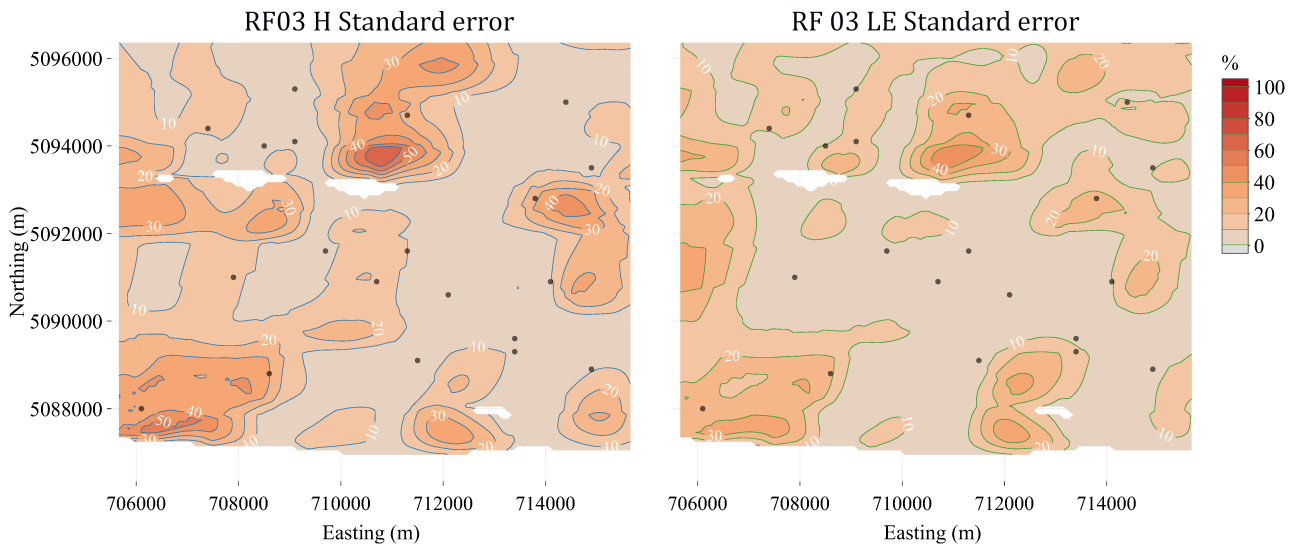


Figure S10. Standard error topographies for sensible (left) and latent (right) heat fluxes for Research Flight 03 in the July IOP, 11 Jul. 09:20 to 11:20 CDT, over the 10x10 km CHEESEHEAD core domain. The brown dots are the NCAR-ISFS tower locations.

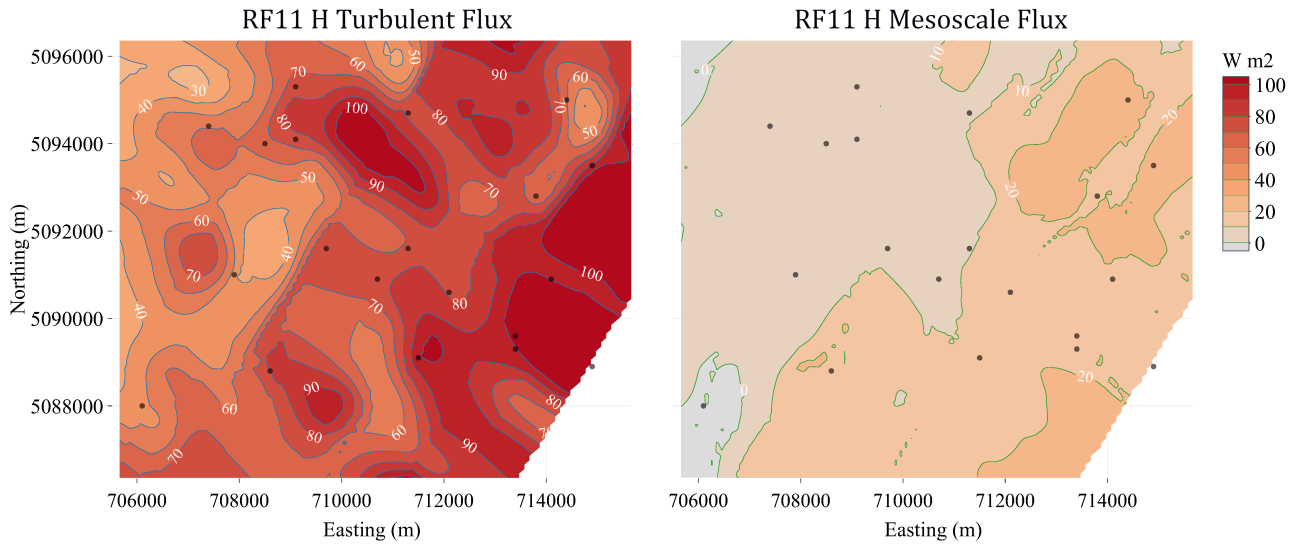


Figure S11. Turbulent (left) and mesoscale (right) sensible heat flux topographies for Research Flight 11 in the August IOP, 21 Aug. 09:00 to 11:30 CDT, over the 10x10 km CHEESEHEAD core domain. The brown dots are the NCAR-ISFS tower locations.

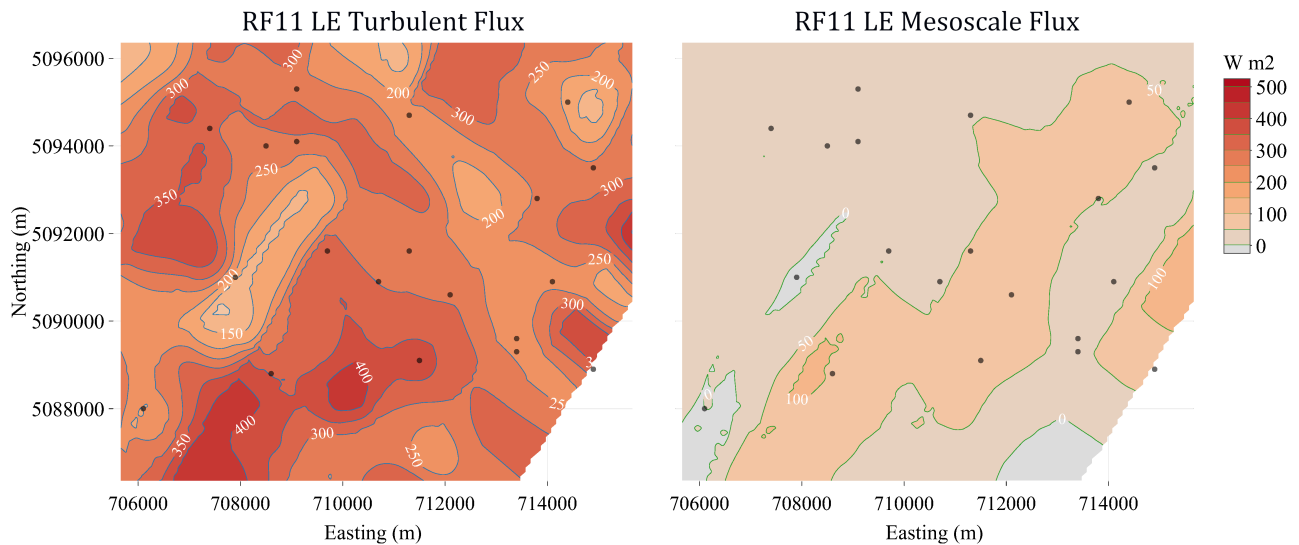


Figure S12. Turbulent (left) and mesoscale (right) latent heat flux topographies for Research Flight 11 in the August IOP, 21 Aug. 09:00 to 11:30 CDT, over the 10x10 km CHEESEHEAD core domain. The brown dots are the NCAR-ISFS tower locations.

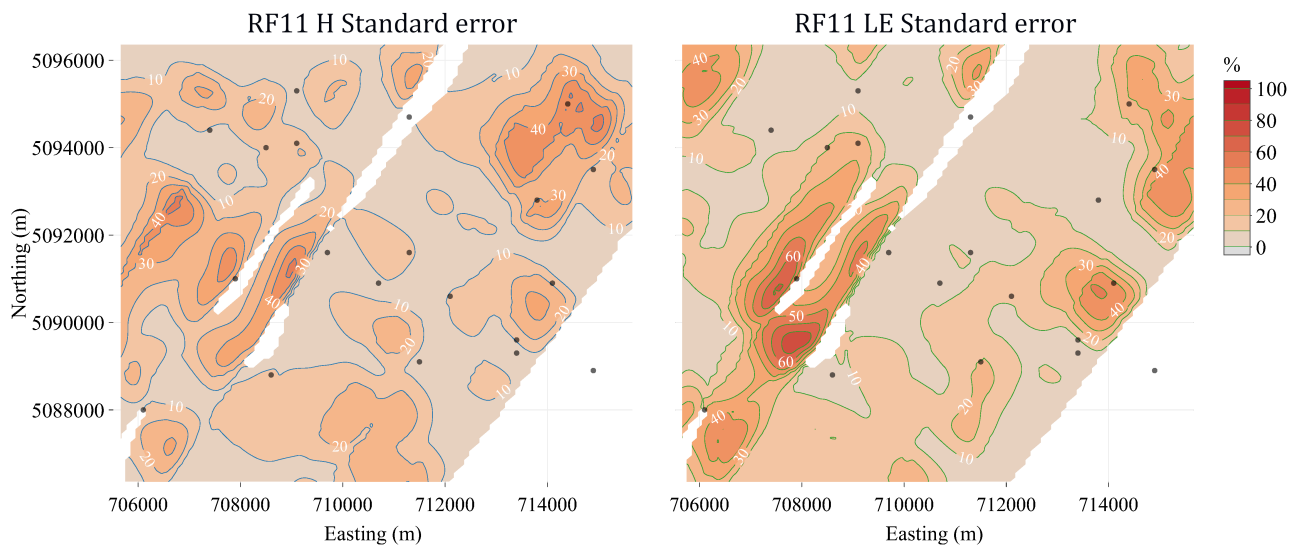


Figure S13. Standard error topographies for sensible (left) and latent (right) heat fluxes for Research Flight 11 in the August IOP, 21 Aug. 09:00 to 11:30 CDT, over the 10x10 km CHEESEHEAD core domain. The brown dots are the NCAR-ISFS tower locations.

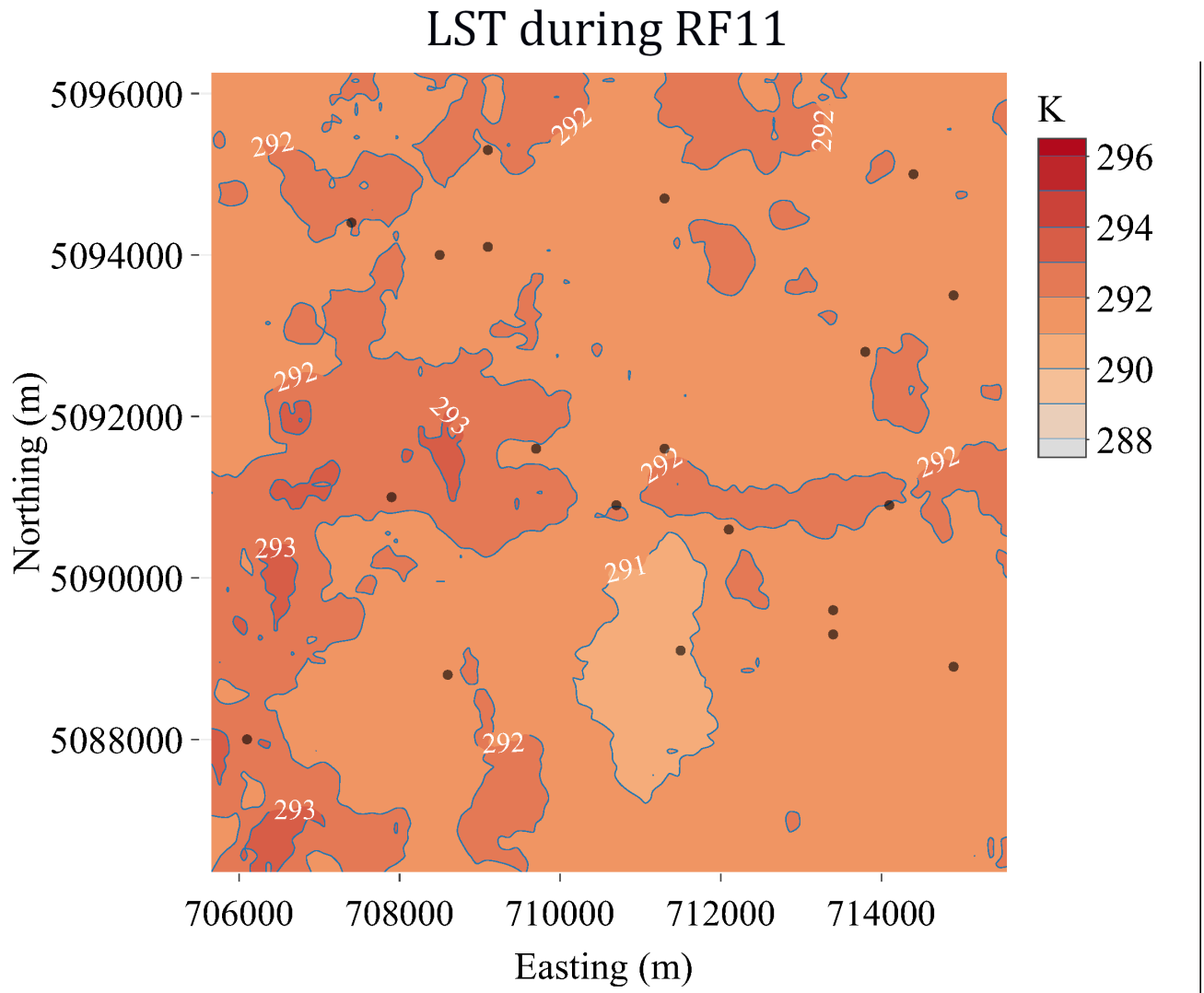


Figure S14. Fusion Land Surface Temperature data for the 10x10 km domain during Research Flight 11, 21 Aug. 2019 09:00 to 11:30 CDT , from Desai et al. (2021)

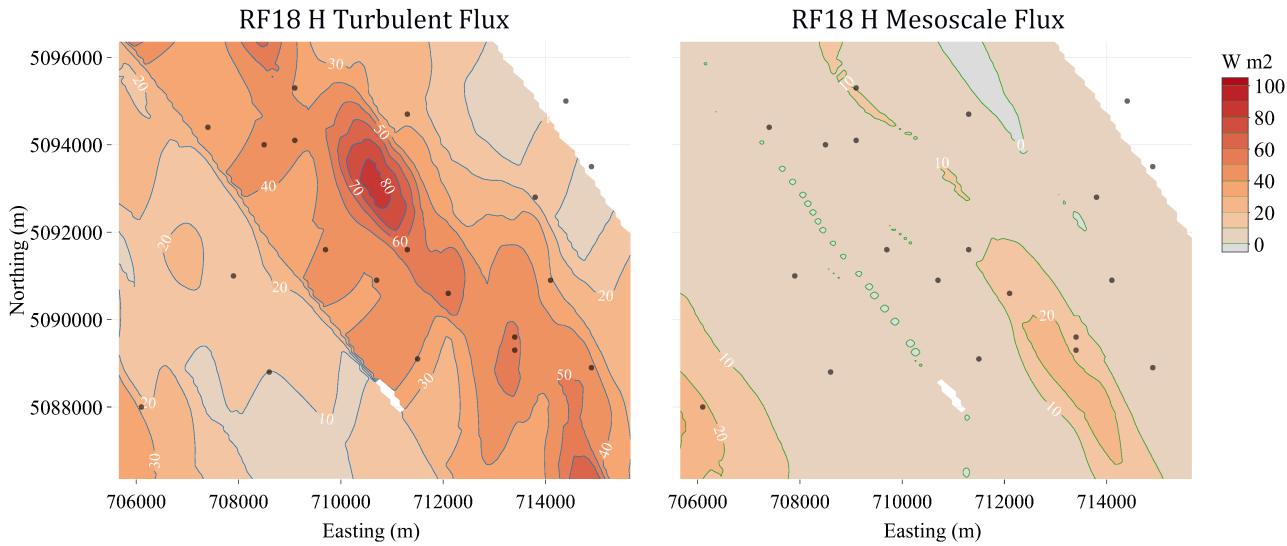


Figure S15. Turbulent (left) and mesoscale (right) sensible heat flux topographies for Research Flight 18 in the September IOP, 24 Sep. 14:00 to 16:30 CDT, over the 10x10 km CHEESEHEAD core domain. The brown dots are the NCAR-ISFS tower locations.

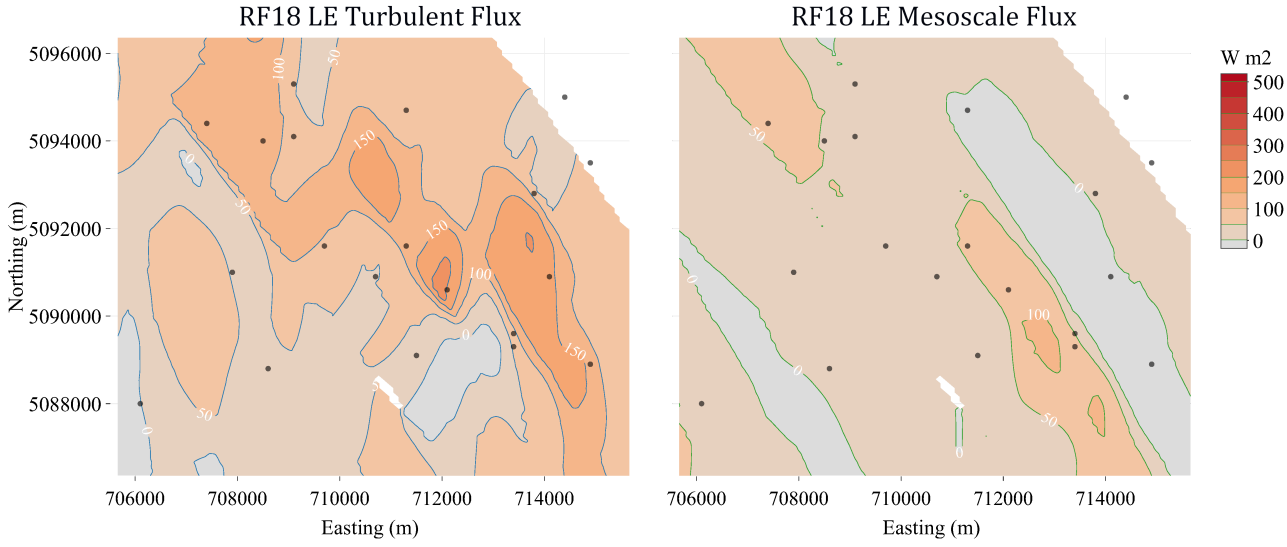


Figure S16. Turbulent (left) and mesoscale (right) latent heat flux topographies for Research Flight 18 in the September IOP, 24 Sep. 14:00 to 16:30 CDT, over the 10x10 km CHEESEHEAD core domain. The brown dots are the NCAR-ISFS tower locations.

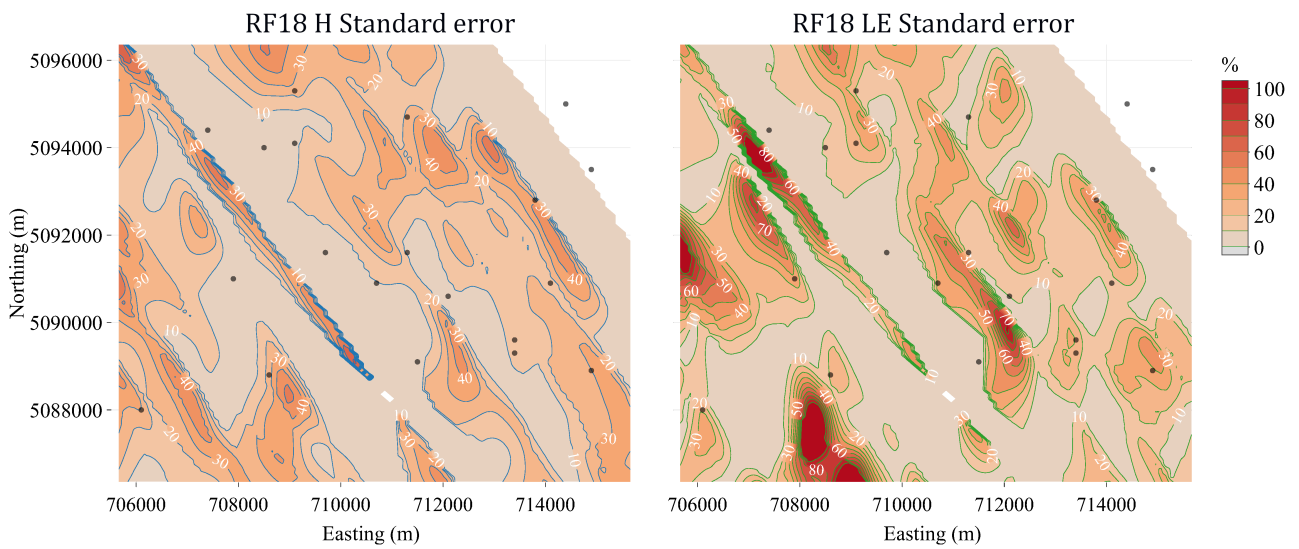


Figure S17. Standard error topographies for sensible (left) and latent (right) heat fluxes for Research Flight 18 in the September IOP, 24 Sep. 14:00 to 16:30 CDT, over the 10x10 km CHEESEHEAD core domain. The brown dots are the NCAR-ISFS tower locations.

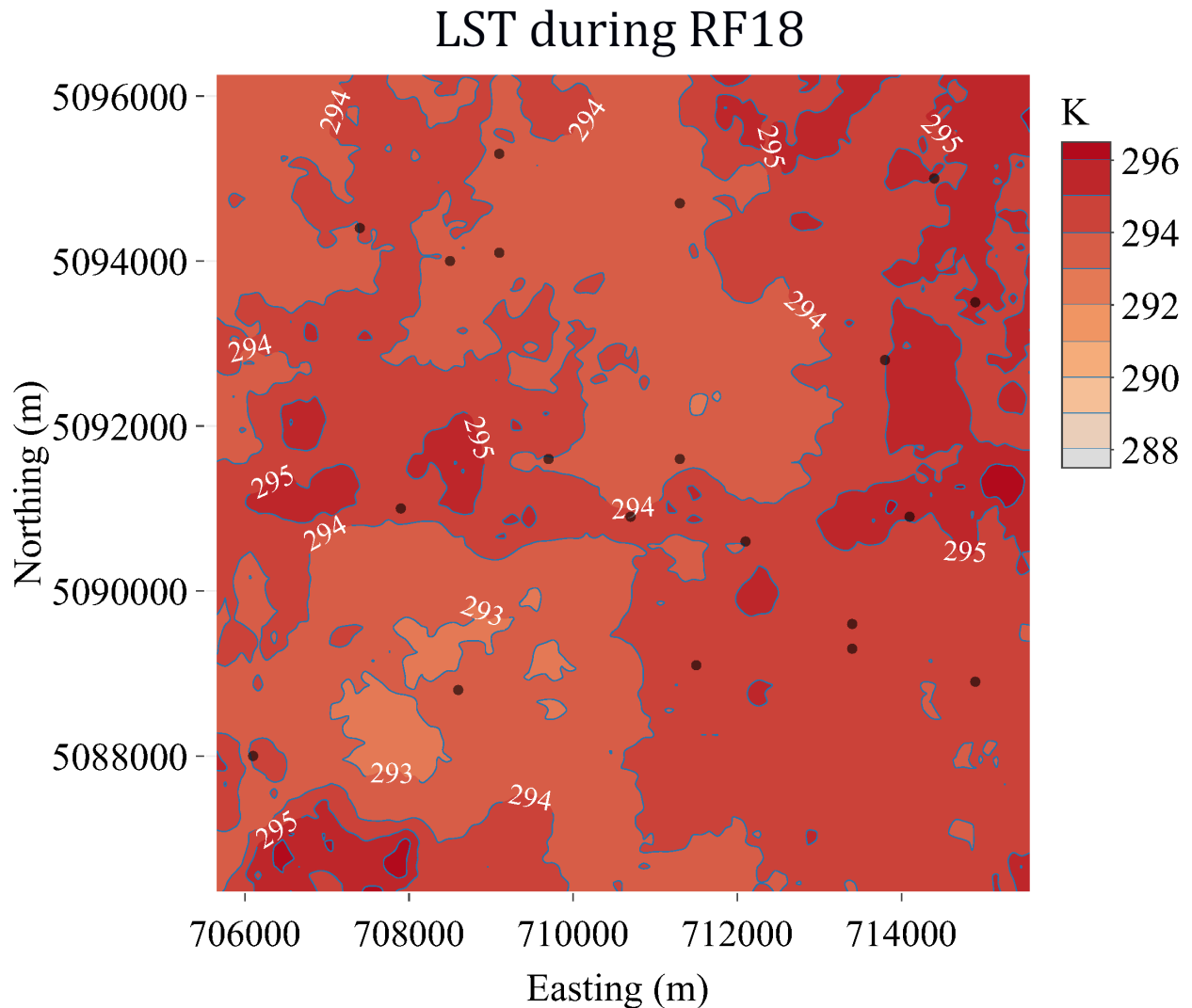


Figure S18. Fusion Land Surface Temperature data for the 10x10 km domain during Research Flight 18 in the September IOP, 24 Sep. 14:00 to 16:30 CDT, from Desai et al. (2021)